UNIVERSITY OF TECHNOLOGY SYDNEY
Faculty of Engineering and Information Technology
School of Mechanical and Mechatronic Engineering

Locomotion dynamics of agile canines

by

Hasti Hayati
Principal supervisor: Prof David Eager
Co-supervisors: Dr Paul Walker and Dr Terry Brown

A THESIS SUBMITTED
IN PARTIAL FULFILLMENT OF THE
REQUIREMENTS FOR THE DEGREE

Doctor of Philosophy

Sydney, Australia

2019

Certificate of Authorship/Originality

I, Hasti Hayati declare that this thesis, is submitted in partial fulfillment of the requirements for the award of Doctor of Philosophy, in the school of Mechanical and Mechatronic, Faculty of Engineering and IT, at the University of Technology Sydney.

This thesis is wholly my own work unless otherwise reference or acknowledged. In addition, I certify that all information sources and literature used are indicated in the thesis.

This document has not been submitted for qualifications at any other academic institution.

This research is supported by the Australian Government Research Training Program.

Production Note:
Signature: Signature removed prior to publication.

Date: 17/02/2020

ABSTRACT

Locomotion dynamics of agile canines

by

Hasti Hayati

Principal supervisor: Prof David Eager

Co-supervisors: Dr Paul Walker and Dr Terry Brown

Greyhounds are the fastest of all canine breeds, capable of attaining 70 km/h in 30 metres. The greyhound's unique sprinting ability has made it an elite sprinter and racing animal throughout history. Greyhounds sustain specific injuries, mainly skeletal, that are believed to be race-related and are rarely seen in other breeds of dogs. This dissertation focuses on studying the locomotion dynamics and foot-surface interaction of greyhounds. Accordingly, a thorough review was conducted of the literature on severe musculoskeletal injuries in greyhounds, factors contributing to injury in greyhound racing, different methods of measuring the locomotion dynamics of legged mechanisms, and different approaches to simulating legged locomotion. This review is presented in Chapter 2. Chapter 3 outlines common types of severe race-related injuries in racing greyhounds drawn from two years' worth of injury data collected on New South Wales greyhound racing tracks by qualified on-track veterinarians between January 2016 and December 2017. In Chapter 4 the method used to study the functional properties of greyhound race track sand surfaces is described, and the findings of the effects of altering the moisture content and rates of compaction on the dynamic behaviour of sand surfaces are presented and compared with findings from relevant literature. The experimental method used to derive the stiffness and damping coefficients of sand samples is explained in detail. Chapter 5 shows how the galloping dynamics of greyhounds were measured using a single Inertial Measurement Unit (IMU). The IMU which was equipped with a tri-axial accelerometer was embedded in a pocket located approximately on the

greyhound's Centre of Mass. The acceleration signals could successfully identify the turning dynamics regardless of the type of track surface. Finally, Chapter 6 presents the results of simulations of the hind-leg dynamics during the most critical duration of the galloping gait using the Spring-Loaded-Inverted-Pendulum method. The primary purpose of the designed SLIP model was to estimate greyhound hind-leg dynamics by altering surface properties.

Dedication

To my family.

Acknowledgements

First and foremost, I would like to express my sincere gratitude, to my supervisor, David Eager, for his unconditional support and for sharing this journey alongside me. I cannot express in words how grateful I am and how much his supervision and mentorship meant to me. I would like to thank my co-supervisors Paul Walker and Terry Brown, for their support during my candidature. Beside my supervisory team, I would like to thank Benjamin Halkon and Sebastian Oberst for their insightful comments and encouragement. Also, special thanks to the kind-hearted Chris Chapman, the manager of UTS Dynamics and Mechanics of Solid laboratory, for his help in conducting my experiments.

I would like to thank my teammates in the RHISN team, Sanaz Mahdavi, Robert Stephenson, Nathan Thomas, and Imam Hossain, for the sleepless nights we were working together and all the fun we have had in the last four years.

I would like to express my deepest gratitude to UTS Women in Engineering and IT (WiEIT) team, who warmly welcomed me in the team in July 2019. To Arti Agruwal, whom I always look up to, to Eva Cheng, Lauren Black, Amy and Amelia, who all support my passion towards empowering women.

To all of my friends and colleagues, Jeri Childers, MaryAnn McDonald, Jacqui White, Kasra Khosusi, Sara Farahmandian, Anna Lidfors Lindqvist, Dana Rezazadegan, Hamid Lashgari, Mohammad Assefi and Pouria Khojaste who were all beside me and supported me during this journey.

To my dear friends back in Iran, who maintained their friendship regardless of 12,000 km distance. Zahra, my first friend in the world and Afsaneh, who I shared the best undergrads life with her.

To my mother-in-law, Mahnaz, the kindest soul in my life, my father in law,

Saeid, for his endless support, my brother-in-laws, Behkam and Behdad and my sister-in-law Kimia, who are not in-laws for me, they are real brothers and sister.

To my mother, Mina, my role model and who taught me to be strong, to my father, Heshmatollah, who taught patience and spirituality, to my brother Pedram, whom talking to always keeps me motivated, to Tjasa, my sister-in-law, for her peaceful soul and to the youngest member of family Kaia, my niece, whom because of her I've learnt how to love unconditionally.

Last but not least, I dedicate this dissertation to my love, my soul-mate, my best friend, my dear husband Behnam. Without you, I couldn't be me. Love you forever.

Hasti Hayati

Sydney, Australia, 2019.

List of Publications

Journals

[1] **Hayati, H**, David E, and Paul W. "The effects of surface compliance on greyhound galloping dynamics." *Proceedings of the Institution of Mechanical Engineers, Part K: Journal of Multi-body Dynamics* 223(4): 1033-1043, 2019.

[2] **Hayati, H**, Mahdavi F, Eager D. "Analysis of agile canine gait characteristics using accelerometry." *Sensors* 19(20): 4379, 2019.

[3] Eager, D and **Hayati, H**. "Additional Injury Prevention Criteria for Impact Attenuation Surfacing Within Children's Playgrounds." *ASCE-ASME Journal of Risk and Uncertainty in Engineering Systems, Part B: Mechanical Engineering* 5(1): 011002, 2019.

[4] **Hayati, H**, David E, and Paul W. "Locomotion dynamics of turning and sprinting on different surfaces in agile quadrupeds: racing greyhounds" *ASME Journal of Dynamic Systems, Measurement, and Control* [Under Review].

Conferences

[1] Eager D, **Hayati, H**, Chapman C. "Impulse Force as an Additional Safety Criterion for Improving the Injury Prevention Performance of Impact Attenuation Surfaces in Children's Playgrounds." In *ASME 2016 international mechanical engineering congress and exposition* 2016 Feb 8. American Society of Mechanical Engineers Digital Collection.

[2] **Hayati, H**, Eager D, Jusufi A, Brown T. "A study of rapid tetrapod running and turning dynamics utilizing inertial measurement units in greyhound sprinting." In *ASME 2017 International Design Engineering Technical Conferences and Com-*

puters and Information in Engineering Conference 2017 Nov 3. American Society of Mechanical Engineers Digital Collection.

[**3**] **Hayati, H**, Eager D, Stephenson R, Brown T, Arnott E. "The impact of track related parameters on catastrophic injury rate of racing greyhounds." In *9th Australasian Congress on Applied Mechanics (ACAM9)* 2017 (p. 311). Engineers Australia.

[**4**] **Hayati, H**, Walker P, Mahdavi F, Stephenson R, Brown T, Eager D. "A comparative study of rapid quadrupedal sprinting and turning dynamics on different terrains and conditions: racing greyhounds galloping dynamics." In *ASME 2018 international mechanical engineering congress and exposition* 2018 Nov 9. American Society of Mechanical Engineers Digital Collection. [Nominated for best paper, an invited paper to ASME jorunals].

[**5**] **Hayati, H**, Walker P, Brown T, Kennedy P, Eager D. "A Simple Spring-Loaded Inverted Pendulum (SLIP) Model of a Bio-Inspired Quadrupedal Robot Over Compliant Terrains." In *ASME 2018 International Mechanical Engineering Congress and Exposition* 2018 Nov 9. American Society of Mechanical Engineers Digital Collection.

[**6**] Mahdavi F, Hossain MI, **Hayati, H**, Eager D, Kennedy P. "Track Shape, Resulting Dynamics and Injury Rates of Greyhounds." In *ASME 2018 International Mechanical Engineering Congress and Exposition* 2018 Nov 9. American Society of Mechanical Engineers Digital Collection.

[**7**] **Hayati H**, Mahdavi F, Eager D. "A single IMU to capture the fundamental dynamics of rapid tetrapod locomotion: Racing greyhounds". In *European Society of Biomechanics.* 2019 Jul 10.

[**8**] Mahdavi F, Hossain MI, **Hayati, H**, Eager D, Kennedy P. "Track Shape, Resulting Dynamics and Injury Rates of Greyhounds." In *ASME 2018 International Mechanical Engineering Congress and Exposition* 2018 Nov 9. American Society of Mechanical Engineers Digital Collection.

[**9**] **Hayati, H**, Eager D., Walker P. "An impact attenuation surfacing test to analyse the dynamic behaviour of greyhound racetrack sand surface." In *World Engineering Convention Australia 2019 proceeding* 2019 Nov 22. [Accepted].

Nomenclature and Notation

g	Gravitational acceleration
l	Hind-leg length
$\dot{l}$	Hind-leg linear velocity
$\ddot{l}$	Hind-leg linear acceleration
m_b	Overall mass of the greyhound
m_c	Mass of the Clegg hammer
m_l	Hind-leg mass of the greyhound
$[\ddot{x}]$	Vector of acceleration obtained from the accelerometers
$[\dot{x}]$	Vector of velocity obtained from the accelerometers
$[x]$	Vector of surface penetration obtained from the accelerometers
y	Surface compression
$\dot{y}$	Surface linear velocity
$\ddot{y}$	Surface linear acceleration
C_s	Surface damping coefficient
F	Impact force of the Clegg hammer
K_l	Hind-leg stiffness coefficient
K_s	Surface stiffness coefficient
T	Kinetic energy
U	Potential energy
$\mathcal{L}$	Lagrangian
θ	Hind-leg angle with respect to the ground
$\dot{\theta}$	Hind-leg angular velocity
$\ddot{\theta}$	Hind-leg angular acceleration
G_{max}	maximum acceleration
J_{max}	maximum jerk

w	moisture content
M_b	mass of the container and wet sand
M_c	mass of the container and dry sand
M_a	mass of the container

Abbreviation

AIS	anatomical injury severity
CFL	compressed flight phase
CoM	center of mass
CWT	continuous wavelet transform
DFT	discrete Fourier transforms
EFL	extended flight phase
FFT	fast Fourier transform
GPS	global positioning system
GRF	ground reaction force
HFR	high frame rate
iKMS	integrated kinematic measurement system
IMU	inertia measurement unit
ISS	injury severity index
LF	left fore-leg
LH	left hind-leg
NSW	new south wales
OTV	on track veterinarians
RF	right fore-leg
RH	right hind-leg

Contents

List of figures

List of tables

Chapter 1

Introduction

In this section, the thesis of this research, background, aims, objectives, significance, method, dissertation organization, and the main contributions are given.

1.1 Thesis

That the locomotion dynamics of agile canines (greyhounds), in a non-steady environment (race), can be measured via a single inertial measurement unit and estimated by a mathematical model.

1.2 Background

Greyhounds are the fastest canine with a speed of circa 68 km/h which is double that of the fastest human. Similarly to cheetahs, they use rotary gallop as their high-speed gait. Accordingly, greyhounds have been used in different athletic activities such as coursing and sprinting races throughout history.

There are unique injuries associated with racing greyhounds which are rarely seen in other breeds of dog. These injuries are believed to be caused by environmental conditions such as sharp bends on the race track, inappropriate surface compositions and insufficient banking on bends.

High rates of injuries in racing greyhounds have been documented in detail previously. The most common career-ending injuries in racing greyhounds were seen to be musculoskeletal injuries of the right hind-leg, specifically tarsal bones also referred to as the 'hock'.

The race track surface is a paramount risk factor. Thus, to find out what is causing such injuries in greyhounds, the leg-surface interaction should be studied in detail. Common methods of measuring dynamics of legged locomotion are:

- Deploying force plates to measure the kinetics of locomotion such as forces and torques acting on limbs and joints.
- Using wearable sensors to measure motion kinematics.
- Invasive methods such as in-vivo recording by Sonomicrometry to measure muscle activities during locomotion.

Studying the ground reaction forces (GRF) through force-plates provides highly accurate dynamic data, but it is not always a feasible approach since it is not always possible to embed a force plate on irregular terrains such as granular and compliant terrains that characterise the natural habitat of most terrestrials. On the other hand, wearable sensors can be used to study the locomotion kinetics of animals in their natural habitat, but the accuracy of the results is lower than when using force-plate.

Among different types of simulation methods, the spring-loaded-inverted-pendulum (SLIP) model is a mathematical model extensively used in simulating legged locomotion. It can capture the dynamics of legged animals and mechanisms with acceptable accuracy. With this method, the effect of surface compliance on the galloping dynamics of greyhounds can be simulated.

1.3 Aim, objectives and significance

1.3.1 Stakeholders

- **Greyhound racing**: Reducing the rate of catastrophic injuries is one of the major aims in the greyhound racing industry. This aim can be achieved by identifying the injury contributing factors and eliminating them from the race.
- **Comparative biomechanics**: Gait monitoring of agile quadrupeds such as racing horses and greyhounds in non-steady conditions is a big challenge in comparative biomechanics as conventional methods of gait analysis are usually designed for the laboratory environment. Using a wearable sensor and a

proof of concept whether it can obtain the fundamental aspects of quadrupedal locomotion in such conditions can provide a solid platform for further studies.

1.3.2 Aims

i. To analyse greyhound injury data to identify frequent types of life-threatening injuries and hazardous locations on the race track where most of the injuries occur.

ii. To analyse a sand sample from a greyhound racing track and determine the variables that are affecting its mechanical properties.

iii. To obtain a proof-of-concept of using a single warble-sensor device to monitor agile quadruped locomotion in a condition where other gait monitoring methods cannot be deployed.

iv. To estimate the dynamics of greyhound's hind-legs while galloping on surfaces with different mechanical properties.

1.3.3 Objectives and significance

i. The first objective is analysing two years worth of injury data (January 2016 to December 2017, provided by Greyhound Racing NSW (GRNSW)) to see whether the same injury pattern, viz. the high rate of injuries on right hind-legs is observed in the data.

ii. The second objective is analysing to what extent the mechanical properties of a sand sample (collected from a typical greyhound race track surface in NSW) are affected when the moisture content and the bulk density[1] are altered. The significance is that the results of this study can be used to optimise the sand surface compositions of greyhound race tracks to prevent the severe injuries caused by inappropriate track surfaces.

[1]Refer to Chapter 2, Section 2.6 for more information.

iii. The third objective is analysing the locomotion dynamics of racing greyhounds, using an inertial measurement unit (IMU). The measure of success in this objective is that the obtained data identifies differences in race track conditions (bends vs straight sections and different surface types). This method is significant in that it can determine the hazardous elements of greyhound race tracks to help the industry to eliminate these elements from the race.

iv. The fourth objective is developing a model to estimate the dynamics of a greyhound's hind-leg in a galloping gait. The measure of success is having less than 20% error between the mathematical model and experimental data. The experimental data are trajectories of a galloping greyhound's hip-joint during hind-leg stance, which will be obtained from high-frame-rate (HFR) videos. This model is significant in that it will predict the foot-surface dynamics of greyhounds over surfaces with different compositions as there is a current research gap in this field.

1.4 Methods

i. The first objective was analysing the injury data of racing greyhounds from January 2016 to December 2017 which was provided by GRNSW. Firstly, career-ending and severe injuries were categorised properly based on the current industry injury criteria. Then, anatomical injury severity was obtained. Finally, hazardous locations on the race track were determined using both the injury data and the recorded videos of the race.

ii. The second objective was analysing the functional behaviour of the greyhound race track surface by altering the level of moisture and compaction. The dynamic behaviour of the sand was studied by analysing the impact data. The impact data can be obtained using a standard drop test that provided the maximum deceleration, the maximum rate of change of acceleration, the impact duration, and the energy loss.

iii. The third objective was analysing the locomotion dynamics of racing greyhounds, using an IMU. The IMU was mounted approximately above the grey-

hound's center of mass. The animals were encouraged to run on a typical greyhound race track. The IMU was equipped with a three degree-of-freedom accelerometer capable of measuring the acceleration during galloping in three different axes (x-y-z). The data was analysed to see whether it could identify different locations and surface types. Animal ethics approval was required for this study.

iv. The fourth objective was developing a mathematical model to estimate the dynamics of a greyhound's hind-leg stance in a galloping gait over different surface types. The SLIP method is an extensively used method in capturing the dynamics of legged motion. Most of the current models in legged locomotion do not consider the underneath terrain. In the designed SLIP model, extra spring and damper elements were added to represent the surface. To obtain the governing equation of motion, the Lagrange method was used. To solve the obtained non-linear ordinary differential equation, the 4th order Runge-Kutta method was deployed. MATLAB ode45 solver was used to minimise the cost of computation in solving the equations. Kinovea -0.8.25 was used for analysing the experimental data i.e. motion tracking of hip joint during hind-leg single-support of HFR videos of galloping greyhounds. The experimental data was then compared with the model results to validate the SLIP model of hind-leg stance during galloping gait.

1.5 Thesis organization

This dissertation is organised as follows:

- Chapter 2: Literature review.
- Chapter 3: A Retrospective study of injuries in racing greyhounds.
- Chapter 4: Dynamic behaviour of greyhound track surfaces.
- Chapter 5: A Single IMU to measure greyhound locomotion dynamics.
- Chapter 6: SLIP model of greyhounds hind-leg during RH single-support.

- Chapter 7: Conclusion.

1.6 Contributions to the body of literature

The following publications were a direct result of this research:

- Chapter 3 – Identifying the most prevalent type of severe injuries and the hazardous location on the race track [3].
- Chapter 4 – Identifying the ideal moisture content and rate of compaction for sand surfaces and a method to obtain the mechanical properties of compliant surfaces [4, 5].
- Chapter 5 – A novel method to analyse the locomotion dynamics of agile canines using a single IMU [6–8]
- Chapter 6 – A SLIP model of the hind-leg which can predict the limb dynamics over different terrains [9, 10].

Chapter 2

Literature review

2.1 Introduction

The relevant literature that motivates and supports this dissertation is provided in this chapter. We firstly explain greyhound racing history in Section 2.2 and then describe the common types of injuries in this sport in Section 2.3.

Important injury contributing factors are divided into three main categories of (i) track-design factors, (ii) race-related factors, and (iii) seasonal factors and are explained in detail in Section 2.4.

Bend radius and surface of the track are two important risk factors. Sharp bends with insufficient camber, and track surfaces with inappropriate properties can provoke serious injuries. In Section 2.5, we review the fundamental characteristics of sand[1]. In Section 2.6.1 we introduce the factors that should be taken into account in assessing a safe surface.

A large number of studies have looked into ideal surface compositions concerning injury prevention. However, there is a research gap on the interaction of greyhound biomechanics and the underneath surface. Thus, in Section 2.6 we introduce the different methods used in studying body-surface interaction.

The most extensively used method to simulate legged locomotion dynamics is the spring-loaded-inverted-pendulum (SLIP) model. We explain the SLIP model and its application in biomechanics and robotics in Section 2.6.3. Finally, the summary of this chapter is given in Section 2.7.

[1]Sand is the common material for the race track surface in the greyhound racing industry.

2.2 Greyhound is an elite sprinter

Greyhounds are a breed of dog that belongs to the family of sighthounds (Figure 2.1). Sighthounds' ability to sprint and chase prey has made them a reliable food hunting assistant throughout history [11]. The greyhound has a maximum speed of more than 65 km/h [12]. The rotary gallop is the greyhound's preferred galloping gait [13], and is their fastest but also most fatiguing gait [14].

Figure 2.1 : A galloping greyhound on a race track.

Greyhound racing tracks vary in shape and design but are mostly an oval shape with either sand or natural grass surface. Races are run anti-clockwise with six to eight runners in each race. Greyhounds chase a mechanical lure, which is manually driven by a lure driver who tries to keep a distance between 5 to 7 m from the leading greyhounds [15].

2.3 Common greyhound racing injuries

Greyhounds sustain unique kinds of injuries seldom seen in other breeds of dogs [16]. These are mostly musculoskeletal injuries and are involved in locomotion and rapid acceleration [15].

As mentioned above greyhound racing is usually anti-clockwise. The race direction leads to specific types of injuries [16–19] which may be due to two reasons. Firstly, greyhounds use the rotary galloping gait with the limb-contact pattern of left fore-leg, right fore-leg, right hind-leg and left hind-leg [20]. In most of the greyhounds, the leading fore-leg is the left limb, and the leading hind-leg is the right

limb [21]. This means that the leading legs have to support the weight as well as the initial impact forces. Secondly, when a greyhound navigates around a bend, it has to lean towards the centre of the track to counteract the centrifugal force [22]. As a result, the load distribution on the limbs becomes asymmetrical on turns, putting the leading legs at a disadvantage [16].

Injuries to cranial muscles of the thigh, specifically *quadriceps fenioris* muscle group injuries, are occurring as a result of race direction, and are usually seen on the right hind-leg [17]. Similarly, the left foreleg is affected by race direction as the fracture of metacarpal bones is frequently observed in the left fore-leg [18]. Gillette and Hickman both reported more injuries on the left accessory carpal bone [23, 16] and the left distal and proximal interphalangeal joints compared to those of the right foreleg. In contrast, the right hind-leg had more injuries than the left side with high rates of central tarsal fracture and *gracilis* muscle rupture [16].

Having tight bends with insufficient banking and straight-to-bend transition can cause specific injuries. For instance, Davis mentioned that pad injuries and fractures of the accessory carpal bone are regularly noticed in fast greyhounds that rapidly change their direction on sharp bends [17]. Furthermore, Bloomberg et al. compared the injury data of a track with and without camber, which showed a 53% reduction in the tarsal injuries on the track with camber. They argued this reduction might be due to introducing the camber on bends [24].

Inappropriate bend design also increases the risk of greyhound collisions. Ireland [25] in a book authored by Bloomberg et al. [22] argued that there are two main strategies adopted by greyhounds to reduce the excessive centrifugal force when running around a bend. The greyhounds either reduce their speed or seek a larger radius (they may adopt both strategies at the same time.). Hence, when a greyhound at its top speed faces a poorly designed track (short radius and/or level bend) it generally slows down. Slowing down causes the 'interference' or 'congestion' which creates a potential collision area on bends [25] that increases the likelihood of an injury. This interference has been previously noted in the literature where the majority of the injuries were observed to occur on the first bend as a result of

congestion and/or collisions [3, 26, 27].

Davis was among the pioneers who studied track-related injuries in racing greyhounds, provided diagnosis techniques, and appropriate treatment procedures for each injury [17]. Based on his study some injuries arose due to the inappropriate mechanical properties of the track surface. For instance, injuries to the muscles of the pelvic limb and the muscles and tendons lying over the volar surface of the metacarpal bones, are usually seen as a result of a hard sandy surface [12].

Gillette also believed that the track surface was one of the main risk factors and therefore gave a clear definition of safe track surface properties. He argued that these factors can be determined with proper surface composition and regular maintenance [23]. Bloomberg et al. also insisted on regular track maintenance because tarsal injuries increased in consecutive races that harden the surface [26].

Summing up, the top career-ending and life-threatening injuries in greyhound racing mentioned in the literature, are injuries to the right tarsal [3, 16, 17, 19, 28] and the muscle of the pelvic limb (specifically the *gracilis* muscle) [16, 17].

2.4 Injury contributing factors in greyhound racing

The contributing injury factors are divided into three main groups of (i) track-design factors, (ii) race-related factors, and (iii) seasonal factors, which are explained in the following subsections.

2.4.1 Track-design factors

Bends

For obvious reasons, greyhound racing has its inherent hazards causing loss of balance and stability that leads to injuries, and poor track design can worsen the injury rate [16].

Greyhound racing tracks are usually an oval shape with two straight sections and two bends. The first straight section after the starting boxes is called the 'Back straight', and the one right before the finish line is called the 'Home straight'.

There are usually ten to twelve races in each 'meeting' that can start from different distances.

Evidence indicates that the majority of injuries are happening on bends (see above). In order to find out why there is such a high probability of an incident on bend, it is necessary to define a safe bend.

There are two critical elements considered in bend design; the radius and the camber or surface banking [25]. A high rate of acceleration and change of the rate of acceleration (jerk) [29] act on greyhounds' limbs as they are navigating around the bend. The extreme force upon contact of one paw in the rotatory galloping gait [30] makes them even more prone than human athletes to sustain injuries while turning.

The answer can be found in the simple mechanics of turning. Any moving object on a turn is exposed to a centrifugal force given in Equation 2.1 below.

$$F_c = \frac{mv^2}{r} \tag{2.1}$$

where F_c is the centrifugal force, v is the speed of the object, r is the radius of the bend and m is the mass of the object. The speed has a direct relationship with centrifugal force while the radius has the opposite relation with it. In other words, the higher the speed and the lower the radius, the higher the centrifugal force.

Moreover, in addition to the mentioned strategies in facing sharp bends, greyhounds also lean towards the center of the track to counteract the centrifugal force by their weight, which is illustrated in Figure 2.2 below. The anti-clockwise direction of the race puts the right rear-leg at a disadvantage on bends. As greyhounds lean, the load distribution become asymmetrical and puts more load on the leading hind-leg [25].

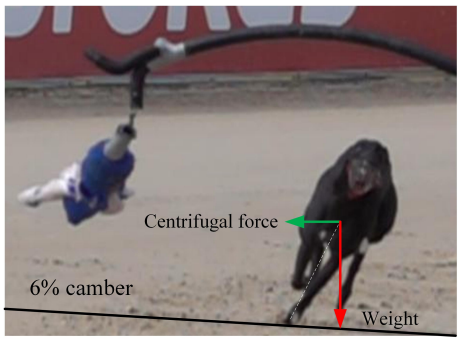

Figure 2.2 : A greyhound leans towards the inner rail while running around a bend at the Richmond track, NSW, Australia.

Camber is introduced to reduce the excessive centrifugal force and therefore the required lean angle. Greene [31, 32] was among the pioneers to discuss the benefits of camber on athletic tracks. Green [32] noted athletes who ran on banked competition indoor running tracks reported that a banked bend puts less stress on the ankles and that they can obtain maximum velocity with no apparent ill effect. On the other hand, athletes on a non-banked track experienced excessive pronation and/or supination which can cause 'shin splints' or 'anterior compartment syndrome' as a result of excessive mechanical stress on the interosseous attachment of the posterior *tibialis* muscle which helps to control the roll stability of the ankle.

Ireland mentioned that depending on the speed of the greyhounds, the camber degree should vary [25]. He suggested different camber angles are required for different race distances. For 800 m races the ideal camber which eliminates the need to lean is 33% or 18.4°. For 400 m races the optimum camber is 50% or 26.5°.

However, as most of the greyhound tracks have sand surfaces, in practice the optimum camber angles as advised by Ireland [25] are challenging to maintain particularly in heavy rainfall regions. For example, a storm can erode the sand from the track surface and move it to the bottom of the slope and into the drainage gutter. It is recommended this sand be regularly transferred back to the track. Thus, a camber angle in high rainfall areas is recommended to be 14% or 8.1° [25].

Track surface

The race track surface is believed to be one of the main factors contributing to injury. [17, 19, 21, 33, 34]. The ideal track surface should act to absorb the impact forces of the foot, provide traction for a controlled gallop, and efficient use of energy [35]. Moreover, any inconsistency on the track surface is dangerous and can cause an injury [12, 35] as the greyhound is not capable of adjusting its gait based on changing surface conditions [23].

The recommended mixture of track materials for greyhound race tracks are sand, silt, clay and water. Particles are also defined by their size i.e. clay (less than 2×10^{-3} mm), silt ($2{\times}10^{-3}$ mm), and sand ($5{\times}10^{-2}$ to $2{\times}10^{-1}$ mm) [25]. The ratio of these track materials is important as it will ensure absorption of the impact forces and thereby provide a safer race track for the animals. Table 2.1 shows the recommended sand particle size and percentage in greyhound tracks of NSW, Australia.

Table 2.1 : Recommended sand particle sizes and percentage by GRNSW.

Fraction	**Size (mm)**	**Percentage (%)**
Fine gravel	2.00	0
Very coarse sand	1.00	$< 5\%$
Coarse sand	0.50	10% - 20%
Medium sand	0.25	30% - 40%
Fine sand	0.15	40% - 50%
Very fine sand	0.05	40% - 50%
Silt/clay	< 0.05	$< 5\%$

Apart from the granular size and percentage of the particles, two other important variables affect sand functional properties. One is the moisture content, which binds the sand particles together as well as helping in absorbing the impact forces. Another is the rate of compaction or the bulk density of the sand which provides enough traction for greyhounds [25]. The effect of these variables on the sand surfaces studied is given in detail in Section 2.6.1.

There are also injuries correlated with the type of surface used as the type and severity of the injuries are different on tracks with sand as opposed to grass surface [36, 33, 19]. Prole [19] mentioned that on the grass surface 95% of all the reported foot injuries were on toes, while only 6% of them were on tarsal bones. In other words, the common injuries on grass and sand surfaces are toe and hock injuries, respectively. Added to this, *Paronychia*, which is accumulating and wedging sand under the nails, is common on sand tracks [17].

2.4.2 Race-related factors

Apart from the track-related factors, there are other factors that affect the injury rate in racing greyhounds. For instance, the mechanical lure configuration (i.e. the length and height), may impact the probability of injuries. We observed that a longer lure would improve greyhounds' line of sight to the lure as well as distributing the greyhounds across the track width, which resulted in lower rates of injuries [37].

The race grade, which usually implies the speed of the greyhound, is seen to affect the injury rate [27] (i.e. the higher the speed, the higher the probability of injuries). This fact was observed by Sicard et al. in a survey on the injury data of five greyhound tracks in Washington, US over two years [27]. Iddon et al. also conducted a survey of two greyhound race tracks in the UK and reported a significant increase in the injury rate in fast track conditions compared to the slow track conditions [33].

The race number can be another injury factor as more injuries were seen in the final races [26]. Bloomberg argued that the surface becomes harder in final races and therefore increases the risk of injuries specifically tarsal injuries [26]. However, Sicard et al. did not observe any correlation between the race number and the injury rate [27].

2.4.3 Seasonal factors

Iddon et al and Sicard et al. advised that the time of the year and the ambient temperature did not have a significant effect on the injury rate [33, 27]. However,

Prole observed more injuries in dry weather conditions than wet conditions. The reason was argued to be the higher speed of greyhounds on drier and therefore harder track surface which increases the chance of accidents [19].

2.5 Characteristics of sand

We argued that the track surface is one of the critical risk factors and should be considered in injury prevention practices. As most of the greyhound track surfaces are made of sand, its characteristics and the variables which change its mechanical properties are reviewed in detail in the following sections.

2.5.1 Size, shape and percentage of sand particles

We have presented the recommended particle size and shape for greyhound racing sand surface above (Table 2.1). Here, apart from introducing sand particle shape, the rationale behind the importance of sand particle properties is given. In addition, the conventional methods to measure these properties are briefly explained.

The sand grading curve shows the portion of sands with different particle sizes, from fine particles to gravel. The grading curve of sand can be determined by using a manual or automatic sieve.

The shape of the sand particles can vary from a 'very angular' to a 'well rounded' shape [1] and is a key influence on the dynamic behaviour of the sand [38].

There are two key variables used to classify sand particles, namely 'roundedness' and 'sphericity', which are illustrated below in Figure 2.3.

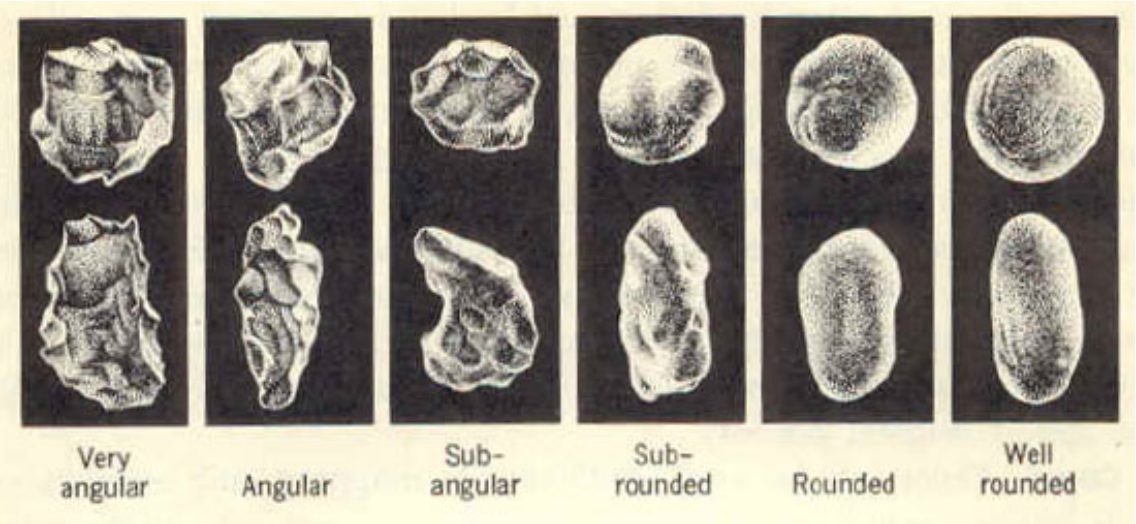

Figure 2.3 : Sand particle shape. Modified after Power's article [1].

Roundness is associated with the relative sharpness and the angularity of the edges/corners of the particle. Sphericity is defined as the ratio of the particle surface area to the surface area of the sphere. In other words, the sphericity determines the degree to which the shape of the particle approaches that of the sphere [38].

These parameters determine the dynamic behaviour of the sand. For instance, as much as roundedness is desirable in terms of the impact attenuation properties, angularity is not. When the particles are very angular, they tend to pack tightly as the sharp corners interlock and will resist the movement of the particles when subjected to an impact. In contrast, well-rounded particles tend to smoothly transit to different locations upon impact [39].

2.5.2 Water retention

Depending on the particle size, shape and percentage of particles, sand can retain specific amount of water. This value is referred to as 'water retention'. The water retention curve[2] is the relationship between the water content (θ) and the soil water potential (Ψ) [2].

[2]The water retention curve is typical for different types of soil. It is also called the soil moisture characteristic [2].

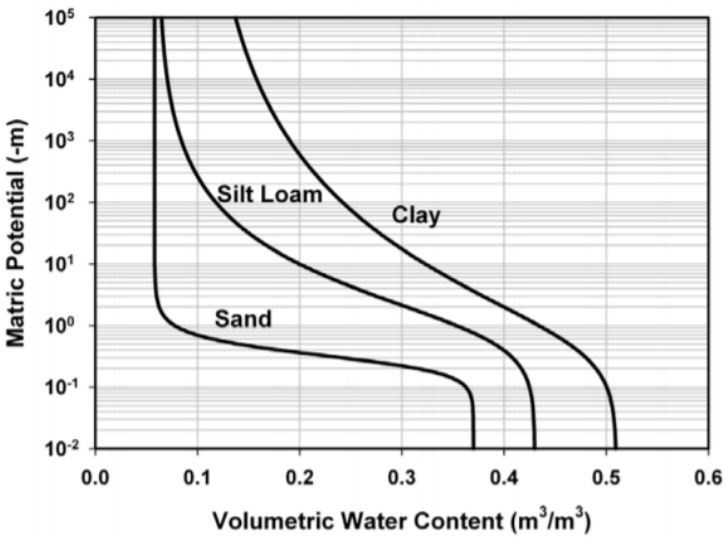

Figure 2.4 : Typical soil water characteristic curves for different types of soil [2].

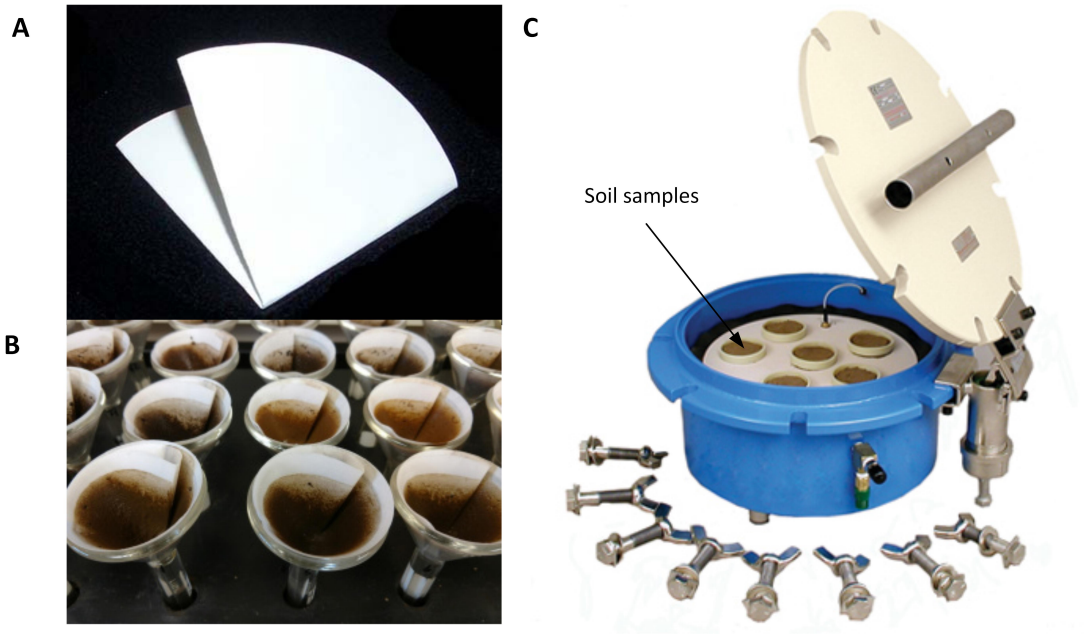

Figure 2.5 : A filter paper (A). Soil samples in filter papers (B). A pressure cell (C).

Two conventional methods to generate water retention curves use pressure cells and filter paper [2] are shown in Figure 2.5.

As argued above, the soil water potential specifies how much water can be retained in sand. There are different items of equipment which are used to measure the Soil Volumetric Content (SWC), which are called 'water potential meters'. Different types of potentiometer used in the laboratory and *in-situ*, are illustrated in

Figure 2.6.

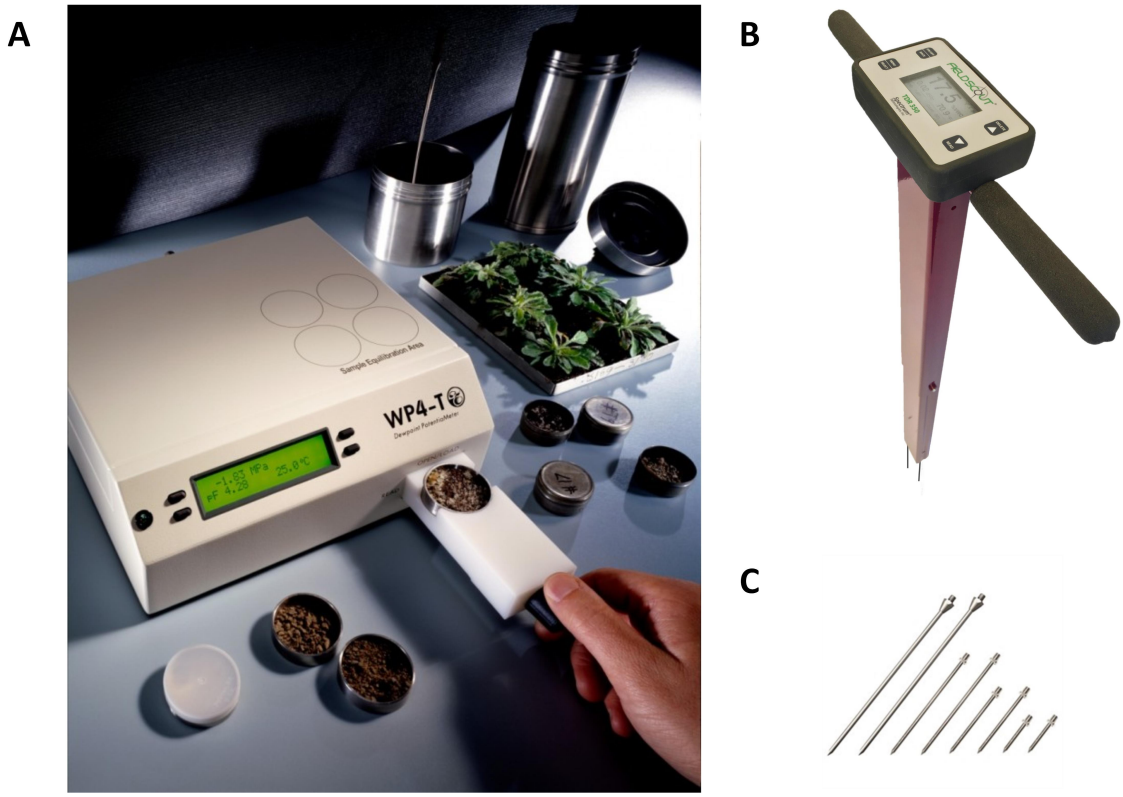

Figure 2.6 : WP4-C Dewpoint potentiometer and the soil samples (A). Field Scout TDR350 Moisture Meter (B). Potentiometer rods (C).

To have an accurate moisture content, a conventional oven can be used [40]. In Chapter 4, we have explained in detail the method for measuring the moisture content of sand samples.

2.6 Limb-surface interaction

The importance of the track surface in controlling the injury rate was mentioned by different researchers. However, there is still a significant gap in understanding the interaction of these agile sprinters and the underneath terrain [15, 21].

Ireland advises that the moisture consistency influences compressive[3] and shear strength[4]. Thus, moisture should be maintained within 2% of the optimal value[5].

[3]The strength of the surface material required to withstand the force of impact.

[4]The strength of the material that allows propulsion of the support limb.

[5]No specific moisture level was mentioned.

A moisture level greater than the optimum value produces a sloppy track and a moisture level lower than the optimum level produces a dry and therefore a hard track [25]. A hard track would exert excessive forces on greyhounds' limbs resulting in injuries, whereas a sloppy track would throw sand into the eyes of following greyhounds [25, 35].

Three different methods to study greyhound limb-surface dynamics are reviewed here. These are namely (i) experimental methods to study the effect of variables that affect functional properties of the track surface (Section 2.6.1), (ii) experimental methods to measure the locomotion kinetics of greyhounds in a race (Section 2.6.2), and (iii) a simulation method to model the greyhounds limb-surface interaction (Section 2.6.3), which is presented in the following sections.

2.6.1 Track surface test methods and devices

Understanding the dynamic behaviour of the race track surfaces contributes to engineering a safe race. Thus, this section aims to understand how different variables alter the mechanical properties of sand surfaces and what is the optimum value for these variables in terms of injury prevention. To the best of our knowledge, there is no study of optimising these values for greyhound race tracks, and therefore those in equine race tracks are reviewed.

To compare the dynamic properties of dirt and synthetic surfaces[6], an *in-situ* test using a Track Testing Device (TTD), was conducted by Settebro et al. on an equine race track surface [41]. The effect of three different variables (i) the impact velocity (1.91 m/s, 2.30 m/s and 2.63 m/s), (ii) the impact angle (0° and 20°), and (iii) the repeated impacts (two times), in a constant moisture content (10.4 ± 1.2% for the dirt surface and 0.2 ± 0.2% for the synthetic surface) were analysed. The analysed impact data were the maximum force, the load rates and the stiffness.

Apart from the TTD, a Clegg hammer and a shear vane tester were used. The Clegg hammer was developed by Branden Clegg to control the compaction of road materials [42]. The apparatus consists of a guided tube and a flattened cylindrical

[6]No more information on the material composition of the surfaces is given.

mass. The mass is located inside the tube and should be dropped at standard height on the surface. The Clegg hammer measures the peaks of deceleration when the mass comes into contact with the surface in units of tens of the acceleration due to gravity [42, 43].

Setterbo et al. showed that all the studied variables have a significant effect on the dynamic behavior of both surfaces, with the largest effect observed from the repeated impact tests [41].

Holt et al. studied the effect of sand moisture levels ($11.96 \pm 1.63\%$, $17.31 \pm 1.14\%$, $19.08 \pm 0.78\%$) and rates of compaction (1.647 ± 0.02 g/cm^3, 1.748 ± 0.046 g/cm^3, 1.766 ± 0.039 g/cm^3) of two different drainage systems (Limestone gravel and permavoid^{TM} drainage), on the dynamic performance of synthetic equestrian surfaces (93.84% sand, 5.15% fibre and 1.01% binding polymer). They used the Orono Biomechanical Surface Tester (OBST)[7], a 2.25 kg Clegg hammer and a 30 kg traction device equipped with a horseshoe [45].

The OBST, which simulates the collision of horse forelegs and the ground, was dropped four times on each surface for each treatment. The measured parameters were the maximum load, the maximum loading rate, the maximum vertical deceleration, and hysteresis (the energy loss which is defined as the area under the load-deformation curves) [45].

The Clegg hammer was dropped four times based on the protocol recommended by ASTM Standard [46]. A 30 kg traction device, which was also used to measure the traction of the surface, was dropped once in four different locations of the test chamber for each treatment from a height of 200 mm. For each experiment, the moisture content remained constant while the compaction rate altered. A tamper equipped with an accelerometer was used to produce the low, medium and high surface density. For the low-density surface, the absorptive layer (the top 30 mm layer of the 150 mm surface chamber) was raked. For the medium density surface, the absorptive layer was struck three times to reach the overall thickness of 140 mm,

[7]Please refer to [44] for more details of OBST.

and for the high-density surface, the top layer was struck five times to reach the overall thickness of 130 mm [45].

Holt et al.'s results showed a significant effect of the moisture content, density, and drainage type on the measured parameters. It was concluded that a moisture content of 19.08% and a medium density of sand (1.748 $\pm$ 0.046 g/cm^3) plus the permavoid^{TM} drainage, has the most desirable mechanical properties for a safe race [45]. Moreover, in this surface condition, the energy loss (the area under the load-deformation curves) and vertical acceleration upon the impact, were relatively lower than in other conditions. Ratzlaff et al. argued that these properties mitigate the stresses exerted on the animal's[8] limb during rapid locomotion [47].

As also stated by Setterbo et al. [41], high density is correlated with the high rate of injuries [48]. Hence, 'surface harrowing' is suggested which in practice can reduce the density of the surface [49]. On the other hand, low density can have a detrimental impact on locomotion efficiency [50]. Gillette [35] stated that, one of the requirements of the ideal surface is having enough traction for gripping. The low density surfaces were shown to have low support needed for propelling the body forward [50].

The horizontal properties of the surface, represented by the shear strength or surface traction, should also be kept in an optimum range. Traction is affected by the amount of moisture content and density, and at high values it would impose a large amount of bending moment on the foot [51][9]. In contrast, a low traction surface reduces the support needed for efficient gallop [45].

2.6.2 Measuring legged locomotion dynamics

Above, we have reviewed different experimental methods to quantify track surface dynamic behaviour. In this section, the experimental method to measure the kinetics and kinematics of foot-surface interaction are given.

[8]Racing horses.

[9]Tarsal bone of the greyhounds.

Force plates

McMahon and Green were among the pioneers who looked into the impact of surface compliance on the running dynamics [52]. They designed a two degrees-of-freedom (DOF) spring-mass model representing the legs and the track surface. Their objective was to predict the effect of surface compliance on step length and ground contact time. To verify their model, they designed a single lane running surface with 26.25 m length, made of plywood boards (0.406 m $\times$ 1.219 m $\times$0.015 m). The plywood was screwed to 0.044 m $\times$ 0.089 m rails which served as supports. Moving the supporting rails could alter the spring coefficient of the surface. A Kistler force plate (model 9261A) was mounted beneath the track to measure foot force. Eight healthy male subjects ran over the experimental wooden track. Analysing the foot force result on a hard surface showed a spike five times the average body weight of the runners, which did not appear on a very compliant surface. However, running on the compliant surface with a stiffness 0.15 times this stiffness, reduced the speed up to 0.7 times compared to the hard surface. Finally, a moderately compliant surface, which is found to have the stiffness three times of a man's body stiffness, increased the speed up to 2% and also correlated with a low injury rate.

To assess how much leg stiffness and metabolic costs of running are affected by track surface stiffness, Kerdok et al. designed an experimental platform with adjustable stiffness which was embedded on a 1000 Hz force-plate-fitted treadmill. The treadmill was fitted with five different track surfaces (75.4, 97.5, 216.8, 454.2, and 945.7 kN/m). Eight healthy males ran over the designed platform for five minutes in a mirrored fashion (i.e. running from the softest to the stiffest and then the stiffest to the softest). To measure the metabolic cost of running the oxygen uptake was measured by a closed gas-collection Douglas bag setup. Their results showed that running mechanics are not affected by substrate surface while running economy is affected [53].

Although the force plate provides accurate kinetic data, it cannot be used to study the effect of difficult terrains such as the compliant or granular surfaces which are characteristics of surfaces encountered by ecologically relevant animals.

Inertial measurement units

Inertial measurement units (IMU) can be used to study complex dynamics such as turning and locomotion on difficult terrains where conventional methods cannot be deployed.

Wilson et al. studied the hunting dynamics of cheetahs using an in-house collar-shaped IMU. They successfully analysed the locomotory dynamics of the cheetahs hunting in the wild [54].

IMUs can also be used to study the locomotion kinetics of arboreal animals that obviously cannot be studied through force platforms. In a study conducted by Bayren et al. a tri-axial accelerometer was used to measure the landing and gliding kinetics of the Malayan colugo. They found that the propulsive kinetics during take-off increase in longer glides. However, the landing forces decrease with longer glide-distances [55].

Spence et al. used a custom designed accelerometer backpack to study the effect of complex terrain (leaf litter) on the locomotion dynamics of rapid insects (death's head cockroaches). They attached the accelerometer close to the insect CoM. Their results showed that the peaks of CoM vertical acceleration on soft surfaces were smaller than on rigid surface [56].

Use of accelerometers to characterise equine gaits to the best of our knowledge dates backs to 25 years ago in studies conducted by Barry et al. where they used a single IMU to analyse equine gait [57, 58]. Recently, in a study conducted by Uchiyama et al. in 2011, the walking acceleration patterns in 50 healthy human subjects were compared with that of 11 horses to examine whether the movement of horse's pelvis during horseback riding resembles human walking. Witte et al. used two uniaxial IMUs, one mounted on the hoof and another on the metacarpophalangeal joint, and measured the footfall timing of horses (*Equus caballus*) to predict the peak GRFs acting on limbs. They compared their results with force plate data which showed a mean error of 2.3 ms and 3.5 ms for the timing of limbs touch-down and lift-off, respectively, across all gaits [59]. Following this study, Pfau et al.

used three different sensors to measure the galloping dynamics of thoroughbred racehorses, in particular, their CoM movement and external energy fluctuation [60]. One accelerometer was mounted on the horse's hoof to measure the contact time of the limb with the ground. A GPS data logger and an IMU sensor, which were needed to estimate the CoM movement as well as estimating the external mechanical energy, were mounted on the wither of the animals. Their results showed that mechanical energy is mostly affected by changes in craniocaudal velocity (anterior-posterior direction). It is found that the CoM movement was also negligible during a high-speed gallop.

Accelerometry is also used in canine locomotion studies. For instance, in the a study conducted by Jenkins et al. a single wearable inertial sensor, mounted above the carpal joint on the lateral side of the fore-limb, was used to determine and then automate the temporal gait characteristics in canines. Their results were manually validated with the HFR videos of the canines and showed acceptable accuracy [61]. In another study conducted by Rhodin et al. [62] an inertial sensor-based system is used in canines to detect and quantify induced moderate lameness as well as differences between supporting and swinging limb lameness. It has been proven in Alvarez et al. study that canine lameness can be detected by measuring the vertical head and pelvic movement [63]. However, motion-capturing methods are time-consuming and are mostly limited to the laboratory environment. The results of the Rhodin et al. study showed that by using three inertial based sensors attached to the mid-line of the top of the head, the mid line of the spinous processes of the second sacral vertebra and the dorsal surface of the metacarpal bones of the forelimb, the moderate induced lameness in canines can be detected and quantified [62]. In a similar study conducted by Ladha et al. [64], an IMU equipped with a tri-axial accelerometer and gyroscope coupled with a standardised walking course, was used to detect canine lameness. The unit was then attached to each leg of the dog for data collection. The results showed that the unit was capable of precisely delineating the step time as well as the toe-touch and toe-lift. Gerencsér et al. also used a single inertial sensor to characterise the locomotion behavior in freely moving dogs [65].

Britt et al. also used a commercial IMU (Blackthorn K9 Equipment Inc.) embedded on a vest equipped with GPS sensor, magnetometer, gyroscope and accelerometer for real-time position and orientation tracking of canines [66].

Despite the advantages of IMU in gait analysis, mainly the usability of the device in challenging dynamics, it has a couple of disadvantages. For instance, IMUs are computational heavy, have to be attached to the object body which may cause discomfort, are not as accurate as force-platforms and need calibration before each test. More importantly, power limitation is one of their most significant limitations [67–69].

2.6.3 SLIP model to simulate legged locomotion dynamics

Apart from experimental methods used to study the effect of the surface on the locomotion dynamics, the SLIP model (illustrated in Figure 2.7) is the simplest and an one of the most extensively used methods addressing legged locomotion in humans, animals and robots [70, 71]. It consists of a mass, located at the CoM of the system and usually massless compliant legs [72, 70]. The SLIP model, which was introduced by Blickhan [72], was an extension of the inverted-pendulum models designed earlier by Cavagna & Kaneko [73].

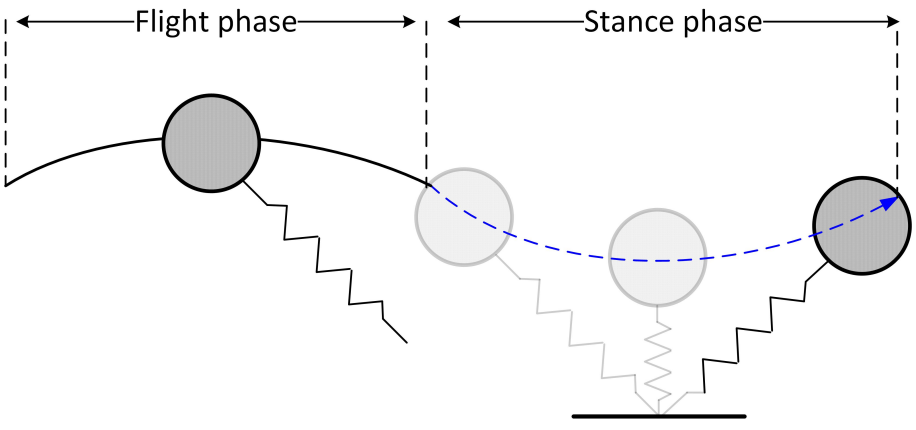

Figure 2.7 : A simple SLIP model.

Gayer et al. showed that, owing to the behavior of compliant legs, a simple bipedal SLIP model is capable of simulating different varieties of gaits such as walking [70] and running [74, 75]. Moreover, SLIP models are also capable of explaining

the dynamics of legged motion both during stance and flight (when no legs are on the ground). For instance, recently the SLIP model was used to explain swing leg kinetics during human walking gait [76].

SLIP models are widely used in designing legged mechanisms such as quadruped robots. Raibert was among the first pioneers who used a SLIP model in designing legged robots [77]. His work provided a vantage point in designing the recent complicated quadruped robots in the literature [78–97].

Equation of motion (EOM)

We mentioned that SLIP models are the best way to mimic the multi degree-of-freedom (DOF) systems of legged mechanisms. We also introduced the SLIP model i.e. a lumped mass representing the body mass and massless liner springs illustrated in Figure 2.7. In this section, we review the methods used to obtain the equation of motion (EOM) of the multi-DOF system which is deployed in this dissertation.

Newton's second law to derive EOM

Most of the discussion in the following sections is from the Rao and Yap study [98]. The procedure below can be used to derive the EOM using Newton's second law:

- Determine a suitable set of coordinates describing the positions of the various point masses and rigid bodies in the system. Assume proper positive directions for the displacements, velocities, and accelerations of the masses and rigid bodies.

- Determine the static equilibrium configuration of the system and measure the displacements of the masses and rigid bodies from their respective static equilibrium positions.

- Draw the free-body-diagram (FBD) of each mass/rigid body in the mechanism. Indicate the spring, damping, and external forces acting on each mass or rigid body when positive displacement and velocity are given to them.

The Newton's second law of motion should then be applied to each mass/rigid body as follows

$$m_i\ddot{x}_i = \sum_j^{\infty} F_{ij} \tag{2.2}$$

or

$$m_i\ddot{\theta}_i = \sum_j^{\infty} M_{ij} \tag{2.3}$$

where $\sum_j^{\infty} F_{ij}$ represents the sum of all the external forces acting on mass m_i and $\sum_j^{\infty} M_{ij}$ denotes the sum of moments of all the external forces acting on the rigid body of moment of inertia J_i.

Lagrange's equation to derive EOM

The equations of motion of a multi-DOF system can be simply obtained in terms of generalized coordinates using Lagrange's equations. Lagrange's equations for an n-DOF system can be stated as follows:

$$\frac{d}{dt}\left(\frac{\partial T}{\partial \dot{q}_j}\right) - \frac{\partial T}{\partial q_j} + \frac{\partial V}{\partial q_j} = Q_j^{(n)} \tag{2.4}$$

where T is the kinetic energy of the system, V is the potential energy of the system, $\dot{q}_j = \partial q_j/\partial t$ is the generalised velocity, and $Q_j^{(n)}$ is the non-conservative generalised force that corresponds to the generalised coordinate [98]. The results of Equation 2.4 are a couple of ordinary differential equations (ODE) which can be solved by different numerical methods such as the Runge-Kutta method [99, 100].

2.7 Summary

The literature relevant to this work have been reviewed in this chapter. Common career-ending injuries as well as important risk factors, were discussed in detail. Track surface and turning were introduced as the most important track-related risk factors. Although the surface compositions have been studied to some extent, there is a big gap in analysis of the interaction of body and underneath terrain in high speed gaits. Methods of studying body-surface interaction, namely using surface impact test devices, force-plates, deploying IMU and simulation through the SLIP

method, were discussed in detail. The gaps identified within this chapter set the stage for the current study presented in this dissertation. Chapter 3, we present our analysis of two years worth of injury data (from January 2016 to December 2017), obtained from NSW greyhound racing tracks to see if a similar pattern is also seen in NSW greyhound race tracks. Chapter 4 sets out our studies of the effect of moisture level and rates of compaction on sand samples provided from a typical greyhound race track and also an analysis of the impact behaviour of the sample, using a standard impact test. In Chapter 5 covers our analysis of the acceleration data of greyhounds galloping on two tracks with different surface types using a single IMU. In chapter 6, we simulated the leg-surface interaction of galloping greyhounds which was then verified with experimental data.

Chapter 3

A Retrospective study of severe injuries in racing greyhounds

3.1 Introduction

The purpose of the data analysis detailed in this chapter was first to find the most common type of severe race-related injuries and second to determine the location on the track where most of the injuries were happening. Based on the reviewed literature, tarsal fractures of the right hind-leg (from now on the right hock) account for most of the casualties in greyhound racing with most of them happening on bends.

Accordingly, the injury data of racing greyhounds on NSW tracks (34 tracks in total) from January 2016 to December 2017, collected by qualified OTVs, were analysed. The injury severity score (ISS) and levels are introduced in Section 3.2.1, and the results are provided in Section 3.3.1. To determine where most of the severe injuries were happening on the track, the race videos were observed in conjunction with the injury data. The results are provided in Section 3.3.2.

The results showed that right hock injuries accounted for more than one-fourth (35%) of the total casualties in both 2016 and 2017. The right hind-leg itself was 41% and 44% of the total number of Level 2 [1] injuries in 2016 and 2017, respectively. Analysing the race videos showed that most of the injuries occurred on bends and mostly on the first bend after the start. Finally, almost 40% of the deaths due to right hock injuries happened on bends in both 2016 and 2017.

[1] Refer to Section 3.2.1 for the definition of the injury levels

3.2 Methods

To find the most frequent type and location of life-threatening injuries, the injury data collected by OTVs, during 2016 and 2017 were analysed. The ISS and injury levels are given in Section 3.2.1. To determine a location on the track where most of the injuries were happening, we observed the race videos [2].

3.2.1 Injury data analysis

Injury severity in the greyhound racing industry in Australia is defined through stand-down periods (number of days that greyhounds have been incapacitated) and injury type. We have tabulated the ISS and injury levels in Table 3.1 and 3.2, respectively.

Table 3.1 : Injury severity score.

Severity	Incapacitation Period	Typical Injury Types
Minor Class I	0 days	Grade 1 muscle injury
Minor Class II	1-10 days	Mild skin laceration
Medium	11- 21 days	Grade 2 muscle injury
Major	Greater than 21 days	Grade 3 muscle injury and bone fracture
Catastrophic	Deceased or euthanized	Severe skull or spinal injury/joint fracture

Table 3.2 : Injury levels.

Injury Level	Definition
Level 1	Catastrophic
Level 2	Catastrophic and Major
Level 3	Catastrophic, Major and Medium
Level 4	Catastrophic, Major, Medium and Minor

[2]The race videos are available at <www.thedogs.com.au>.

3.2.2 Race video analysis

The available videos of race meetings from January 2016 to December 2016 were viewed to determine the injury location on race tracks. This was done in conjunction with injury data analysis to minimise human error. However, on some occasions, identifying where precisely the injury had occurred was impossible, so the location was categorised as 'Unknown injury location'.

3.3 Results and discussion

There was a total of 546 and 537 Level 2 musculoskeletal injuries in 2016 and 2017, respectively. The anatomical injury severity (AIS) in both years, is given in the form of pie charts in Section 3.3.1.

The injury occurrence frequency can be represented through plotting the schematic diagram of the race track where the injuries are illustrated as 'dots' in different colours. The location with the highest proportion of the dots is the hazardous location of the track.

A total of thirteen tracks with available race videos are included, and the results are given in Section 3.3.2. Additionally, we checked whether specific types of injuries tended to happen more frequently in particular locations on the track. The results are tabulated in Tables 3.5 to 3.8.

3.3.1 Level 1 and 2 injuries AIS

The Level 1 and 2 AIS in 2016 are plotted in Figure 3.1 and 3.2, respectively. The injuries were divided into five different groups: left fore-leg; right fore-leg; left hind-leg; right hind-leg; and others.

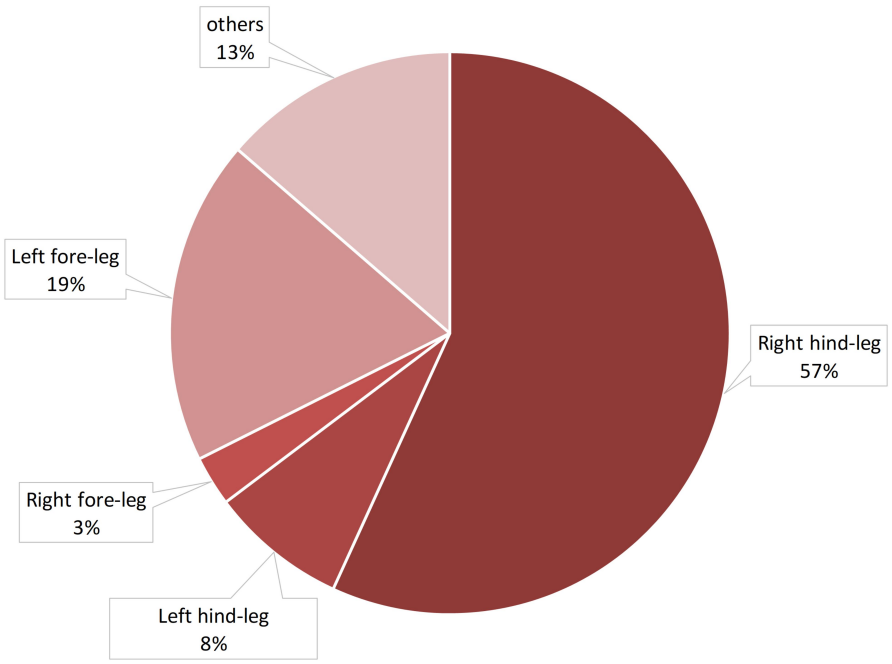

Figure 3.1 : AIS of Level 1 injuries of greyhound racing tracks in NSW, 2016.

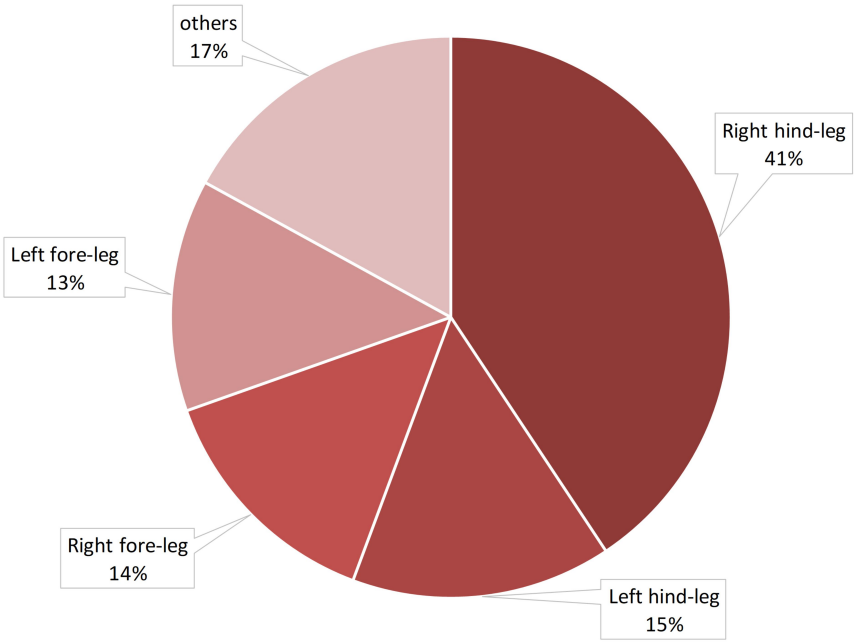

Figure 3.2 : AIS of Level 2 injuries of greyhound racing tracks in NSW, 2016.

The Level 1 and Level 2 AIS in 2017 are plotted in Figure 3.3 and 3.4.

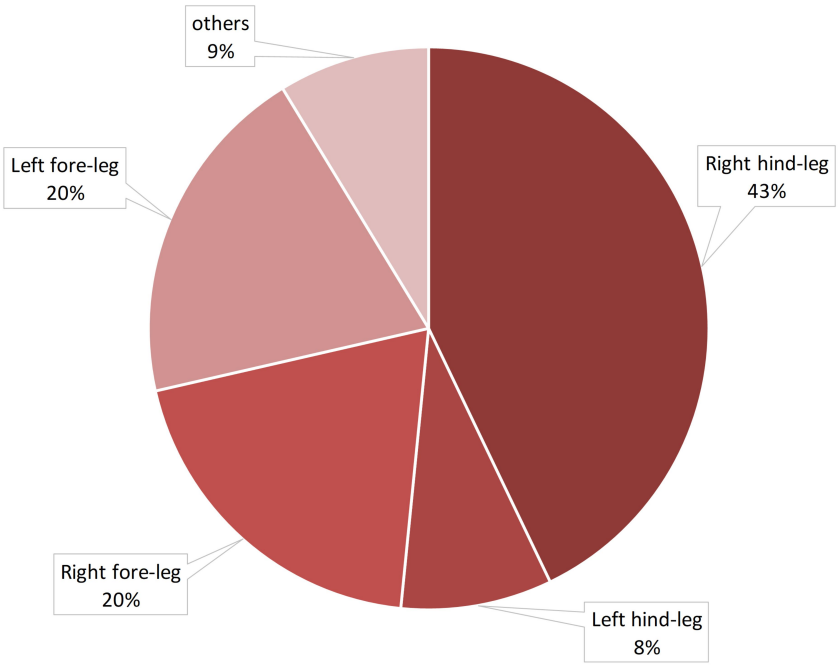

Figure 3.3 : AIS of Level 1 injuries of greyhound racing tracks in NSW, 2017.

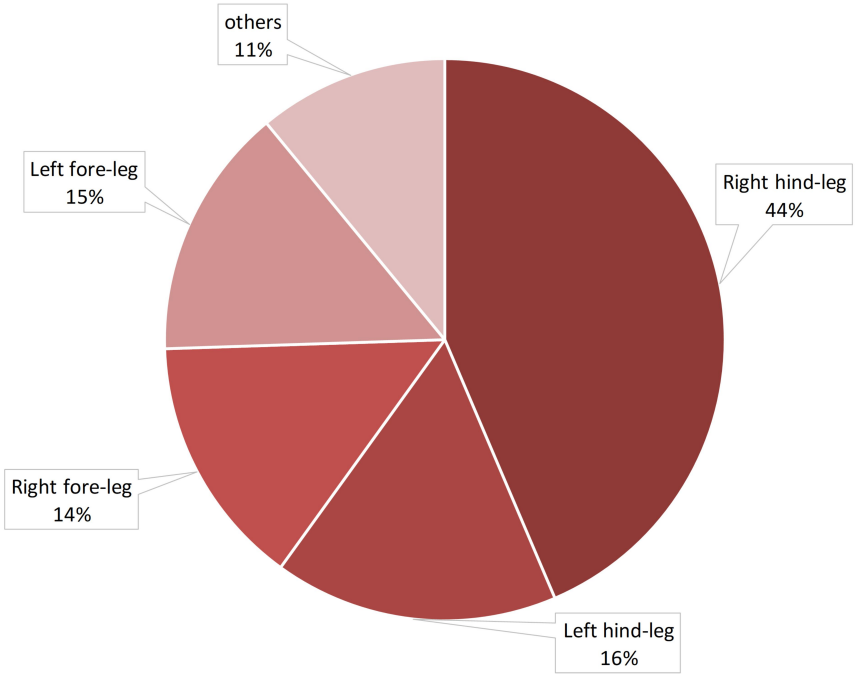

Figure 3.4 : AIS of Level 2 injuries of greyhound racing tracks in NSW, 2017.

It can be seen that the right hind-leg injuries accounted for 57% and 41% of the total Level 1 and 2 injuries in 2016, sequentially. Similarly, right hind-leg injuries accounted for 43% and 44% of the total Level 1 and 2 injuries in 2017. These findings

correlate well with the literature [3, 16, 17, 28].

More details on Level 1 and 2 right hind-leg injuries in 2016 are given in Table 3.3. Hock fracture/sprain accounted for 39% of Level 2 and 82% of Level 1

Table 3.3 : Level 1 and 2 right hind-leg injury type in 2016. Not applicable is abbreviated as NA.

Injury type	Level 2 injuries	Level 1 injuries
Tarsal (hock) fracture/sprain	**87**	**51**
Gracilis tear	73	1
Tensor fascia latae tear/strain	20	NA
Metatarsal fracture	12	2
Toe fracture/dislocation	10	1
Pectineus injury	8	NA
Fibula fracture/sprain	4	NA
Gastrocnemius tear/strain	2	NA
Long-bone fracture	2	11
Achilles tendon tear/strain	1	NA

injuries. The top three most frequent Level 2 injury types in 2016 were the right hock fracture/sprain, *gracilis* tear and tensor *fascia latae* tear/strain.

The type and number of Level 1 and 2 right hind-leg injuries in 2017 are tabulated in Table 3.4. The hock fracture/sprain accounted for 41% of Level 2 and 79% of Level 1 respectively. The top three common injury types in 2017 were similar to 2016.

We mentioned in Chapter 2 that the top severe injuries in racing greyhounds are the right hock and *gracilis* muscle injuries. As is evidenced above, our results are in excellent agreement with the literature.

3.3.2 Hazardous location on the race track

To determine the location of injuries on the race track, which in most cases were not given (59% of all the injuries in two years had an 'unknown' injury location), we observed the available race videos of the associated injuries.

Table 3.4 : Level 1 and 2 Right hind-leg injury type in 2017. Not applicable is abbreviated as NA.

Injury type	Level 2 injuries	Level 1 injuries
Tarsal (hock) fracture/sprain	**98**	**43**
Gracilis tear	65	NA
Tensor fascia latae tear/strain	22	NA
Pectineus injury	11	NA
Toe fracture/dislocation	9	NA
Metatarsal fracture	6	3
Hamstrings injury	4	NA
Gastrocnemius tear/strain	3	NA
Stifle injury	3	1
Gluteals injury	2	NA
Tibia fracture	2	1
Split webbing	1	NA
Biceps femoris injury	1	NA
Femur fracture	1	1
Sartorius injury	1	NA
Unknown	4	4

Figures 3.5 to 3.11 show injury locations for thirteen greyhound racing tracks in NSW with red, yellow, blue and green dots representing catastrophic, major, medium and minor injuries, respectively. We only plotted race distances with a high number of race meetings. The number of dots on each diagram does not represent the precise number of injuries on each track.

The following criteria were followed in plotting the injury locations plots:

- The injury was a direct cause of an incident (collision) in this particular location;
- The injury was an indirect cause of the incident, i.e. greyhounds being hampered by another greyhound causing loss of balance and an incident in this particular location;
- The greyhound 'apparently' slowed down or limped/stopped in this particular location (this may imply the injury was worsened because of an excessive force

acting on the limbs).

If none of the above conditions was recognised, the injury location was categorised as 'unknown injury location'.

Figure 3.5 shows the injury locations for the Bathurst (race distance of 307 m) and Bulli tracks (race distance of 400 m). In both tracks, most of the injuries occurred on a bend, mainly the first bend after the start.

The injury locations for Dapto (race distance of 520 m) and Dubbo (race distance of 318 m) are plotted in Figure 3.6. In both tracks, the high proportion of injuries occurred on bends, mainly the first bend after the start.

The injury locations for Gosford (race distance of 515 m) and Goulburn (race distance of 350 m) tracks are plotted in Figure 3.7. As can be seen, most of the injuries have happened on the first turn after the start.

The injury locations for Grafton (race distance of 407 m) and Lismore (race distance of 520 m) tracks are illustrated in Figure 3.8. Most of the injuries occurred on the first bend after the start in both tracks.

The injury location for Maitland (race distance of 450 m) and Nowra (race distance of 520 m) tracks are plotted in Figure 3.9. It can be seen that most of the injuries happened on the bends after the start.

The location of injuries for the Richmond (race distance of 535 m) and The Gardens (race distance of 515 m) tracks are given in Figure 3.10. Injuries mostly occurred on the first bend on both tracks.

The injury location for Wentworth Park track (race distance of 520 m) is given in Figure 3.11. The highest number of injuries happened on the first bend after the start.

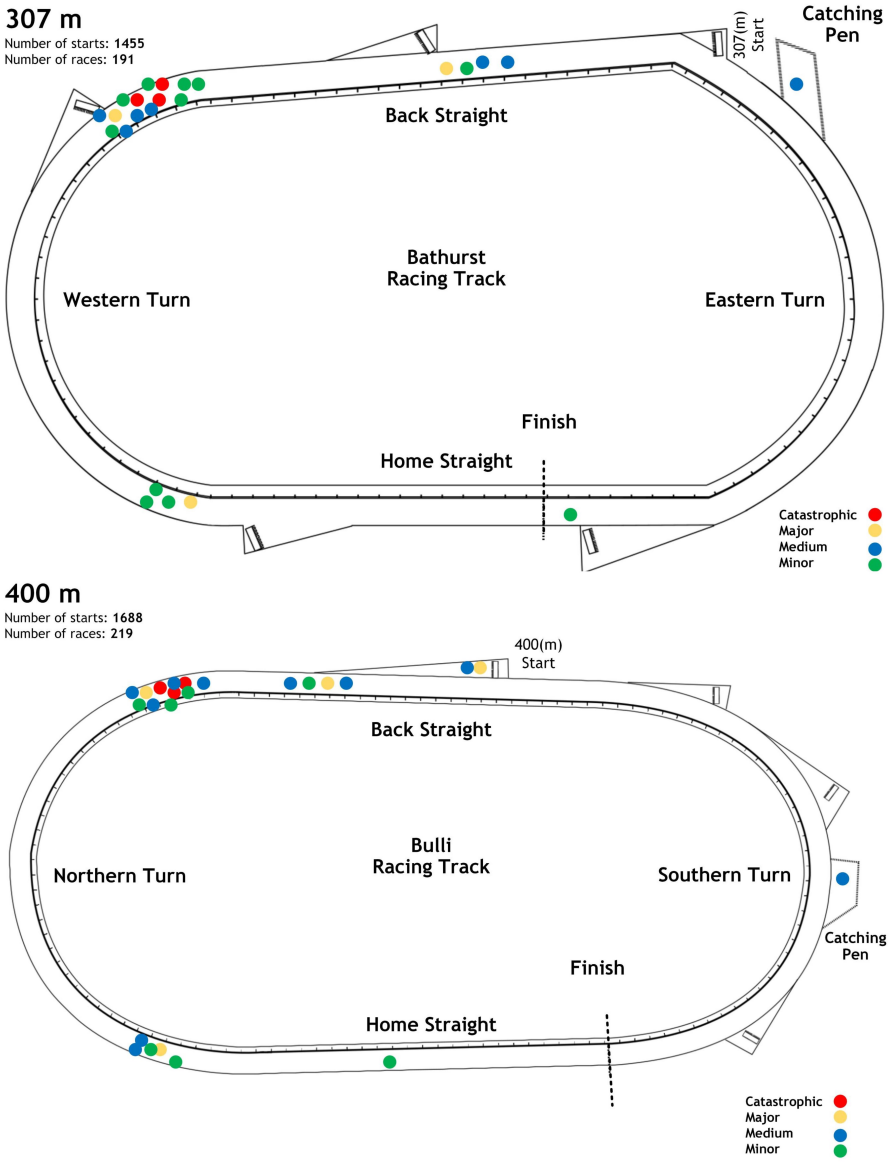

Figure 3.5 : Injury location graphs for Bathurst 307 m and Bulli 400 m race distances. Red, yellow, blue and green dots represent catastrophic, major, medium and minor injuries, respectively.

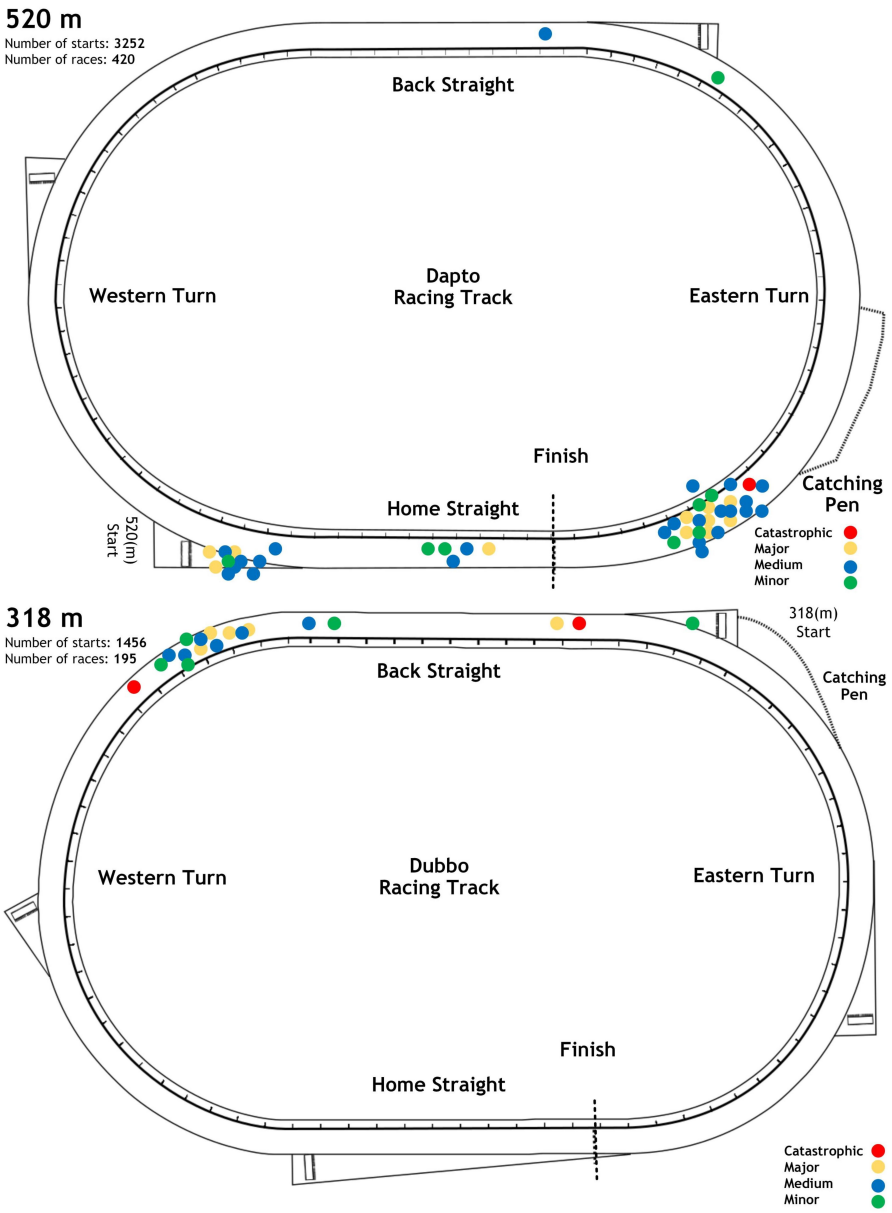

Figure 3.6 : Injury location graphs for Dapto 520 m and Dubbo 318 m race distances. Red, yellow, blue and green dots represent catastrophic, major, medium and minor injuries, respectively.

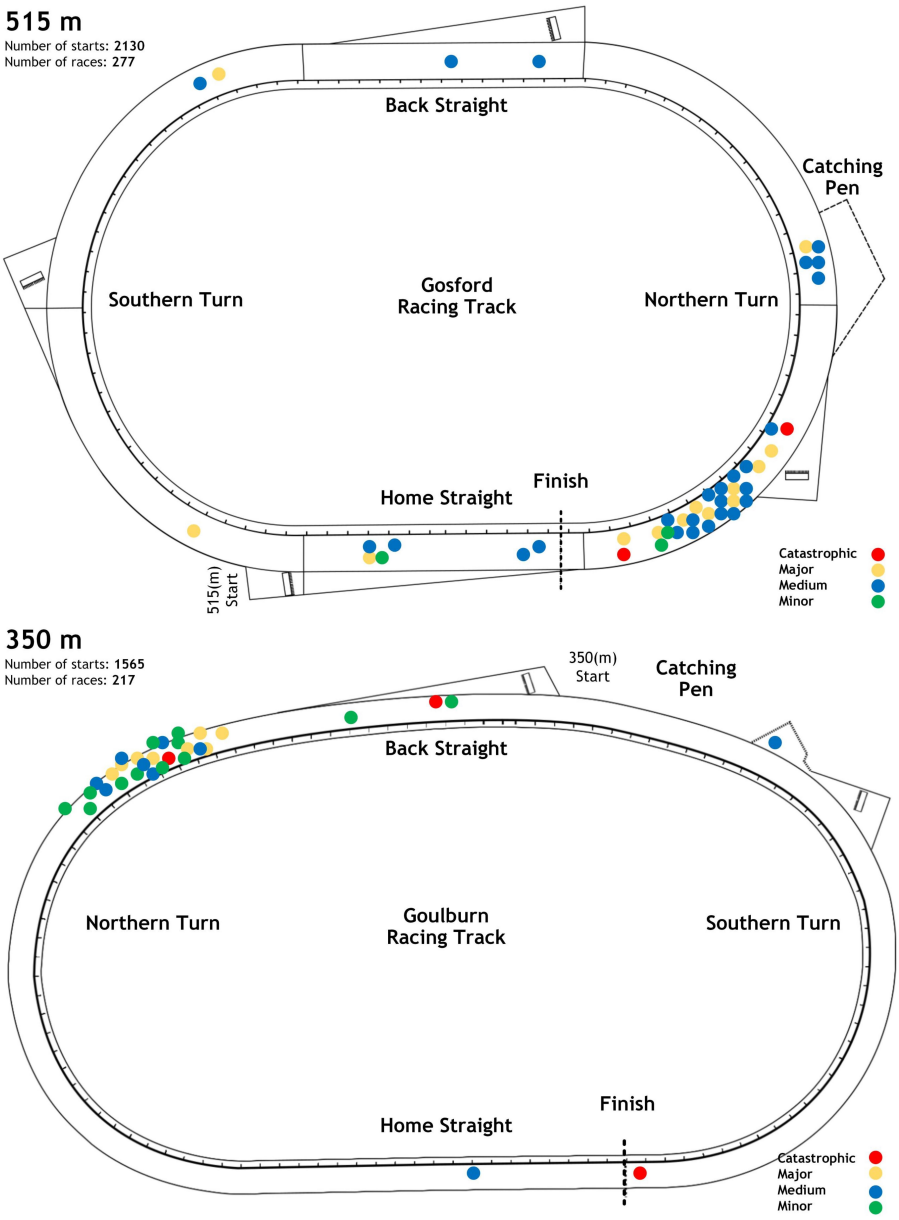

Figure 3.7 : Injury location graphs for Gosford 515 m and Goulburn 350 m race distances. Red, yellow, blue and green dots represent catastrophic, major, medium and minor injuries, respectively.

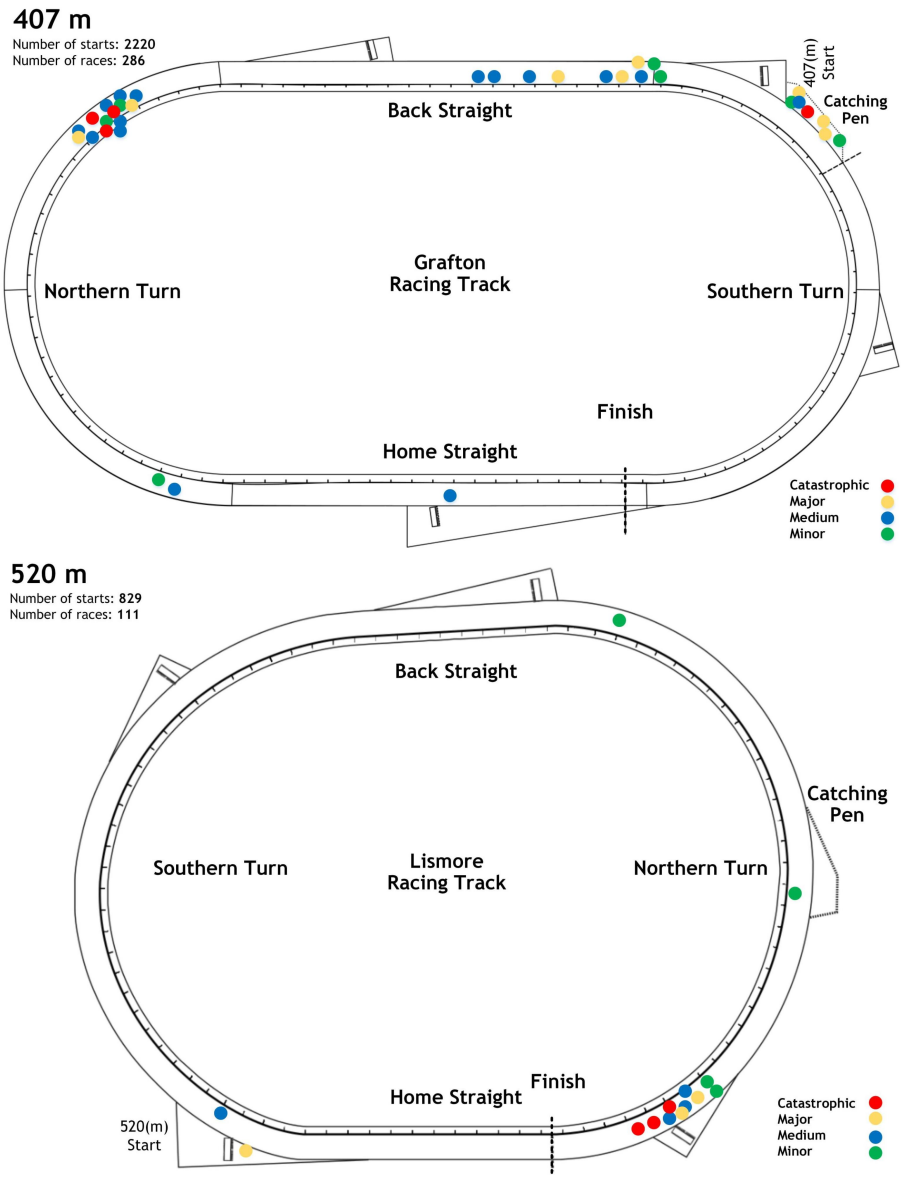

Figure 3.8 : Injury location graphs for Grafton 407 m and Lismore 520 m race distances. Red, yellow, blue and green dots represent catastrophic, major, medium and minor injuries, respectively.

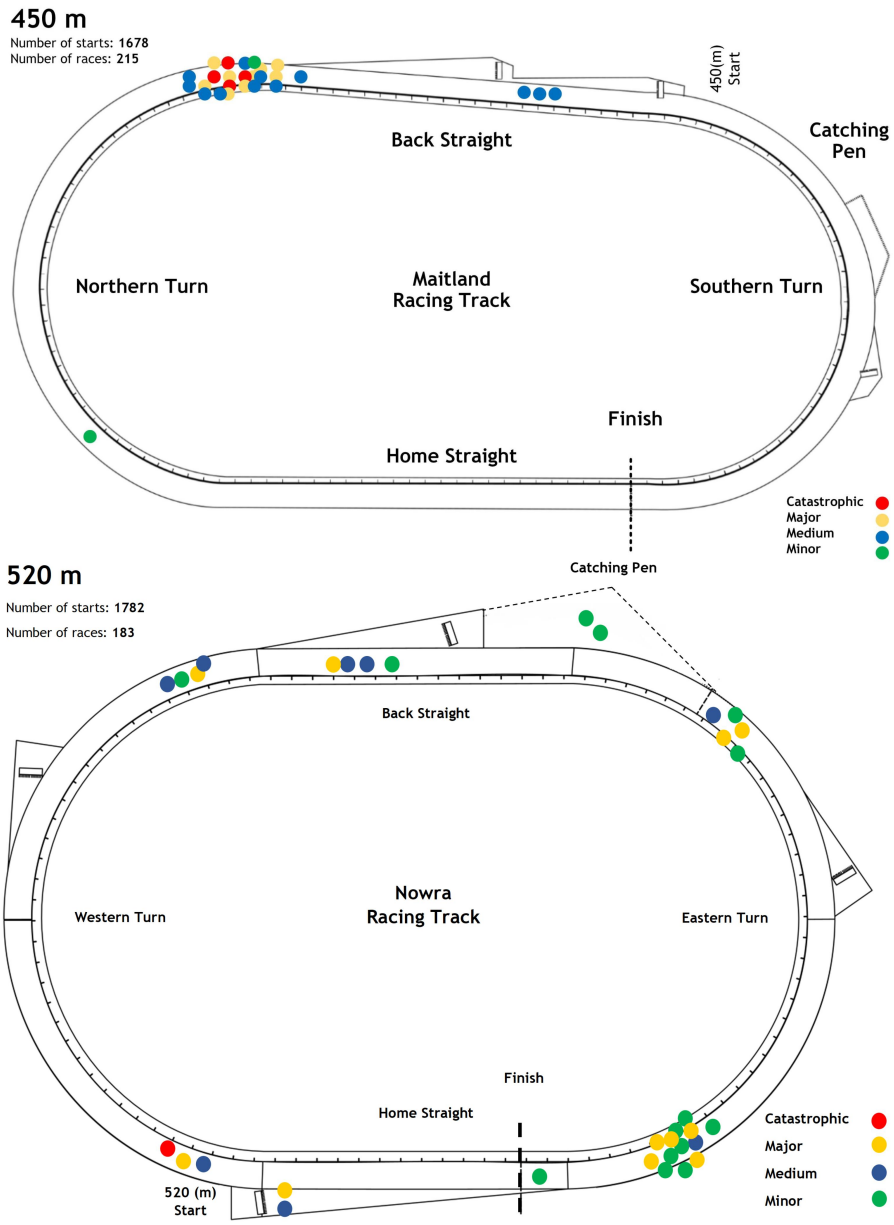

Figure 3.9 : Injury location graphs for Maitland 450 m and Nowra 520 m race distances. Red, yellow, blue and green dots represent catastrophic, major, medium and minor injuries, respectively.

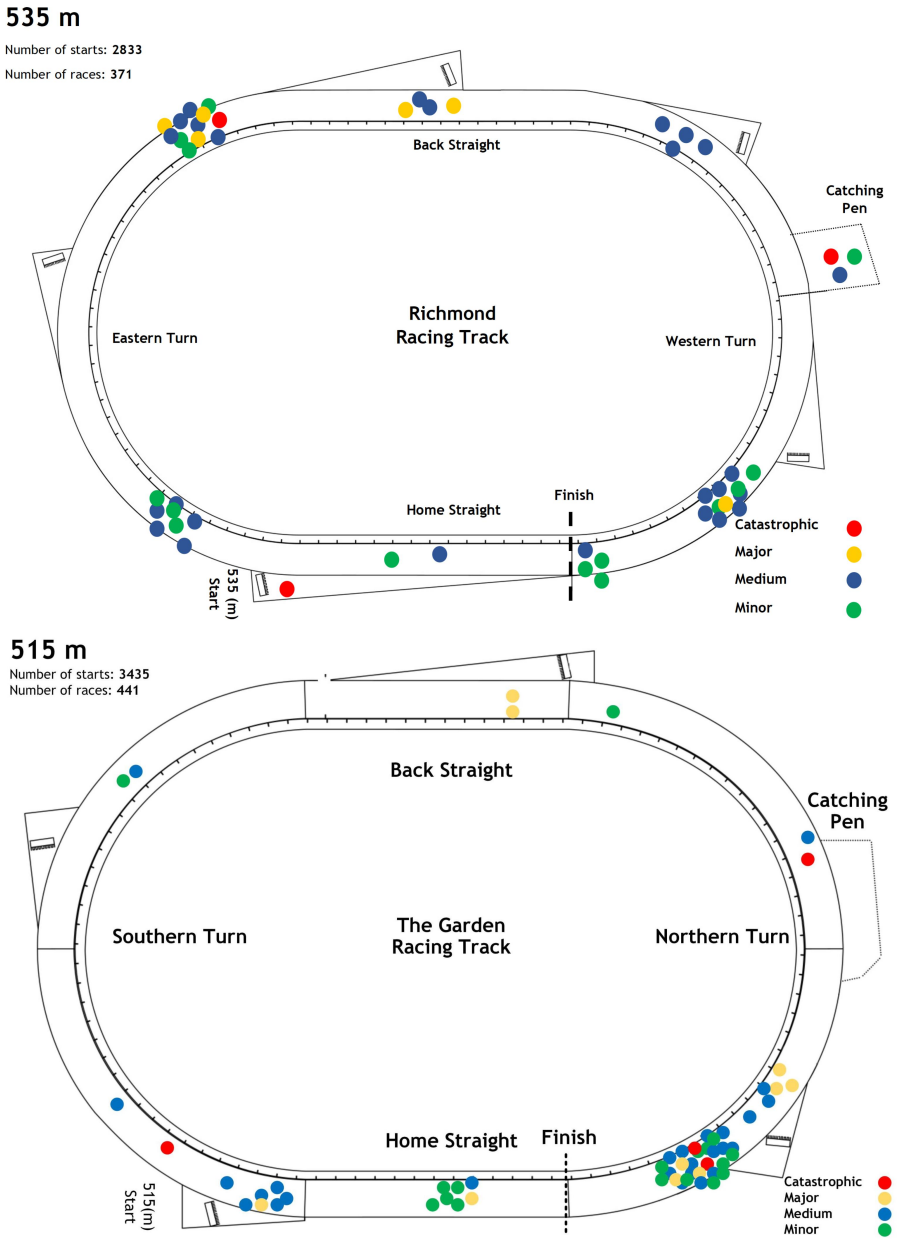

Figure 3.10 : Injury location graphs for Richmond 535 m and The Gardens 515 m race distances. Red, yellow, blue and green dots represent catastrophic, major, medium and minor injuries, respectively.

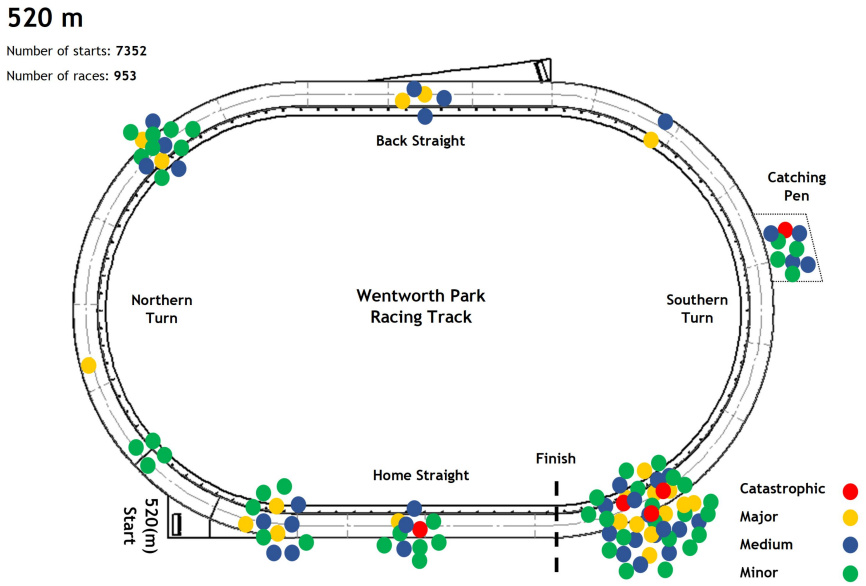

Figure 3.11 : Injury location graphs for Wentworth Park 520 m race distance. Red, yellow, blue and green dots represent catastrophic, major, medium and minor injuries, respectively.

We observed that most of the injuries occurred on the first bend after the start, which is in agreement with previous literature advising the significant difference between the number of incidents on the first bend and on the other bends [22, 27].

The total number and percentage of right hock Level 1 and 2 injuries that happened on bends in 2016, are tabulated in Table 3.5 and 3.6, respectively.

Table 3.5 : Total number and percentage of Level 1 right hind-leg injuries that happened on bends in 2016.

Items	Right hind-leg	Right Hock
Total number	62	51
Injuries occurring on bends	23 (37%)	**20 (39%)**
Unknown location	17 (27%)	12 (23%)

37% of total Level 1 right hind-leg and 39% of total right-hock injuries occurred on bends. Likewise, 31% of total Level 2 right hind-leg and 35% of right-hock injuries occurred on bends as well.

Table 3.6 : Total number and percentage of Level 2 right hind-leg injuries happened on bends in 2016.

Items	Right hind-leg	Right Hock
Total number	222	87
Injuries occurring on bends	69 (31%)	**35 (40%)**
Unknown location	91 (40%)	23 (26%)

Total number and percentage of Level 1 and 2 right hock injuries in 2017 that happened on bends are tabulated in Table 3.7 and 3.8, respectively.

Table 3.7 : Total number and percentage of Level 1 right hind-leg injuries happened on bends in 2017.

Items	Right hind-leg	Right Hock
Total number	54	43
Injuries occurring on bends	20 (37%)	**18 (40%)**
Unknown location	16 (29%)	13 (30%)

Table 3.8 : Total number and percentage of Level 2 right hind-leg injuries happened on bends in 2017.

Items	Right hind-leg	Right Hock
Total number	231	98
Injuries occurring on bends	71 (30%)	**37 (37%)**
Unknown location	86 (36%)	25 (25%)

37% of total Level 1 right hind-leg and 40% of right hock injuries occurred on bends. The same pattern was observed for Level 2 injuries as 30% of total Level 2 right hind-leg and 37% of right-hock injuries occurred on bends.

Sicard et al. also noted the same trend in hock injuries. They observed that unlike other injuries which were randomly distributed over the race track, the hock injuries (did not specify the left or the right side), occurred on the first bend [27].

As stated in the literature, bend radius is an important risk factor as a high rate of acceleration and change of the rate of acceleration (jerk) [29] are applied to greyhounds' limbs while turning. The extreme force upon contact of one paw in rotatory galloping gait [30] makes greyhounds even more prone to sustain injuries while turning than a human sprinter.

Furthermore, greyhound congestion is another reason that most of the injuries are happening on the bend section as argued by Ireland [25]. We observed a similar trend in the videos with most of the injuries happening on the first bend after the start. Based on the race videos most of the injuries were occurring as a result of the clustering of greyhounds towards the inner rail on the first turn. Clustering can result from various track related parameters such as short mechanical lures biased towards the inner rail [37], the high number of greyhounds in each race, insufficient camber, and lack of transition from straight sections to bends.

3.4 Summary

In this chapter two years injury data and race videos from January 2016 to December 2017, were analysed to identify frequent types of severe injuries and determine hazardous locations on the race track. The results showed that the right hock had the highest number of Level 1 and 2 injuries and was mostly happening on bends. These findings draw attention to right hock dynamics and their interaction with the track surface which was studied through the SLIP method. Results are presented in Chapter 5. Another interesting observation was the considerable difference between the right and left hind-leg in respect of the number of injuries. The left hind-leg only accounted for 15% and 16% of the Level 2 injuries in 2016 and 2017, respectively. These results provide enough evidence for future research on the differences between right and the left hind-legs dynamics.

Chapter 4

Dynamic behaviour of greyhound track surfaces

4.1 Introduction

It was shown in Chapter 2 that the track surface is a critical risk factor in the greyhound racing industry. Analysis of injury data and race videos of racing greyhounds in Chapter 3, showed that there is a similar trend in the data. It was observed that most of the casualties occured on bend sections in the track. The right hind-leg in particular accounted for most of the severe injuries.

Although the track surface is known as an influential parameter contributing to injuries, there is a big gap in understanding the limb-surface biomechanics. The first step towards filling this gap is to identify the variables that change the dynamic behaviour of the sand surface, as sand is the most frequent type of surfacing in the greyhound racing industry.

Thus, the first aim of the research reported in this chapter was to study the effect of the moisture content and rate of compaction on the dynamic behaviour of the sand surface, as these are two fundamental variables contributing to a safe surface and therefore a safe race. The second aim was to obtain the stiffness coefficient (k_s) of the surface, via a designed impact test. The dynamics of the leg and surface were modelled using the k_s as an input for the SLIP model. Chapter 6 contains the details of this research.

4.2 Methods

The sand sample was collected from Wentworth Park sporting complex, Glebe NSW, with the sand particle sizes and percentages given in Table 4.1. The sample was taken to the University of Technology Sydney Vibration and Solid Mechanics laboratory for further analysis. We hypothesised that altering the sand moisture level

and rate of compaction would change its mechanical properties. In Section 4.2.1, this method is explained in detail. A method to obtain the stiffness coefficient of the surface is also explained in Section 4.2.2.

Table 4.1 : Sand particle sizes and percentages at the Wentworth Park track.

Fraction	Size (mm)	Percentage (%)
Fine gravel	2.00	Trace
Very coarse sand	1.00	3%
Coarse sand	0.50	7%
Medium sand	0.25	25%
Fine sand	0.15	28%
Very fine sand	0.05	33%
Silt/clay	< 0.05	4%

4.2.1 An impact test to study the dynamic behaviour of the sand

The dynamic behaviour of the sand sample was studied by analysing the impact data, namely the maximum acceleration (G_{max}), the maximum rate of change of acceleration (J_{max}), the impact duration (contact time), and the energy loss. These were all obtained by conducting an impact test using a 'modified' Clegg hammer.

The Clegg hammer was developed by Branden Clegg to control the compaction of road materials [42]. The apparatus consists of a guiding tube and a square-faced impacting cylindrical mass. The mass is located inside the tube and is dropped from a standard height onto the surface being tested. The Clegg hammer measures the peak deceleration when the mass comes into contact with the surface in units of $10\times$ gravity [42, 43].

The conventional Clegg hammer does not report some essential impact data. For this reason it was modified to obtain the G_{max} (in units of gravity (G) versus time (ms)). The modifications consisted of replacing the single Clegg hammer accelerometer with two calibrated laboratory-grade Endevco high-G accelerometers. Adding the high-G accelerometers allowed a higher degree of experimental precision and accuracy than that offered by the standard Clegg hammer. The reliability

of the system was tested in previous studies on children's playgrounds for impact attenuation of surfacing [5, 4].

Altering the moisture level and rate of compaction of the sand sample

The effect of three moisture levels (12%, 17%, and 20%) and three rates of compaction (1.35 g/cm^3, 1.45 g/cm^3, and 1.55 g/cm^3), on the dynamic behaviour of the sand sample, were examined here.

The rate of compaction is a representative of the traffic conditions of the racing surface and is affected by greyhound activity that would compact the top surface [45]. Bloomberg advised that in the final races of each event, the surface tends to become compacted which leads to an increases in the chance of hock fracture [26].

The experiment for drying out the sand samples and altering their moisture content complied with AS 1289 Part 2.1.1 Standard [40]. Based on the Standard, the sand sample was heated up in an oven, between 105 to 110° for 16 to 24 hours. The following equation was used to measure the moisture level of the sand:

$$w = \frac{m_b - m_c}{m_c - m_a} \times 100 \tag{4.1}$$

where w is the moisture content of the sand sample, m_b is the mass of the container and wet sand, m_c is the mass of the container and dry sand, and m_a is the mass of container.

Three different moisture levels were simulated here, namely 12%, 17%, and 20%. In order to simulate the low traffic, medium traffic and high traffic conditions of the race track, we followed the procedure explained by Holt et al. [45]. For all three conditions, we used a cylindrical container with an inner diameter of 15.6 cm. The sand was filled at 3.0 cm increments until reaching the depth of 12.0 cm. The average of sand density (the mass of the sand sample divided by its volume) for the simulated traffic conditions was also calculated and given as follows:

- **Low traffic condition:** The top 3.0 cm layer was raked. The average of sand sample density for all moisture contents was 1.35 g/cm^3. This traffic condition

is pictured in Figure 4.1.A.

- **Medium traffic condition:** The top 3 cm top layer was struck with a tamper to achieve the depth of 14 cm. The average of sand sample density for all moisture contents was 1.45 g/cm^3. This traffic condition is pictured in Figure 4.1.B.

- **High traffic condition:** The top 3 cm top layer was struck with a tamper to achieve the depth of 13 cm. The average of sand sample density for all moisture contents was 1.55 g/cm^3. This traffic condition is pictured in Figure 4.1.C.

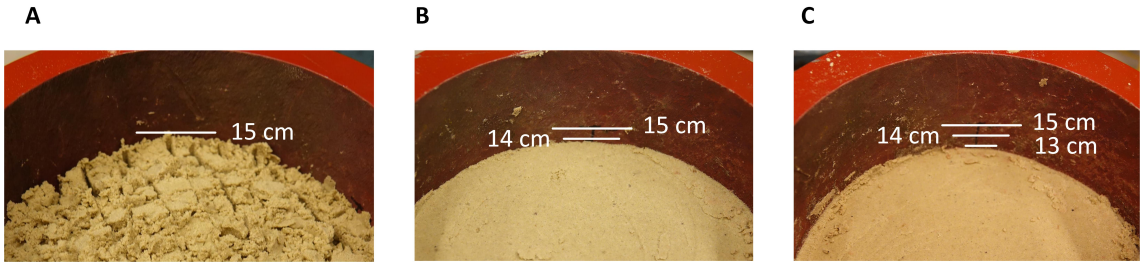

Figure 4.1 : A low traffic condition with the density of 1.35 g/cm^3 (A). A medium traffic condition with the density of 1.45 g/cm^3 (B). A high traffic condition with the density of 1.55 g/cm^3 (C).

It should be noted that the tampering was manual which means there was no control over the applied force. Therefore, achieving a certain depth was the only possible control we could apply.

After preparing the sand sample, an impact attenuation test, which complied with the Standard [46], was conducted from three different heights, namely: 400 mm, 500 mm and 600 mm. Based on the Standard, the test was repeated four times from each height, and the maximum value was reported i.e. the maximum value for G_{max}, J_{max} and contact time. After the fourth drop at each height in the same location, the sand sample was reconstructed to avoid the effect of over compacting of the lower layers on the results. The impact attenuation data were then post-processed using LabVIEW software and plotted in MATLAB R18. The experimental setup is illustrated below in Figure 4.2.

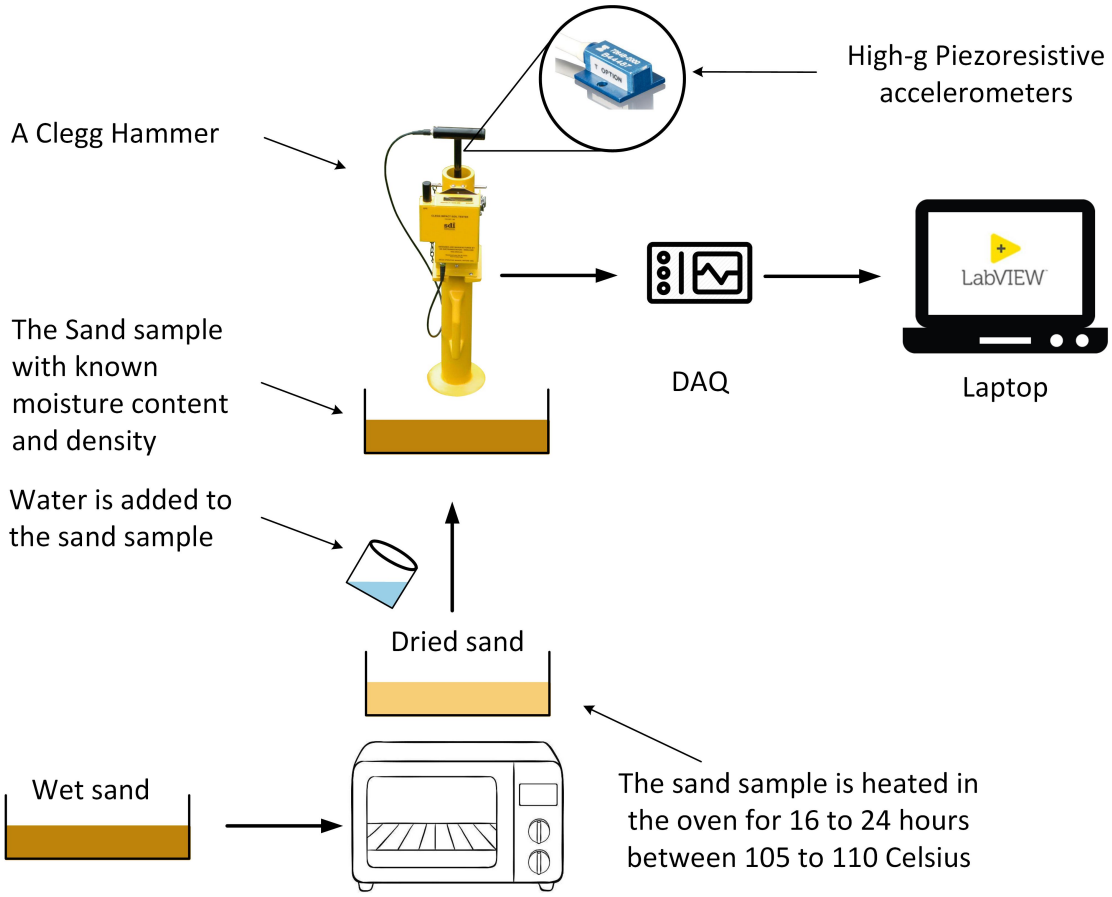

Figure 4.2 : The process of drying out the sand sample, altering the moisture content and the impact test using a modified Clegg hammer.

4.2.2 Obtaining the stiffness coefficients of the sand samples

The stiffness coefficient (k_s) of any compliant surface can be by fitting a line on the 'loading' phase of the load-deformation plots. This method was also adopted by Aerts & Clercq [101] in analysing the performance of athletic shoes with hard and soft soles.

The sand surface penetration (displacement) can be calculated by double integration of the impact acceleration with respect to the impact time. This procedure was carried out for all the sand samples in all the simulated conditions, and the results were plotted further in Section 4.3.2.

4.3 Results and discussion

4.3.1 Effect of moisture content and rate of compaction on the dynamic behaviour of the sand sample

Figure 4.3 shows the impact acceleration versus time of the sand sample with three different moisture levels and rates of compaction. The peak of each impact acceleration is the maximum acceleration (G_{max}). The red, blue and black lines represent 400 mm, 500 mm and 600 mm drop heights, respectively.

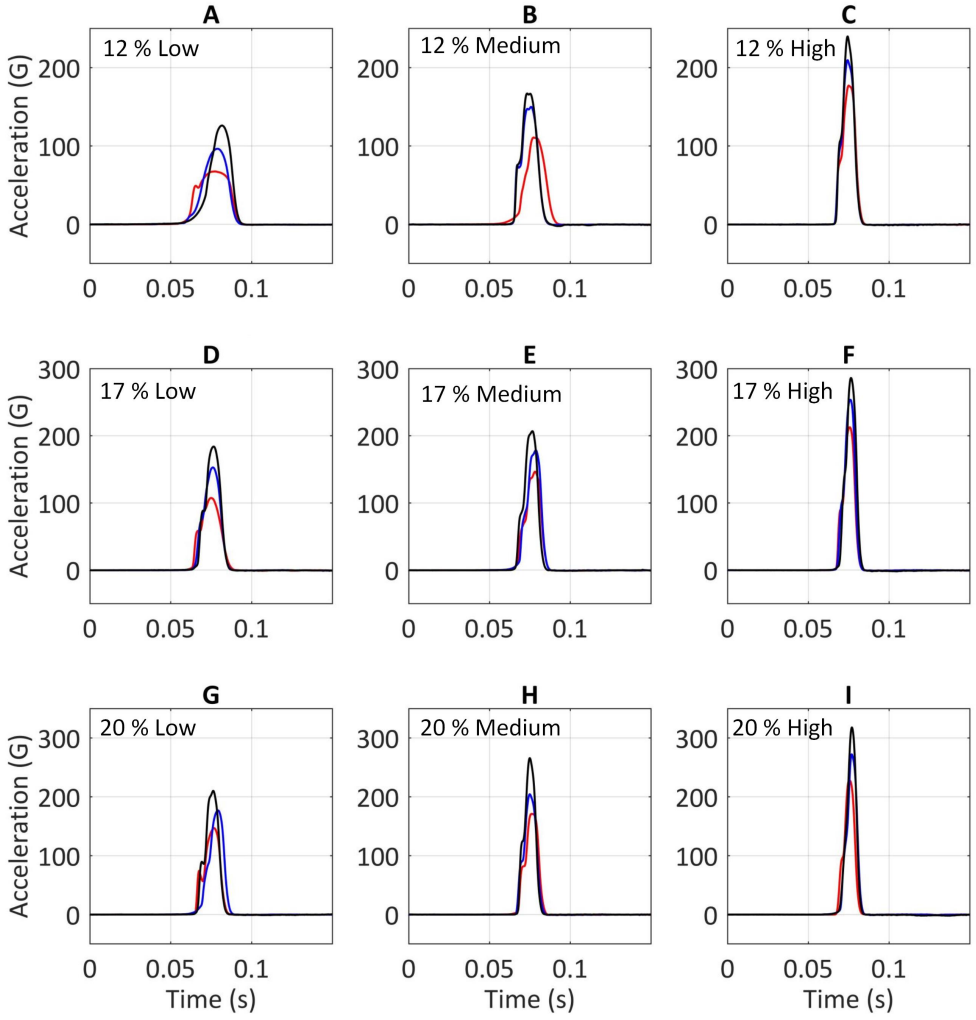

Figure 4.3 : The G_{max} versus time of the sand samples with different moisture levels and rates of compaction. The red, blue and black lines represent the drop height of 400 mm, 500 mm and 600 mm, sequentially.

Figure 4.3 A, B and C show the impact acceleration versus time of the sand sample with 12% moisture level, in low, medium and high traffic conditions, respectively. For the density of 1.35 g/cm^3, increasing the drop height from 400 mm to 500 mm, and 500 mm to 600 mm resulted in 43% and 40% increase of the G_{max}, respectively. Likewise, for the density of 1.45 g/cm^3, increasing the drop height from 400 mm to 500 mm, and 500 mm to 600 mm resulted in 12% and 35.5% increase of the G_{max}, respectively. Finally, for the density of 1.55 g/cm^3, increasing the drop height from 400 mm to 500 mm, and 500 mm to 600 mm resulted in 15% and 14.5% increase of the G_{max}, respectively.

Figure 4.3 D, E and F illustrate the impact acceleration versus time of the sand sample with 17% moisture level, in low, medium and high traffic conditions, respectively. For the density of 1.35 g/cm^3, increasing the drop height from 400 mm to 500 mm, and 500 mm to 600 mm, resulted in 42% and 20% increase of the G_{max}, respectively. Similarly, for the density of 1.45 g/cm^3, increasing the drop height from 400 mm to 500 mm, and 500 mm to 600 mm, resulted in 21% and 16% increase of the G_{max}, respectively. Finally, for the density of 1.55 g/cm^3, increasing the drop height from 400 mm to 500 mm, and 500 mm to 600 mm, resulted in 19.3% and 13% increase of the G_{max}, respectively.

Figure 4.3 G, H and I show the impact acceleration versus time of sand sample with 20% moisture level, in low, medium and high traffic conditions, respectively. For the density of 1.35 g/cm^3, increasing the drop height from 400 mm to 500 mm and from 500 mm to 600 mm, resulted in 20% and 19% increase of the G_{max}, respectively. For the density of 1.45 g/cm^3, increasing the drop height from 400 mm to 500 mm and from 500 mm to 600 mm, resulted in 19.5% and 31% increase of the G_{max}, respectively. Finally, for the density of 1.55 g/cm^3, increasing the drop height from 400 mm to 500 mm and from 500 mm to 600 mm, resulted in 19.4% and 16.7% increase of the G_{max}, respectively.

Increasing the drop height increased the velocity at the time of the impact and as discussed above, the higher the initial impact velocity, the higher the value of the G_{max}. This reveals the rate dependency of the sand [47].

Statistical analysis

In order to assess whether surface treatments have a 'significant' effect on the dynamic behaviour of the sand sample, we compared the impact data from a drop height of 500 mm, for all the moisture levels and rates of compaction, which are tabulated in Table 4.2. An ANOVA test (two-factor with replication) was conducted. Values of $P \leq 0.05$ were considered statistically significant.

Table 4.2 : Impact data from conducting a drop test on the sand sample.

Treatments	G_{max} (G)	J_{max} (G/s)	Time (ms)	Energy loss (J)	k (kN/m)
12%-Low	96.2	43.4k	6.7	46.1	16.7
12%-Medium	149.8	87.1k	4.2	32.9	35.2
12%-High	176.9	117k	3.5	34.4	57.9
17%-Low	152.7	75.9k	4.7	36.4	31.3
17%-Medium	178.2	93.1k	4.8	39.5	44.3
17%-High	253.6	174k	3.1	40.9	84.5
20%-Low	176.7	91.7k	5.0	31.9	38.8
20%-Medium	204.2	129k	3.5	37.3	68.5
20%-High	272.2	205k	3.7	32.2	99.2

There was a significant difference between the values of G_{max} , when the moisture level increased from 12% to 17% [P=0.054 F=4.21]. However, altering the moisture level from 17% to 20%, had no significant effect on the G_{max} values [P=0.11 F=2.79]. Increasing the moisture level from 12% to 17% did not have any significant effect on J_{max} values [P=0.43 F=0.64]. However, changing the moisture level from 17% to 20%, significantly increased the J_{max} [P= 0.043 F=4.72]. The moisture content did not have any effect on the contact time.

Altering the density had a significant effect on the G_{max} [P=0.0003 F=12.9], J_{max} [P=0.00001 F=22.6] and Contact time [P=0.023 F=4.6].

The energy loss or the energy absorbed by the surface is the area under the curve of the load-deformation plots, tabulated in Table 4.2.

Increasing the sand sample density with 12% moisture content from 1.35 g/cm^3 to

1.45 g/cm^3 reduced the energy loss by 28%. In contrast, when the density increased from 1.45 g/cm^3 to 1.55 g/cm^3, it increased the energy loss by 4%.

For the sand sample with 20% moisture content, increasing the sand sample density from 1.35 g/cm^3 to 1.45 g/cm^3 increased the energy loss by 16%. In contrast, when the density increased from 1.45 g/cm^3 to 1.55 g/cm^3, it decreased the energy loss by 15%.

4.3.2 The stiffness coefficient of the sand sample

Figure 4.4 shows load-deformation plots of the sand sample with three different moisture levels and rates of compaction. The slopes of the fitted dashed lines to the loading phases of the superimposed plots is the stiffness coefficient of the sand sample. The red, blue and black lines represent 400 mm, 500 mm and 600 mm drop heights, respectively.

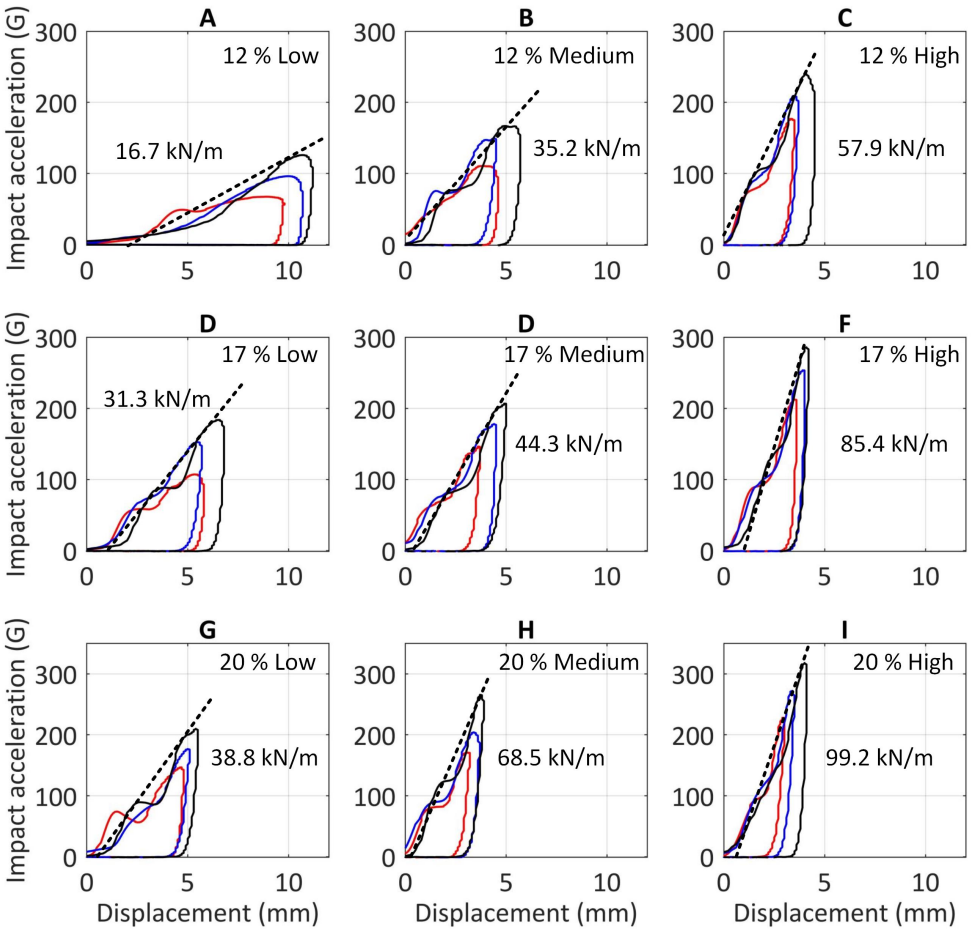

Figure 4.4 : The load-deformation plots of the sand samples with different moisture levels and rates of compaction. The red, blue and black lines represent a drop height of 400 mm, 500 mm and 600 mm, respectively.

Figure 4.4 A, B and C show the load-deformation plots for the sand sample with 12% moisture content in low, medium and high traffic conditions, respectively. The stiffness coefficient increases up to 95% (16.7 kN/m to 32.5 kN/m) and 84% (32.5 kN/m to 59.7 kN/m), as we altered the rates of compaction from the low to medium traffic condition and from medium to high traffic condition, respectively.

Figure 4.4 D, E and F show the load-deformation plots for the sand sample with 17% moisture content in low, medium and high traffic conditions, respectively. Similar to 12% moisture content, the stiffness coefficient also increases as the density of the sand sample increases. This increase was up to 41% (31.3 kN/m to 44.3 kN/m) and 92% (44.3 kN/m to 85.4 kN/m), as the sand samples were compacted from the low to medium traffic condition and from the medium to high traffic condition, respectively.

Figure 4.4 G, H and I show the load-deformation plots for the sand sample with 20% moisture content in low, medium and high traffic conditions, respectively. As for 12% and 17% moisture levels, the stiffness coefficient was affected with the increase of the density of the sand sample. This was up to 76% (38.8 kN/m to 68.5 kN/m) and 45% (68.5 kN/m to 99.2 kN/m) increase, as the sand samples were compacted from the low to medium traffic condition and from medium to high traffic condition, respectively.

In order to see whether the moisture content affects the stiffness coefficient of the sand sample, we compared the sand samples with different moisture levels but the same density.

Comparing the sand sample with low traffic condition in all three moisture levels, showed an increase in the stiffness coefficient as the moisture level increased. This increase was 87% when the water content was changed from 12% to 17%, and only 24% when it was changed from 17% to 20%.

Comparing the stiffness coefficient of the sand sample in the medium traffic

condition in all moisture levels, revealed that increasing the water content increases the stiffness coefficient. The increase was 26% when the water content was changed from 12% to 17% and 55% when the moisture content increased from 17% to 20%.

Similarly, in the high traffic condition altering the moisture content from 12% to 17% increased the stiffness by 47% and increasing the water content from 17% to 20%, increased the stiffness coefficient by 16%.

In Table 4.2 the stiffness coefficients of the sand sample for all moisture levels and rates of compaction are tabulated. The sand sample with a 12% water content and 1.35 g/cm^3 density had a stiffness coefficient almost equal to a pillow track simulated by McMahon et al. (16.7 kN/m vs 14.4 kN/m) [52]. Added to this, the stiffest calculated surface condition which was the sand sample with 20% moisture content and density of 1.55 g/cm^3, had similar stiffness to a wooden track (99.2 kN/m vs 100 kN/m) [52].

The sand sample with ideal moisture content and rate of compaction

We have discussed previously that the ideal track surface should have enough impact attenuation properties to damp the initial impact shock, as well as providing enough traction for a stable gallop [12, 23, 35]. Ratzlaff et al. investigated in more details and concluded that the surface with ideal mechanical properties has a low amount of energy loss and low impact acceleration (G_{max}) when the foot comes into contact with the surface [47]. The low energy loss, as discussed by Ratzlaff et al. would also increase the performance of the animal in the race.

Chateau et al. discussed that the surface with high performance was associated with a higher risk of injuries. By contrast, the surface with impact attenuation properties tended to increase the muscular effort of the animals (horses in their study) which affected their running performance [50].

The low density of the sand or the rates of compaction are also associated with the low rates of injury [48]. In practice, 'harrowing' was suggested by Kai et al., which can reduce the density or the rates of surface compaction [49]. However, a very low density surface may have a detrimental effect on locomotion efficiency as

it affects the support needed for grip and propelling the body forward [50].

Surface traction is another variable identifying a safe surface composition. High traction will increase the bending moment applied to the bones, mainly the tarsal bones, and increase the risk of injuries [51]. However, not enough traction, usually seen in drier sands, will cause the surface not to sufficiently support the limb during the stance duration and will increase the risk of injury.

Accordingly, Holt et al. suggested that increasing the moisture content of the sand (to provide enough traction), while keeping its density low (to have low maximum acceleration) would result in a surface ideal in both race performance and injury reduction [45].

Contact time is another critical variable that affects the safety performance of the surface. The shorter the contact time, the higher the risk of injuries. Accordingly, this variable is considered as one of the primary safety thresholds in different applications such as playground surfacing tests [5, 4]. In our results, the contact time was not affected by the moisture level of the sand samples, but it significantly decreased with increases of the bulk density of the sample. Thus, low to medium density of the sand sample was found to provide the favourable range of contact time with regards to injury prevention.

Summing up, we saw that altering the moisture content, significantly increased the G_{max} and J_{max} with no substantial change seen in the contact time. Moreover, the rates of compaction significantly increased all the impact data. We also argued that the high G_{max} and J_{max} and short contact time were associated with high injury rate. Accordingly, comparing all the impact data it seems that the sand sample with 20% moisture content in a low traffic condition resulted in the most favourable behaviour with regards to both the injury prevention and race performance. The sand sample in this condition had the lowest energy loss compared to all other cases. The contact time was also in the favourable range as mentioned above. Finally, the G_{max} and J_{max} values are relatively low.

4.4 Summary

In this chapter the effect of two different surface treatments (altering the moisture level and rates of compaction) on the dynamic behaviour of the greyhound track sand sample were considered. In addition, a method to obtain the stiffness coefficient of the sand sample is explained, and the results were plotted and compared. The results showed that, although the moisture content had significantly affected the G_{max} and J_{max} it did not have any considerable effect on the contact time. However, the rates of compaction considerably changed all the impact data and therefore the sand profile dynamic behaviour. Considering all the reported impact data and the required features for a safe gallop, a sand sample with the moisture level of 20% and density of 1.35 g/cm^3 had the most favourable behaviour with regards to injury prevention. Last but not least, the results of this chapter, primarily the method for obtaining the stiffness coefficient of the compliant surfaces, could be used in simulating the body-surface interaction which is presented in Chapter 6.

Chapter 5

A Single IMU to measure greyhound locomotion dynamics

5.1 Introduction

In Chapter 4 the effect of different surface treatments on the functional performance of a sand sample of a typical greyhound race track surface was analysed. It was found that the sand sample with 20% moisture content and 1.35 g/cm^3 density, had the most favourable results in terms of injury prevention.

To study the effect of turning and surface compliance on the galloping dynamics of racing greyhounds, an IMU, equipped with tri-axis accelerometer, was used to measure the associated galloping accelerations. We hypothesised that (i) the greyhound galloping dynamics are different on bends compared to straight sections and (ii) the greyhound galloping dynamics are different on different surface types.

The results showed that galloping on bends had significantly higher anterior-posterior accelerations (generated by hind-legs) than galloping along the straight section. Additionally, the recorded dorsal-ventral acceleration due to hind-leg strikes was more than triple that of the fore-leg strikes (15 G vs 5 G). These results were in consistent with the role of hind-legs in powering the locomotion as well as their higher rates of injuries than fore-legs. Although the impact data (G_{max}) of the sand surface were three times higher than that of the grass track, the IMU data (the average of peaks of dorsal-ventral and anterior-posterior acceleration) for sand versus grass surfaces were not significantly different.

5.2 Methods

The first study aimed to match the IMU signals, i.e. linear acceleration in the anterior-posterior and dorsal-ventral direction with each limb strike. For this pur-

pose, we designed an experiment to survey greyhounds paw prints and run a simultaneous kinematic study to match the signals with the limb strikes. We used a commercial accelerometer, called GPSports/SPI Pro X, designed a race jacket with an embedded pocket located on top of greyhound's wither to accommodate the sensor, and used Sony DSC-RX10-III in 50 frames-per-seconds (fps), facilitating the correlation of the paw prints with their corresponding limb.

The second and third studies investigate more closely the IMU signals to see whether they could identify the different locations on the track and changes in surface compliance. To do so, we used an in-house IMU package, which has a higher sampling rate than the commercial IMU (185 Hz vs 100 Hz), on two tracks, one with a sand surface (hereinafter called Track A) and another one with a natural grass surface (hereinafter Track B).

The fourth study was an impact test to compare the hardness of sand and grass surfaces using a modified Clegg hammer. The Clegg measures the peaks of deceleration when the mass comes into contact with the surface.

However, impact duration is an important safety criterion [4, 5] that the conventional Clegg does not report. Accordingly, we modified the Clegg to get the impact acceleration (in units of gravity (G)) versus time (Contact time (ms)).

5.2.1 Identifying limb strike in IMU signals

A greyhound was encouraged to run in a training session on a typical greyhound race track (Figure 5.1A) with a sandy surface. A commercial tri-axial accelerometer (GPSports/SPI Pro X) capable of measuring accelerations up to 16 G at a sampling frequency of 100 Hz was used (Figure 5.1B). The accelerometer was embedded into a sewn pocket located on top of the greyhound's wither which is approximately above the CoM [102]. The schematic of the experiment is depicted in Figure 5.1C.

A simultaneous kinematics study was done with two Sony DSC-RX10-III cameras, one set to 50 fps to capture the whole race video, another one set to 500 fps to capture at least two full strides of the greyhound with greater resolution. The high frame rate camera was mounted close to the finish line to allow greyhounds to

achieve their highest speed and steady-state gallop.

The trial started from 280 m boxes, followed by the Back Straight to a turn of 52 m radius and then the Home straight. Owing to ethical considerations, only a single dog raced in the trial session. The paw print surveying started immediately after the greyhound was collected by the owner. A theodolite was located outside the track (The coordinate reference is shown in Figure 5.1C).

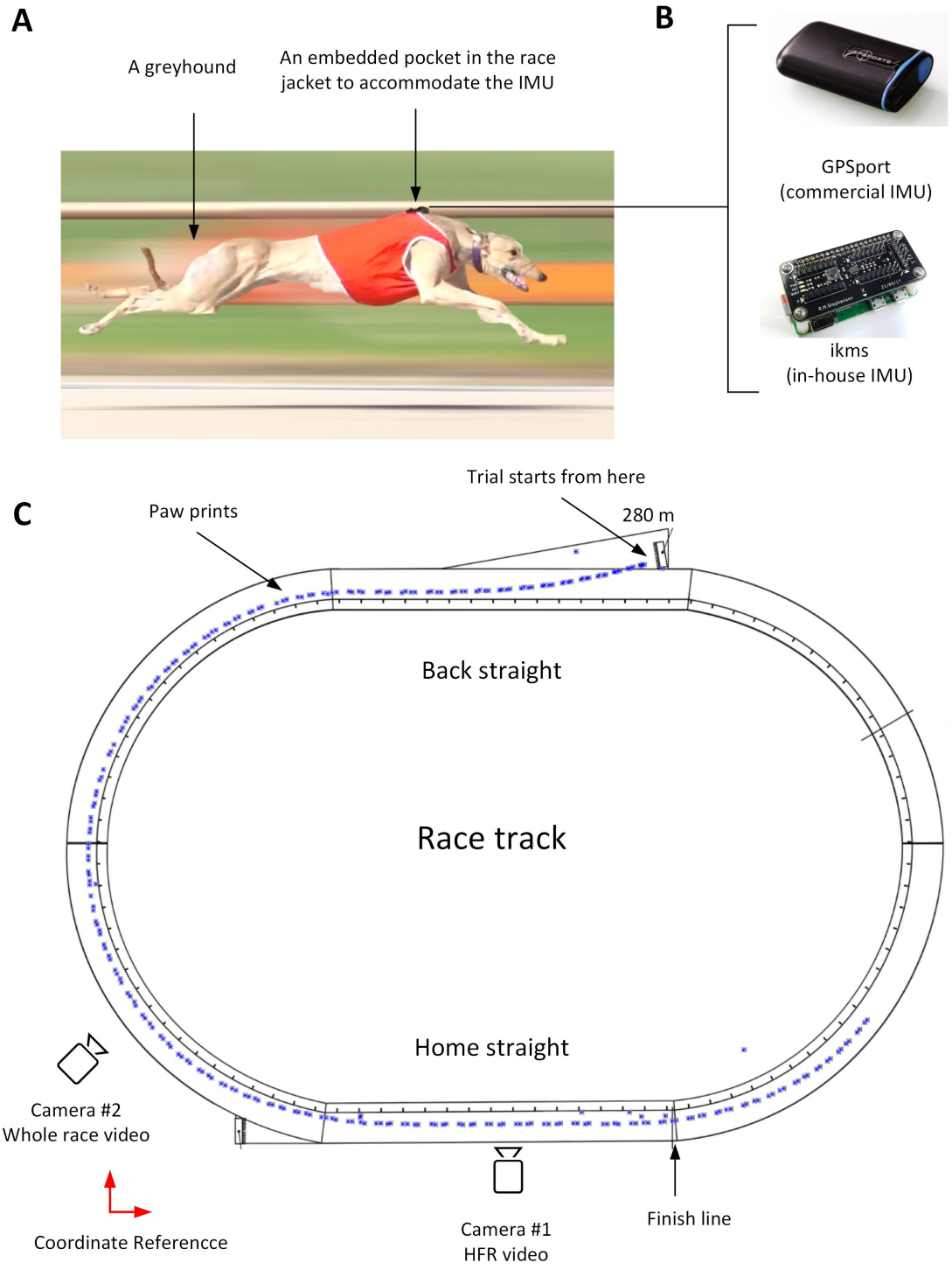

Figure 5.1 : A greyhound galloping on the straight section of a track with sand surface and wearing the designed jacket with embedded sewn pocket (A). The commercial (GPSports/SPI Pro X) and in-house IMU (B). The schematic view of the oval shape sandy track and greyhound's paw prints. The coordinate reference is where the theodolite was mounted to survey the paw prints. Two cameras are mounted for simultaneous kinematic test (C).

5.2.2 How bend and surface compliance affect greyhounds galloping dynamics

Four greyhounds were encouraged to run individually on Track A. Track A is an oval shape sandy track, with the turn radius of 53 m. The track has four race distances, 305 m, 407 m, 480 m and 610 m. Two greyhounds ran from the 407 m distance (starting in Back straight, followed by a bend, Home straight and finish line.) and the rest started from the 480 m distance (starting in bend, followed by Back straight, second bend, Home straight and finish line.).

Four greyhounds ran individually on Track B. Track B is an oval shaped track and has a large radius of 84.1 m with a grass surface. The bends are flat which means the camber angle is almost 0°. The track has two race distances, 300 m and 400 m. Two greyhounds ran from the 300 m distance (starting on a bend, followed by a Home straight and finish line.) and the rest ran from the 400 m distance (starting on Back straight, followed by bend, Home straight and finish line.).

In both Track A and B, an in-house IMU package equipped with a 185 Hz tri-axis accelerometer was used. We compared the anterior-posterior and dorsal-ventral accelerations of six consecutive strides on bend (approximately bend apex) with those of the Home straight, of each greyhound.

In order to see the effect of surface compliance on the dynamics of galloping greyhounds, anterior-posterior and dorsal-ventral acceleration of six consecutive strides of galloping in the Home straight of Track A, were compared with those of Track B.

The temporal galloping gait characteristics using Fast Fourier transform (FFT)

Stride frequency and stride length are two important speed indicator in legged locomotion. The higher the stride frequency and the stride length, the higher the speed [103]. Stride frequency can be measured through optical-based systems (by measuring the footfall timing via videos). However, analysing optical-based data are time-consuming , compute-intensive, and are mostly limited to laboratory environment [62]. Alternatively, accelerometry can be used to measure the stride frequency

by applying Fast Fourier transform (FFT) spectral analysis on acceleration signals.

FFT is a powerful tool in signal processing, which is applied in numerous fields [104]. The FFT is based on the discrete Fourier transforms (DFT) but is much faster than DFT. The DFT is defined as:

$$X(k) = \sum_{n=0}^{N-1} x(n) e^{-j2\pi n/k}, k = 0, 1, ..., N \tag{5.1}$$

where $x(n)$ is a finite data sequence in time-domain consists of N elements and $e^{-j2\pi n/k}$ is a primitive N^{th} root of 1 [105].

All gaits at a steady-state condition (i.e. constant speed) can be considered as a sum of their stationary periodic motion. Deploying FFT spectral analysis would assist in determining the main harmonics of the locomotion, which contains information regarding the fundamental temporal gait characteristics, i.e. the stride and step frequency. Based on Barry et al. study, which aimed to characterise equine gaits via acccelerometry, the first harmonic on the FFT of dorsal-ventral accelerations is the stride frequency of the animal [57]. Accordingly, to compare the stride the FFT was applied on the dorsal-ventral accelerations for all race tracks.

Wavelet analysis

The FFT provides valuable information regarding the temporal gait characteristics, but it is localised only in frequency. This led to the application of wavelet analysis which is localised in both frequency and time. Wavelet analysis is another robust tool in signal processing which decomposes a time-series into time-frequency space. In other words, with wavelet analysis, one can determine both the dominant modes of variability and how those modes vary in time. The continuous wavelet transform (CWT) is a type of wavelet analysis that provides an over-complete representation of a signal by letting the translation and scale parameter of the wavelets vary continuously and is defined as:

$$W_n(s) = \sum_{n'=0}^{N-1} x(n') \sqrt{\frac{\delta t}{S}} \Psi_0^* \left[\frac{(n - n'\delta t}{S} \right] \tag{5.2}$$

where S is the wavelet scale and Ψ is wavelet translation with $*$ symbolise a complex conjunction [106].

Thus, wavelet analysis can be used for gait analysis in biomechanics [58].Using the wavelet analysis, one can detect abrupt changes in signals, which depending on the purpose of the study, contain valuable information. For instance, in work conducted by Biau et al. a wavelet analysis was performed on dorso-ventral axis accelerations in nineteen dressage horses to determine the gait transitions [107]. Moreover, the wavelet spectral analysis was previously used to characterise jumping techniques in equines [58].

Accordingly, the wavelet spectral analysis was performed on anterior-posterior and dorsal-ventral accelerations for Track A and B to determine abrupt changes in the signals during the run, which may indicate hazardous locations on the race tracks.

5.2.3 Surface hardness test using a modified Clegg hammer

In order to compare the hardness of sandy and natural grass surfaces, an impact test was conducted using a modified Clegg hammer, which draws on expertise gained conducting drop tests assessing the safety of children's playgrounds [5, 4]. As given in chapter 4 we modified the Clegg hammer by adding two identical high-G (500 G) piezo-resistive accelerometers (Endevco-7264B-500T). The Clegg and the accelerometers together weighed 2.28 kg. The surface area of the Clegg circular contact surface was 19.63 cm^2 (i.e. 50 mm diameter). LabVIEW software was used to analyse the impact data. The data acquisition unit has a sampling rate of 25000 Hz and complies with AS 4422 standard [108]. A low-pass filter of channel frequency class of 1000 was used.

The impact test was conducted on the Home Straight of both Track A and B. On Track A, which is a sandy track, the test was conducted right after the track preparation and it can be assumed that the track properties were uniform on the Home Straight. The Clegg was dropped four times from different heights of 400 mm and 600 mm, with the maximum impact value reported here [46]. Data were then

post-processed in MATLAB R 2018b.

5.2.4 Animal ethics consideration

Animal ethics approval was obtained (UTS ACEC ETH16-0367). No adverse effects on animal behaviour due to the wearing of the jacket were observed. It is worth noting that the wearing of jackets by greyhounds is routine while they are training or racing. The weight of the IMU device is 66 g, making it three orders of magnitude smaller than the greyhound's body mass of 40 kg.

5.3 Results and discussion

5.3.1 Limb strikes and their corresponding IMU signals

The results of the first experiment are shown in Figure 5.2. Using the whole race video and paw prints, allowed matching the corresponding acceleration data with the leg strikes. In Figure 5.2, the anterior-posterior acceleration versus time for the first three seconds of the test is shown. The first negative peaks correspond to fore-leg impacts with the artificial grass which is used in front of starting boxes to provide enough traction for animals to accelerate. The consecutive positive peaks correspond to the hind-leg impact, which provides the propulsion for locomotion [109]. It should be mentioned that the first two spikes in the signals do not correspond to paw print data as they were on synthetic grass. We compared our results with the Wilson et al. study which used an in-house tracking collar including a GPS and an IMU to capture the locomotor dynamics and outcome of more than three hundred predominantly hunting runs of five wild cheetahs in Botswana [54]. Their results showed that the anterior-posterior acceleration peaks were approximately due to hind-leg foot contact, which is in agreement with our results.

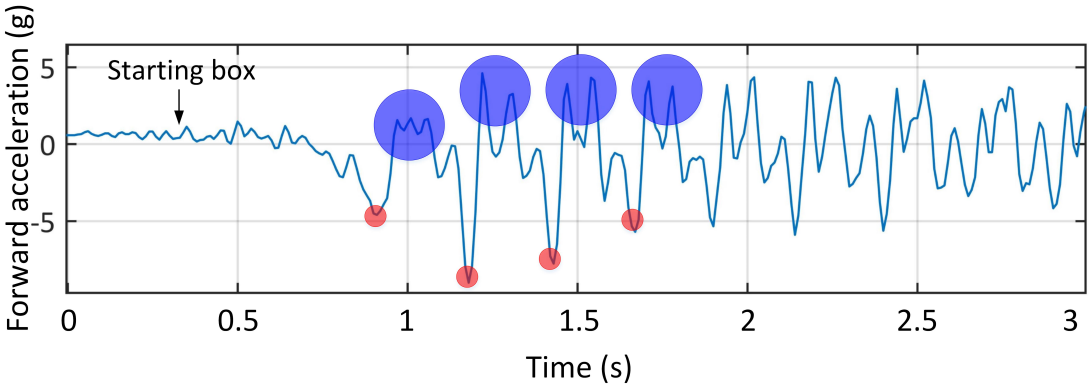

Figure 5.2 : Forward acceleration vs time of eight consecutive strides of a greyhound. The negative peaks (highlighted by red marks) correspond to fore-leg strikes and the positive peaks (highlighted with blue marks) correspond to hind-leg strikes.

Using the HFR data, we generated Table 5.1, where the footfall timing of each of the limbs during the rotary gallop was measured. Rotary gallop is a four-beat gait with two flight phases [13]. The pattern of limb impacts in this gait is rotating i.e. left fore-leg (LF), right fore-leg (RF), compressed flight phase (CFL), right hind-leg (RH), left hind-leg (LH) and extended flight phase (EFL). We then used the

Table 5.1 : Average of stance and flight duration and limb duty factor of galloping greyhounds.

Events	Duration (ms)	β
LF	52.7 $\pm$ 5.1	0.169
RF	58.1 $\pm$ 6.0	0.188
CFL	58.6 $\pm$ 5.3	-
RH	52.5 $\pm$ 4.1	0.169
LH	64.7 $\pm$ 6.6	0.208
EFL	63.5 $\pm$ 9.8	-

footfall timing to match the acceleration signals with the relevant "gait events" of the rotary gallop. The time difference between two consecutive negative peaks is one stride (approximately 300 ms). As mentioned, the negative peaks are due to fore-leg strikes. Adding the LF and RF stance duration leads to the fore-leg lift-off or beginning of the first aerial phase (CFL). The next event is the hind-leg strike.

Adding the RH and LH stance duration leads to the hind-leg lift-off or the beginning of the second aerial phase (EFL). Finally there is another negative peak in anterior-posterior acceleration which is the beginning of the next stride. We continued to use this method for the remaining signals and obtained the same pattern as evidenced in Figure 5.3.

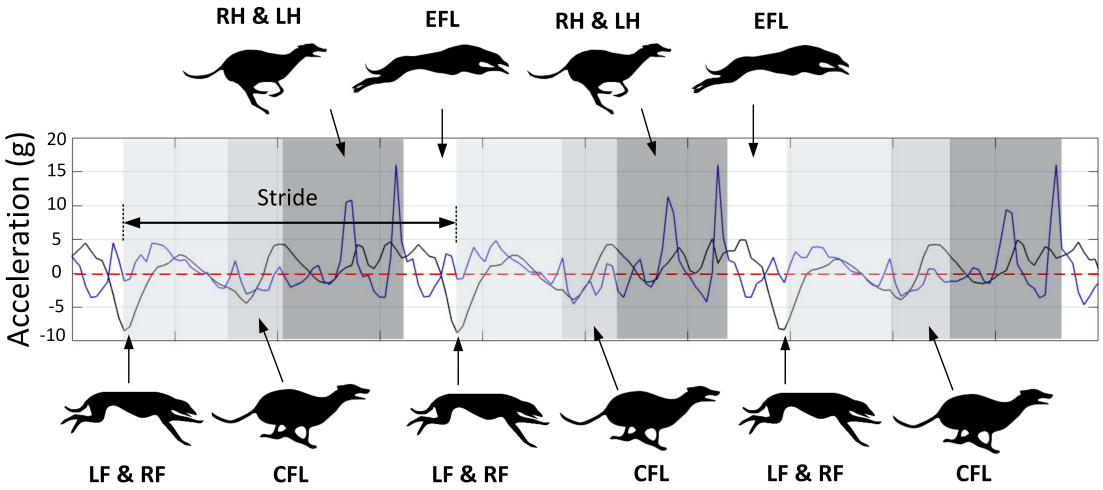

Figure 5.3 : Anterior-posterior (Black line) and dorsal-ventral (blue line) acceleration vs time of three consecutive strides of a greyhound and the corresponding gait events.

Three galloping strides are plotted in Figure 5.3. Greyhound gait events are illustrated, and the arrows are pointed to the corresponding signals.

5.3.2 Effect of bend and different surface composition on greyhound galloping dynamics

The whole race data in both Track A and B was analysed, and it was observed that the negative peaks in anterior-posterior acceleration on bends, which were proven to be due to fore-legs strikes, were lower than those of straight sections as evidenced in Figure 5.4.

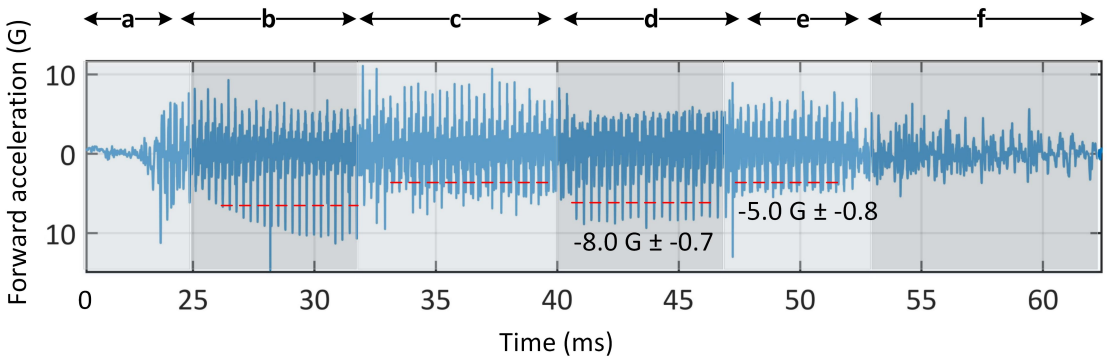

Figure 5.4 : Anterior-posterior acceleration of the whole race in Track A. Accelerating (a), Back straight running (b), the first bend (c), Home straight running (d), the second bend (e) and deceleration (f) are highlighted. The red dashed lines show the average of negative peaks.

Six strides of the bend apex (the bend before the Home straight) were compared with those of the Home straight. The rationale for picking these two sections was allowing greyhounds to have enough time to achieve a steady-state gallop. The t-test (paired two samples for means) was conducted. The values of $P \leq 0.05$ were considered statistically significant. The peaks of signals (anterior-posterior and dorsal-ventral accelerations) in six consecutive strides of the bend apex with that of the Home straight, in both Tracks A and B, for six greyhounds, are tabulated in Table. 5.2 below.

Table 5.2 : Average of peaks for anterior-posterior and dorsal-ventral accelerations on Tracks A and B.

Location on the track	Track A (sand)	Track B (grass)
Anterior-posterior Acc—Fore-leg—Bend	-5.0 ± -0.8G	-5.4 ± -0.2G
Anterior-posterior Acc—Fore-leg—Straight	-8.0 ±-0.7G	-8.7 ± -0.3G
Anterior-posterior Acc—Hind-leg—Bend	6.6 ± 1.3G	6.0 ± 0.7G
Anterior-posterior Acc—hind-leg—Straight	5.4 ± 1.3G	4.7 ± 0.6G
Dorsal-ventral Acc—Fore-leg—Bend	6.2 ± 0.79G	6.4 ± 0.74G
Dorsal-ventral Acc—Fore-leg—Straight	4.4 ± 0.26G	4.7 ± 0.42G
Dorsal-ventral Acc—Hind-leg—Bend	15.0G	15.0G
Dorsal-ventral Acc—Hind-leg—Straight	15.0G	15.0G

Track A: Anterior-posterior acceleration

The anterior-posterior accelerations versus time of greyhounds galloping on Track A are plotted in Figure 5.5 A and B. The negative peaks in anterior-posterior acceleration are associated with the fore-leg strikes, and the positive peaks are due to hind-legs strikes as mentioned earlier.

Comparing the signals resulting from the fore-leg strikes on the bend with those of the Home straight showed a significant difference [t(4)=-8.47 P=0.002].

Additionally, comparing the magnitude of acceleration signals due to fore-leg strikes with those of hind-leg, on both the Home straight and the bend, showed a significant difference [t(4)=3.31 P=0.02 & t(4)=3.2 P=0.02]. These results are consistent with the primary role of the hind-leg in powering the locomotion evidenced in the literature [16, 30, 110]. For instance, Hickman argued that when greyhounds are galloping, the fore-legs are acting like a pivot, while the hind-legs provide the propulsive force [16].

Comparing the anterior-posterior acceleration of the hind-leg strikes on the bend with the Home straight did not show a significant difference [t(4)=0.96 P=0.2].

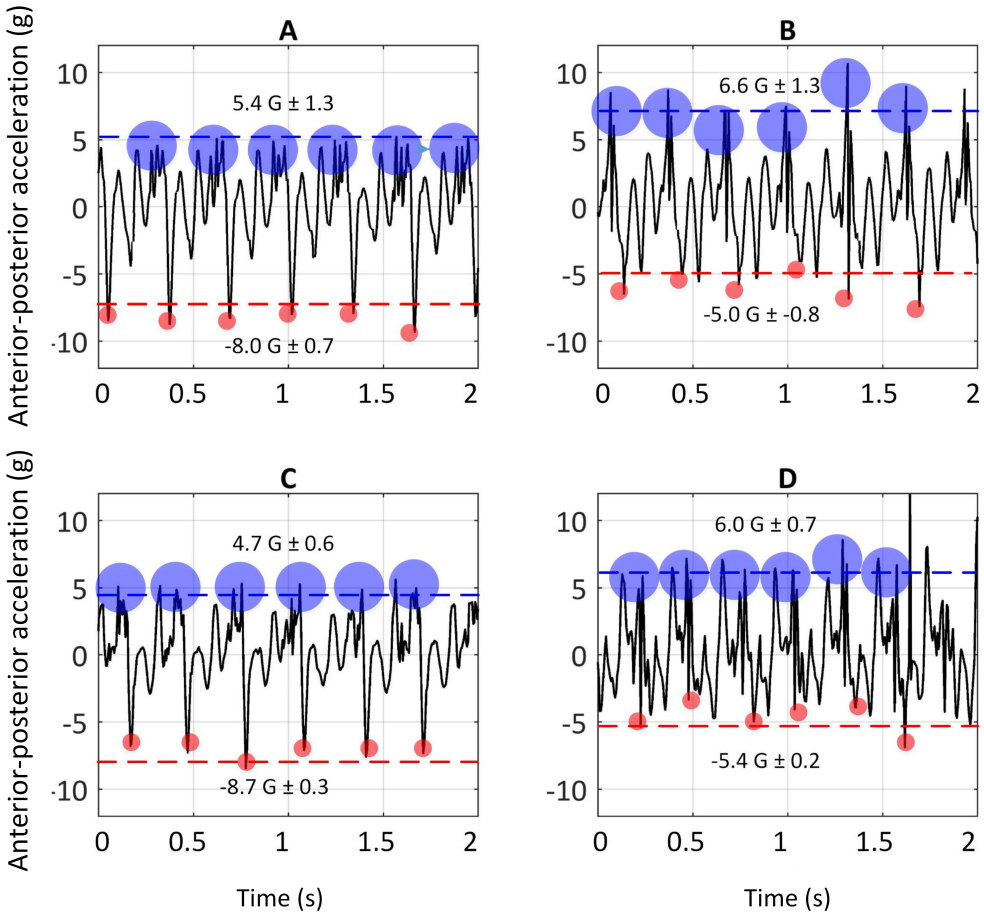

Figure 5.5 : Anterior-posterior acceleration of six consecutive strides on Home straight of Track A (A). Anterior-posterior acceleration of six consecutive strides on the bend of Track A (B). Anterior-posterior acceleration of six consecutive strides on Home straight of Track B (C). Anterior-posterior acceleration of six consecutive strides on the bend of Track B (D). The blue and red circles show the hind-legs and fore-legs strikes, respectively. The dashed red lines show the average of peaks of signals due to fore-leg strikes. The blue dashed lines show the average of peaks of signals due to hind-leg strikes.

Track B: forward acceleration

The anterior-posterior accelerations versus time of greyhounds galloping on Track B are plotted in Figure 5.5. C and D. Comparison of the G-forces of the fore-leg strikes on the bend with the Home straight showed a significant difference [t(4)=-22.7 P=0.00009].

Comparison of the magnitude of acceleration due to fore-leg strikes on the Home straight with those of hind-legs showed a significant difference [t(4)=14.3 P=0.0003].

However, when the IMU signals of hind-leg strikes on the bend were compared with those of fore-legs, no significant difference was observed [t(4)=1.17 P=0.16].

Comparison of the the IMU signals of hind-legs strikes on the bend with the Home straight, showed a significant difference [t(4)=2.31 P=0.05].

Tracks A and B: Dorsal-ventral acceleration

The dorsal-ventral acceleration signals of greyhounds galloping on Tracks A and B are given in this section. As argued earlier, the high positive peaks on dorsal-ventral accelerations were due to hind-leg strikes, and the lower consecutive peaks were due to foreleg strikes, depicted in Figure 5.3. Comparison of accelerations upon hind-leg impacts on the bend and the Home straight showed a similar value of 15 G (1 G due to the animal weight being deducted from 16 G). In other words, forces almost fifteen times of a greyhound's body weight were acting on the limbs in the dorsal-ventral direction each time the hind-legs came into contact with the ground. This well explains the high rate of hind-leg injuries in racing greyhounds [6, 28]. It should be noted that the IMU full-scale range is also 16 G, meaning the device cannot sense signals higher than 16 G. It is possible therefore that, there might be higher acceleration acting on the limbs in reality.

Furthermore, significantly higher values of dorsal-ventral accelerations were seen to be acting on fore-legs when turning than when running along the Home straight on both Track A [t(4)=5.7 P=0.005] and B [t(4)=8,14 P=0.002].

Track A vs Track B: sand surface and grass surface

In order to see whether surface compliance had any effect on the dynamics of greyhounds galloping, the signals for both Track A and B were compared. Firstly, the signals of galloping on the Home straight were compared to eliminate other factors which might affect the results, for example the turning effect.

Anterior-posterior accelerations due to fore-leg strikes on Track A were slightly higher than those of Track B but were not significantly different [t(4)=1.45 P=0.12]. Likewise, when the dorsal-ventral accelerations were compared, the values were not

statistically different [t(4)=2.24 P=0.06]. Similarly, no significant difference between the anterior-posterior acceleration due to hind-leg strikes was seen between the two tracks [t(4)=0.93 P=0.2].

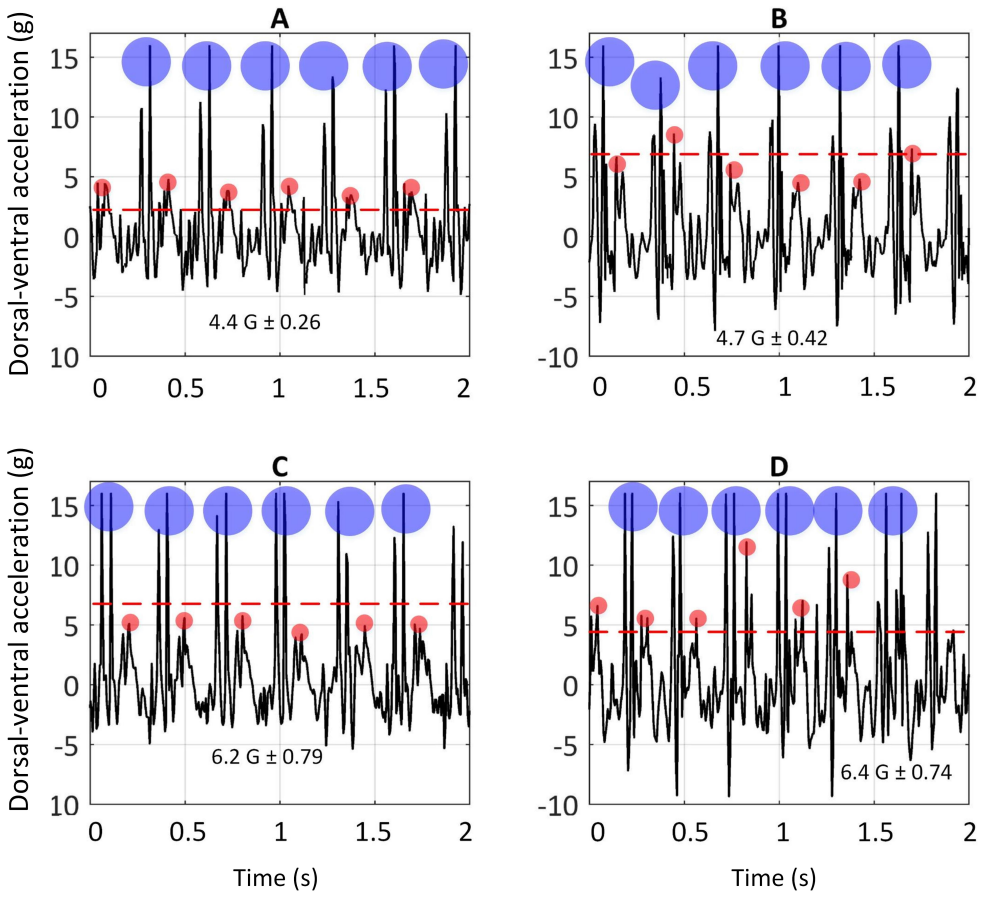

Figure 5.6 : Dorsal-ventral acceleration of six consecutive strides on Home straight of Track A (A). Dorsal-ventral acceleration of six consecutive strides on the bend of Track A (B). Dorsal-ventral acceleration of six consecutive strides on Home straight of Track B (C). Dorsal-ventral acceleration of six consecutive strides on the bend of Track B (D). The blue and red circles show the hind-legs and fore-legs strikes, respectively. The red dashed lines show the average of peaks of signals due to fore-leg strikes.

FFT analysis results

FFT is used to study the temporal characteristics of gaits. The first harmonic in dorsal-ventral acceleration is due to the stride frequency [57]. Figure 5.7 depicts the FFT spectral analysis on dorsal-ventral acceleration for a sample of one dog in Track B.

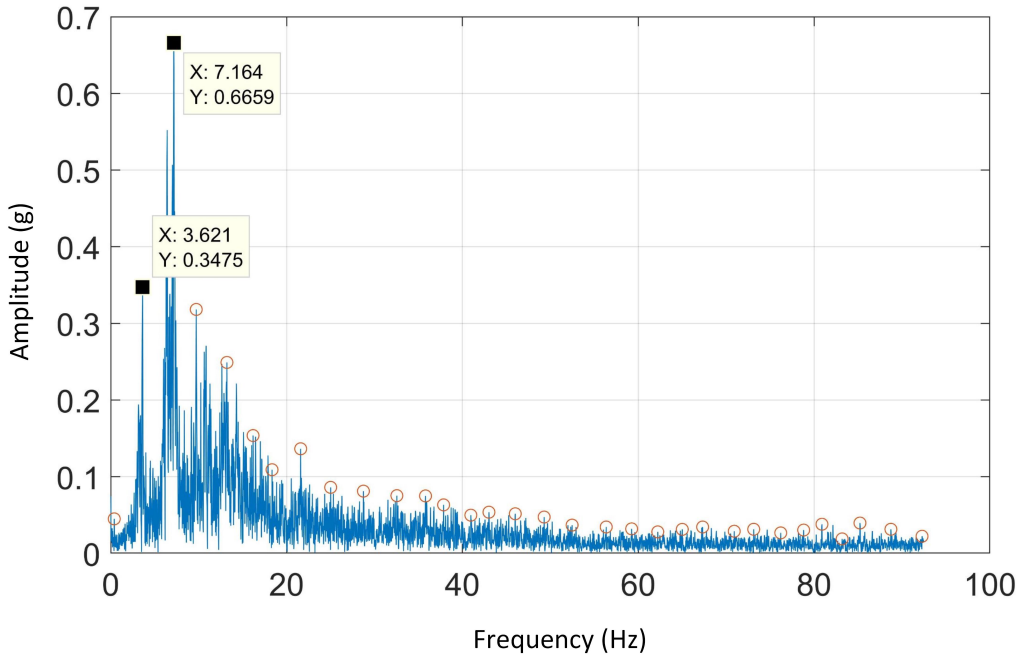

Figure 5.7 : FFT spectral analysis of dorsal-ventral acceleration of Track B.

The average of stride frequencies in Track A and B were around 3.5 Hz. These results were consistent with the measured stride frequencies obtained using HFR videos and literature [111]. The stride frequencies of Track A and B are tabulated in Table 5.3:

Table 5.3 : The average of stride frequencies of greyhounds galloping on Track A and B.

Track	Stride frequency (Hz)
A	3.4 ± 0.15
B	3.5 ± 0.11

The stride frequency and stride length are two important speed indicators in legged locomotion [103]. The results of the FFT analysis on the dorsal-ventral acceleration on Track A and B showed two dominant harmonics. As mentioned, the first one is associated with the stride frequency and the second one might be the step frequency which is also seen in equine gait characteristics [57].

Morlet wavelet spectral analysis

Wavelet spectral analysis is another robust signal-processing tool with various applications in different fields. The main advantages of wavelet analysis over FFT analysis are that wavelets are localised in both time and frequency, whereas the FFT is localised only in frequency. In this section, the results of wavelet analysis on dorsal-ventral and anterior-posterior accelerations for Track A and B are given and compared with the time-domain signals.

Figure 5.8 shows the time-domain and Morlet wavelet power spectrum plots for the dorsal-ventral accelerations of Track A. As can be seen the magnitude and frequency of the signals were decreasing. Also, the animal was walking in the catching pen area before stopping was clear in the wavelet spectrum as the frequency and power of the signals decreased.

Figure 5.9 illustrates the time-domain and Morlet wavelet power spectrum plots for the anterior-posterior accelerations of Track A. As can be seen, there was a sharp increase in both frequency and magnitude when the animal exited the bend section and entered the following straight section.

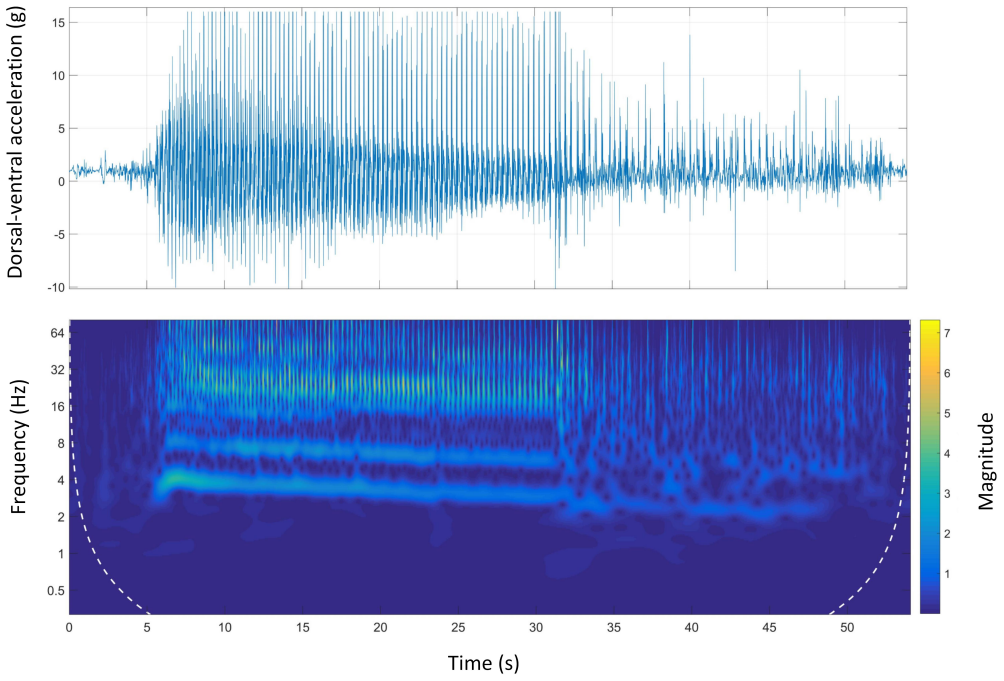

Figure 5.8 : Dorsal-ventral accelerations and Morlet wavelet power spectrum at Track A.

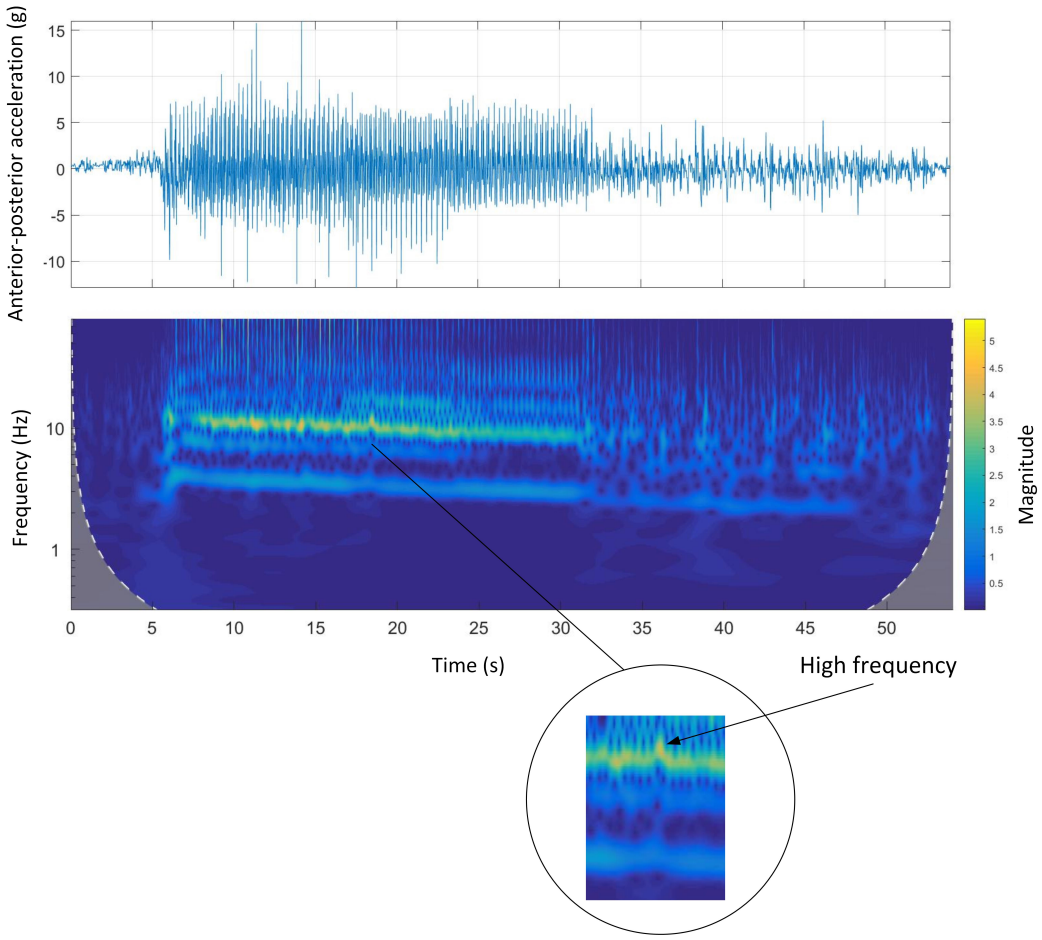

Figure 5.9 : Anterior-posterior accelerations and Morlet wavelet power spectrum at Track A.

Figure 5.10 shows the time-domain and wavelet transform plots for the dorsal-ventral accelerations on Track B. The stride and step frequency of the whole run in the spectrum which is produced by two main temporal periodicities are visible. The stride and the step frequency of the acceleration phase, (the first four seconds of the run), was 4 Hz and 8 Hz, respectively. During the acceleration phase, the stride frequency and magnitude were higher than the rest of the course. The magnitude of the signals was decreasing during the course. The deceleration phase was also clear as the step and stride frequency, as well as the magnitude of the signals sharply decreased at the end of the course.

Figure 5.11 shows the time-domain and wavelet transform plots for the anterior-

posterior accelerations of Track B. A similar pattern to dorsal-ventral accelerations was seen in anterior-posterior accelerations. There was a clear high-frequency high-magnitude signal (10 Hz to 12 Hz) in the wavelet power spectrum. Additionally, comparing the wavelet spectral analysis of Track B with A, the energy expenditure (magnitude) was irregular. This might be due to the inconsistent galloping environment, i.e. track design mainly the track surface as Track B has the natural grass surface.

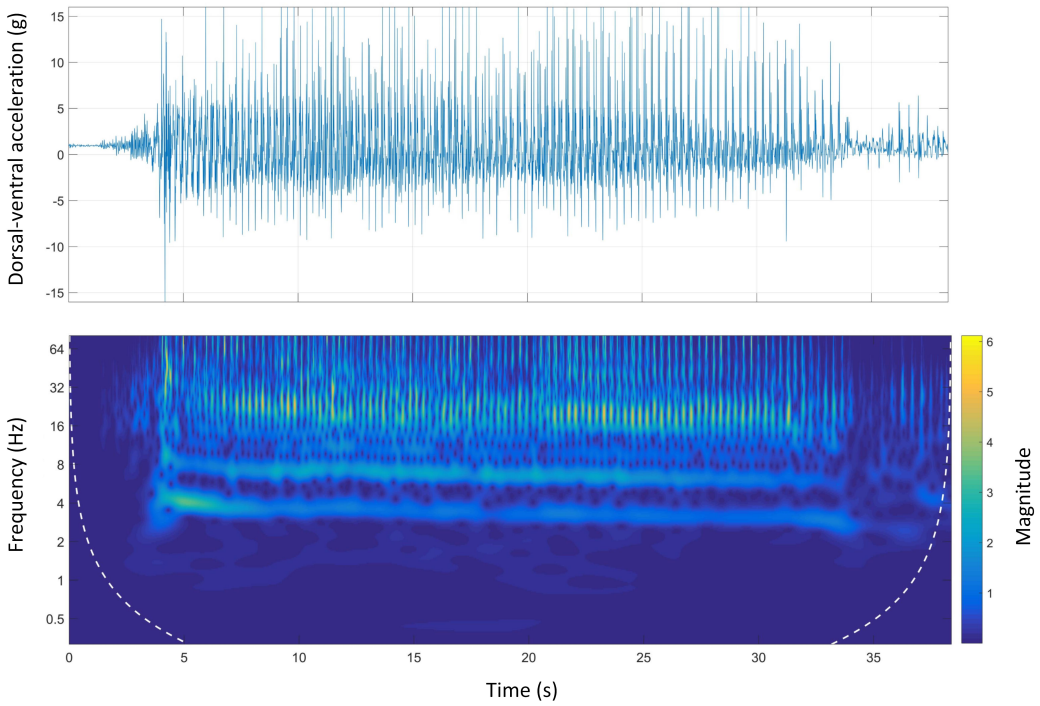

Figure 5.10 : Dorsal-ventral accelerations and Morlet wavelet power spectrum at Track B.

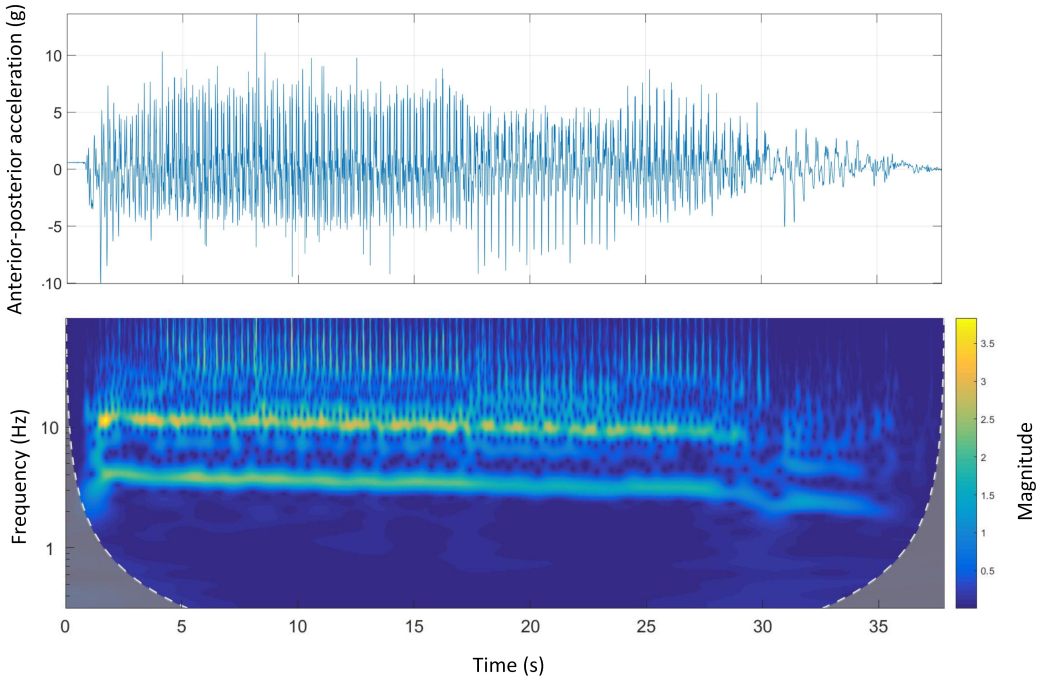

Figure 5.11 : Anterior-posterior accelerations and Morlet wavelet power spectrum at Track B.

The stride and step frequencies and the acceleration and deceleration phases were clear in the wavelet spectrum of the anterior-posterior accelerations in both Track A and B.

The acceleration phase (three to four seconds of the beginning of the race) is associated with high frequency/high magnitude stride frequency. This was in contrast with the deceleration phase, which was related to low frequency/low magnitude stride frequency, happening at the end of the course. The stride and step frequencies of animals were decreasing in all the tracks suggesting animal speed reduction due to fatigue during the course.

Track B showed a very inconsistent stride magnitude during the run compared to Track A (Figure 5.11). This may be because of an inconsistent surface properties as Track B has a grass surface.

There was a clear abrupt change observed in the anterior-posterior accelerations on Track A, when the animal entered the bend section shown in Figure 5.9. The

abrupt changes suggest that the animal either changed the running path to a larger radius to avoid the centrifugal force and jerk on bends or tried to maintain its vision of the mechanical lure while turning. The latter behaviour is one of the reasons for greyhounds clustering while approaching bends [37] and the consequent accidents on bends [3].

5.3.3 Impact test data

The results of the *in-situ* impact test using a modified Clegg hammer are given here. We have explained in Chapter 4 that maximum acceleration and contact time are two essential injury criteria in assessing the safe surface.

Comparing the impact data of Track A, which is a sandy track, with that of Track B which is a grass track showed that G_{max} for the sand surface was almost three times the value of the natural grass surface (170 G vs 55 G for a drop height of 400 mm). Added to this, the impact duration on the sand surface was approximately half that of the natural grass (8 ms vs 16 ms). These results, correlate with a higher rate of hock fractures, which are observed on a sandy track compared to a grass track [19].

Based on the IMU results, it can be concluded that the performance of greyhounds on Track A and B was not significantly different, though the dynamic behaviour of the surfaces was considerably different. This result suggests the need for a more detailed study of the effect of surface mechanical properties on the locomotion dynamics and performance of greyhounds. Added to this, the underneath layers and the inhomogeneity of the both sand and grass surface should be studied before conducting a drop test.

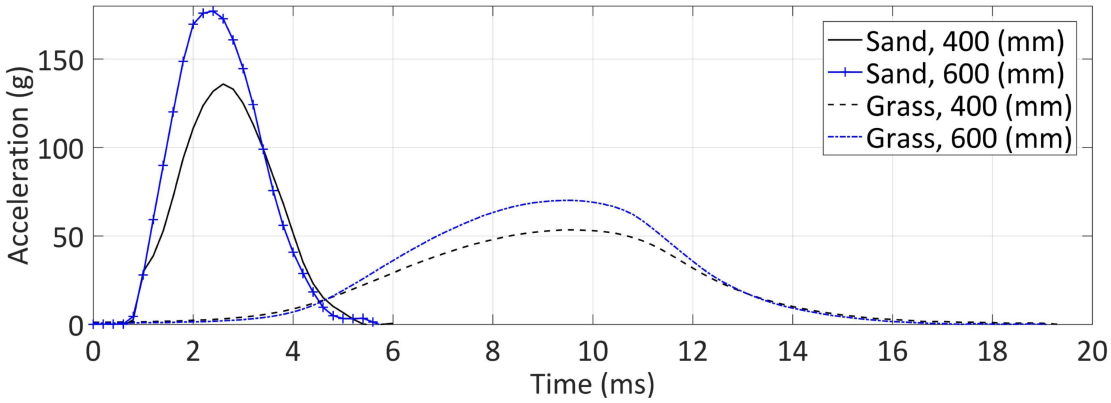

Figure 5.12 : The G_{max} versus time of the sand and grass surfaces with different moisture levels and rates of compaction.

5.4 Summary

The influence of turning and different surface types (sand and grass) on the galloping dynamics of fourteen racing greyhounds were studied. This research is the first, as far as can be ascertained from the literature, to match paw strikes with the anterior-posterior and dorsal-ventral acceleration signals of galloping greyhounds, recorded by a single IMU. The IMU signals were able to identify the difference between turning and straight running. Higher positive peaks in both dorsal-ventral and anterior-posterior accelerations on bends, which were seen to be due to hind-leg strikes, correlated well with the higher rate of hind-leg injuries. Although the sand surface was stiffer than grass, greyhounds galloping dynamics were not significantly different between the grass and sand surface. To summarise, the method developed in this research can make a significant and important contribution to the safety and welfare of agile quadrupeds, such as racing greyhounds and horses, by identifying hazardous track-related elements in racing. Finally, it should also be acknowledged that due to limitations such as available greyhounds and industry restrictions, not all variables were controlled or recorded in this study. Other variables could have affected the results such as age, sex, weight, training and race experience which ideally should be recorded and considered in analysis. A statistical analysis conducted in a recent publication in 2019 [112] showed that age is significantly different between injury types. No evidence was reported that correlate speed and injury, however, these

variables can be considered and will be investigated in future works where possible.

Chapter 6

Greyhound's hind-leg SLIP model during right-hind leg single-support

6.1 Introduction

In Chapter 3 we saw that the hind-legs, mainly the right hock, had the highest injury rate in racing greyhounds. We also mentioned that the bends and the surface types were two important risk factors in this industry. In Chapter 4, we analysed the sand sample of a typical race track to find the ideal surface composition for a safe gallop. Finally, in Chapter 5, we measured greyhounds galloping dynamics with an in-house IMU, and found a significant difference between galloping on bends and straight sections. In this Chapter, we analyse the dynamics of the hind-leg to see if we can find the reasons behind its high injury rate.

The primary purpose of the research reported in this Chapter was to study the impacts of surface compliance on the dynamics of galloping greyhounds during the hind-leg single-support phase as a critical phase in hock injuries. To this end, a 3-DOF model for the greyhound body and substrate surface was designed using the SLIP method. The results showed that forces acting on the CoM did not change by altering the surface compliance, while the loads applied on the hock were substantially affected by it. The main contribution of the work presented in Chapter 6 is designing a mathematical model to predict the dynamics of the hock as the most vulnerable body part in greyhounds. Furthermore, this model can be used to optimise greyhound track surface composition and can therefore contribute to safety and welfare of greyhounds racing industry.

6.2 Methods

Four greyhounds were encouraged to run at Cessnock Track, NSW, Australia, which has a natural grass surface, during a trial session. The greyhounds were released from 'Starting boxes' located at the 400 m race distance and started to chase a mechanical lure driven by a lure driver. The 400 m race started inside the turn, followed by the 'Home straight', then the 'Finish line' and finished at the 'Catching pen' where the greyhounds were collected by the owners.

The simultaneous kinematic analysis to obtain the footfall timing and the hip trajectory during RH-single support is given in Section 6.2.1. The mathematical model of the hind-leg and surface is given in Section 6.2.2.

6.2.1 Kinematic analysis

A Sony DSC-RX10-III camera (adjusted to 500 fps) was mounted on a tripod outside the track and captured greyhounds from a Sagittal view. The camera location was almost at the end of the Home straight to allow enough time for greyhounds to achieve a steady-state gallop. The footfall timing of the greyhounds' rotary gallop in a single stride was firstly calculated, and then their hip joint trajectory during the hind-leg single support was tracked.

Rotary gallop and footfall timing

The rotary gallop is a four-beat gait with two flight phases. Based on our observations most of the greyhounds were 'left-pawed' with an anti-clockwise pattern of paw impacts (Figure 6.1B). As also mentioned in Chapter 5, the pattern of an animal's limb impacts in rotary gallop is rotating i.e. left fore-leg (LF), right fore-leg (RF), compressed flight phase (CFL), right hind-leg (RH), left hind-leg (LH) and extended flight phase (EFL) (Figure 6.1B and C).

The greyhound hind-leg stance phase consists of three different phases: the first single-support phase (which is usually the RH), a double-support phase when both hind-legs are on the ground, and the second single-support phase (which is usually the LH). HFR analysis of greyhounds galloping showed less than 10 ms overlap be-

tween RH and LH in the double-support phase. However, in this work, we only considered the hind-leg 'first' single-support phase and its interaction with the surface. For the sake of simplicity and readability of the dissertation, we refer to this phase as 'RH single-support' hereinafter.

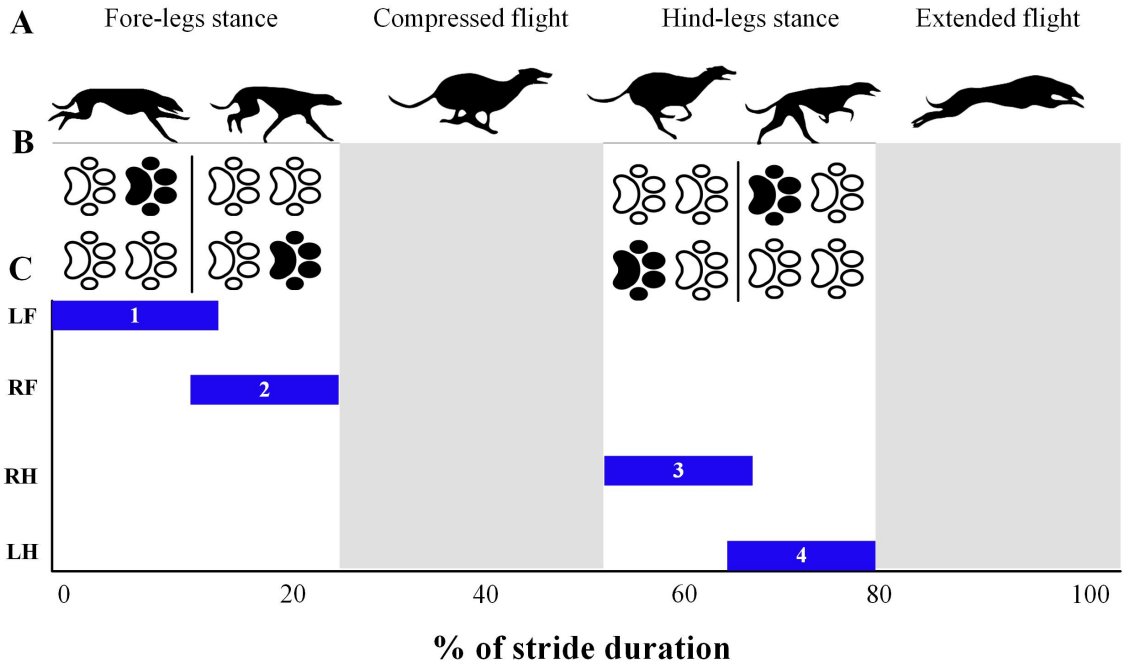

Figure 6.1 : (A) One stride of a galloping greyhound and its corresponding phases. (B) Paw impact pattern of rotatory gallop. (C) Footfall timing of stride duration in percentages; LF, RF, CFL, RH, LH and EFL stands for left fore-leg, right fore-leg, compressed flight, right hind-leg, left hind-leg and extended flight, respectively.

The Hip joint and CoM tracking during RH single-support

HFR videos (set up to 500 fps) of four greyhounds galloping on the Home straight of Cessnock track, were captured. The HFR videos were then post-processed using the Kinovea motion analysis software (version 08.26), which has been reported previously in the literature [113, 114]. A reference pole with a length of 500 mm was attached to the inner rail of the race track to calibrate the videos.

Animal ethics approval was obtained (UTS ACEC ETH160367). This placed several restrictions on the testing including use of sensors and adhesives for attaching 'markers'. No adverse effects on animal behaviour due to filming the greyhounds were observed. Owing to the animal ethics agreement, this required a good deal of manual tracking of greyhound hip joint and CoM (lies 60% along the way from

hip to shoulder joints [102]), during hind-leg single support phase to generate the results provided in this dissertation. We manually adopted the following steps for motion tracking:

- Specified touch down of RH single-support (Figure 6.2A) and set it as the coordinate reference point.
- Drew a reference line from the approximate location of the hip joint and shoulder joint. Estimated the CoM location (60% along the way from hip to shoulder joints [102]) on the reference line (Figure 6.2B).
- Tracked greyhounds' hip joint and CoM during RH single-support using the Kinovea semi-automatic tracking toolbox. Only the hind-leg compression vs time during RH single-support is illustrated (Figure 6.2C).

Figure 6.2 shows the steps adopted. The results of this section were used to validate the simulations explained in the following sections.

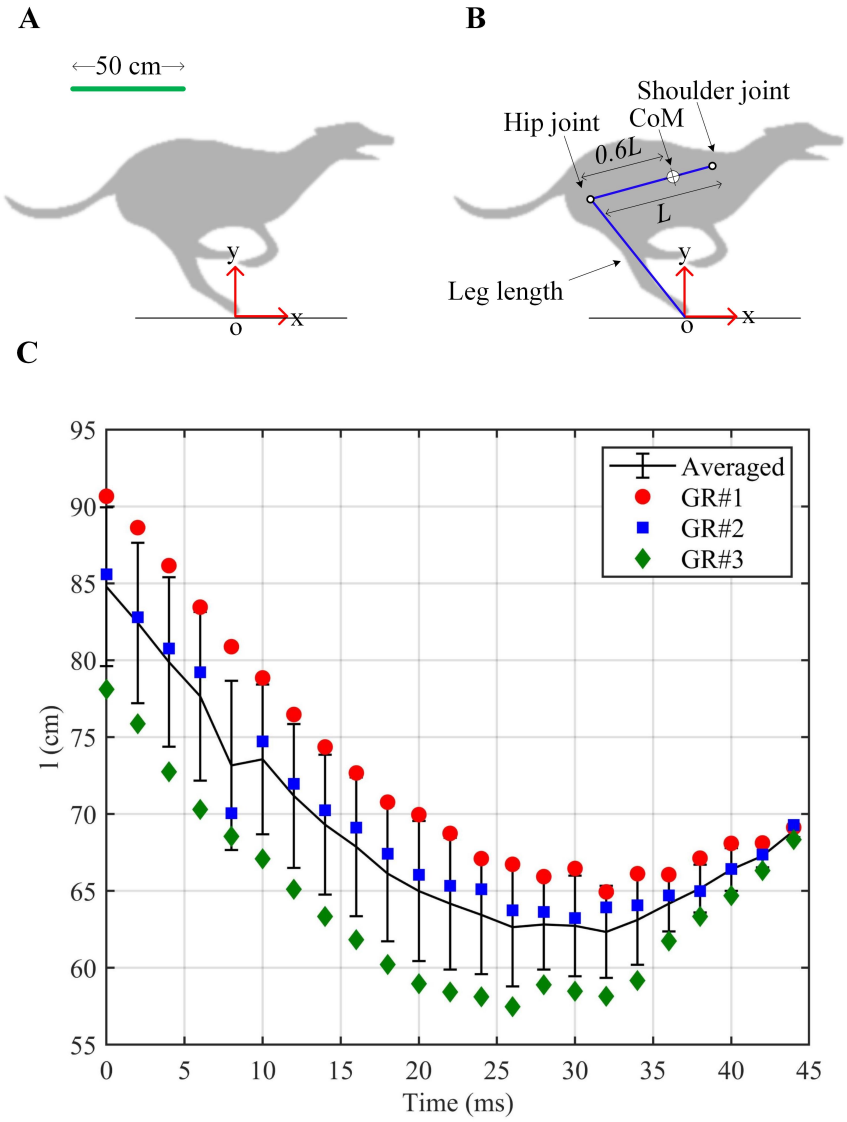

Figure 6.2 : Motion tracking procedure during RH single-support. (A) The coordinate reference point of the system is the touchdown of RH. (B) A reference line from the approximate location of hip joint and shoulder joint is drawn. The CoM location (60% along the way from hip to shoulder joints) on the reference line is estimated. (C) Greyhounds' hip joint and CoM's dynamics during RH single-support using Kinovea semi-automatic tracking toolbox were tracked. Only the hip joint fluctuation versus time for three data sets are presented here.

6.2.2 SLIP model

In order to study the interaction of greyhound RH single-support and the track surface, the SLIP method was used, and was shown to be successful in explaining the dynamics of legged locomotion. In the simplest SLIP model, the overall mass of

the object is usually lumped on the CoM with massless linear springs, representing the legs [70].

Accordingly, in the first attempt, the greyhound and surface were modelled as a 4-DOF system which is shown in Figure 6.3A. The body was modelled as a rigid beam with a mass of m_b. The legs were modelled as linear springs. During RH single-support, hind-legs mass (m_l) was assumed to be concentrated on the toe. Leg compression (l), surface compression (y), leg rotation (θ_1) and body tilting (θ_2) were the independent degrees of freedom of the system. The contact between the hind-legs (the linear spring) and the surface was modeled as a frictionless pin joint.

However, a closer look at the HFR videos of greyhounds during RH single-support phase showed that the ratio of body tilting and leg rotation was negligible or in other words, the body hardly tilted during RH single-support. Thus, we simplified the model which is shown in Figure 6.3B. This approach reduced the order of the model from 4-DOF to a 3-DOF system where the body mass was now lumped on the hip joint. The same simplified model was shown to be accurate enough by Gayer et al. in simulating running and walking gaits [70].

The 3-DOF system consists of hind-leg compression (l), hind-leg rotation (θ), and surface compression (y). Lagrange method [98] was deployed to obtain the system EOM which is given in Equation 6.1 to Equation 6.4.

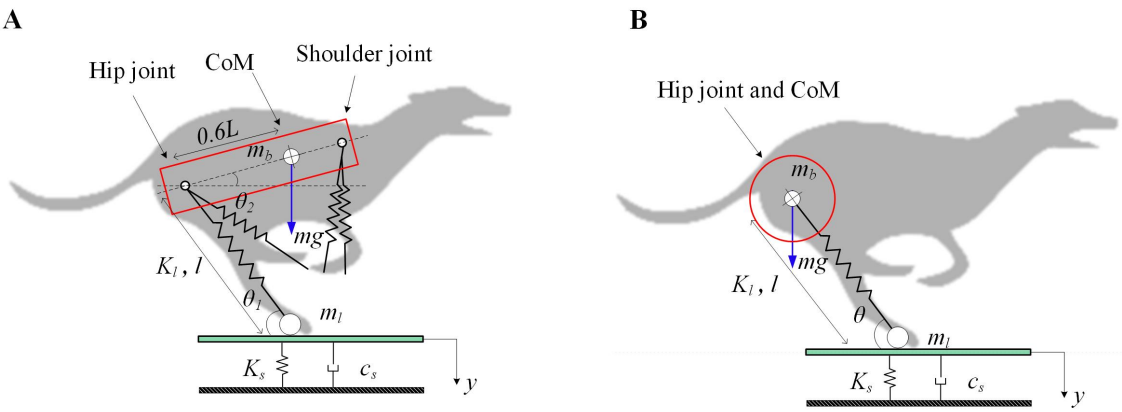

Figure 6.3 : SLIP models of RH single-support of a galloping greyhound. (A) 4-DOF system. (B) 3-DOF system.

$$T = \frac{1}{2}m_b\dot{l}^2 + \frac{1}{2}m_b l^2\dot{\theta}^2 + \frac{1}{2}m_l\dot{y}^2 \tag{6.1}$$

$$U = \frac{1}{2}K_l(l-y)^2 + \frac{1}{2}K_s y^2 + m_b g l sin(\theta) \tag{6.2}$$

$$\mathcal{L} = T - U \tag{6.3}$$

$$\frac{d}{dt}\left(\frac{\sigma\mathcal{L}}{\sigma\dot{q}}\right) - \frac{\sigma\mathcal{L}}{\sigma q} \tag{6.4}$$

where T is the Kinetic energy, U is the Potential energy, and $\mathcal{L}$ is the Lagrangian. The state variables are shown as $q = [l, \theta, y]^T$ and $\dot{q} = [\dot{l}, \dot{\theta}, \dot{y}]^T$. The EOM is given in Equation 6.5 to Equation 6.7.

$$m_b\ddot{l} + K_l(l-y) + c_s\dot{x} - 2m_b l\dot{\theta}^2 - m_b g sin(\theta) = 0 \tag{6.5}$$

$$2m_b l^2\ddot{\theta} + 4m_b l\dot{l}\dot{\theta} + m_b g l cos(\theta) = 0 \tag{6.6}$$

$$m_l\ddot{y} + K_l(y-l) + K_s(y) + c_s\dot{y} = 0 \tag{6.7}$$

where m_b represents the greyhound's overall mass, m_l represents hind-legs mass, k_l represents the hind-legs stiffness coefficient, k_s represents the surface stiffness coefficient, c_s represents the surface damping coefficient, l represents the hind-leg length, $\dot{l}$ represents the hind-leg linear velocity, $\ddot{l}$ represents the hind-leg linear acceleration, y represents surface compression, $\dot{y}$ represents the surface linear velocity, $\ddot{y}$ represents the surface linear acceleration, θ represents the hind-leg angle, $\dot{\theta}$ represents the hind-leg angular velocity, and $\ddot{\theta}$ represents the hind-leg angular acceleration. The Runge Kutta method was deployed to solve the nonlinear second order differential equations using ode45 solver in MATLAB R18 [99, 100].

Surface mechanical properties

As explained in detail in Chapter 4, the stiffness coefficient (k_s) of any compliant surface can be estimated by fitting a line on the 'loading' phase of the load-deformation plots. The surface displacement can be obtained by double integration of the impact acceleration as a function of the impact time[1].

The impact test was conducted via a modified Clegg hammer which is described in detail in Chapter 4. The Clegg hammer was dropped from three different heights of 400 mm, 500 mm and 600 mm on the surface. The test was repeated four times for each height with the maximum value reported here [46].

Figures 6.4A and B represent the load-deformation plots for natural grass and synthetic rubber surfaces respectively, which are superimposed for impact velocities of 2.4 m/s to 3.4 m/s. Refer to Figure 4.4, Section 4.3.2, Chapter 4 for the load-deformation plots of the sand surface. The stiffness coefficients of all the surfaces are tabulated in Table. 6.1.

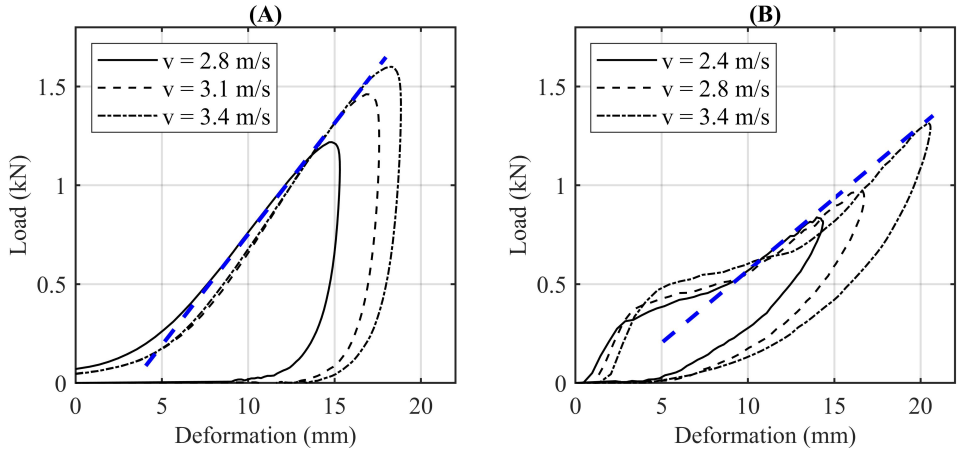

Figure 6.4 : Load-deformation cycles for natural grass for impact velocities of 2.8 to 3.4 m/s (A). Load-deformation cycles for synthetic rubber terrain for impact velocities of 2.4 to 3.4 m/s (B). The slope of the blue dashed line is the effective spring coefficient of the surface (107 kN/m for natural grass surface and 68.2 kN/m for synthetic rubber surface).

Hysteresis was seen in all the plots which revealed the viscoelastic properties in the tested surfaces. Equation 6.8 was considered to get the damping coefficient as

[1]For more information refer to Section 4.3.2 in Chapter 4.

Table 6.1 : Impact data of conducting a drop test on different surfaces. For the sand sample, the second part of the name is the moisture content in percentage. The 'low', 'medium', and 'high' denotes the 'low density', 'medium density', and 'high density' conditions, respectively.

Surface type	k_s (kN/m)
Sand-12%-Low	16.7
Sand-12%-Medium	35.2
Sand-12%-High	57.9
Sand-17%-Low	31.3
Sand-17%-Medium	44.3
Sand-17%-High	84.5
Sand-20%-Low	38.8
Sand-20%-Medium	68.5
Sand-20%-High	99.2
Natural grass	107.0
Synthetic rubber	68.2

given below:

$$F = m_c[\ddot{x}] + c_s[\dot{x}] + k_s[x] \tag{6.8}$$

where F is the force of the Clegg hammer when impacting the ground from different heights, m_c=2.28 kg is the mass of the Clegg hammer and accelerometers, $[\ddot{x}]$ is the vector of acceleration data obtained from the accelerometers, $[\dot{x}]$ is the vector of velocity integrated from the acceleration data, and $[x]$ is the surface penetration obtained from integrating velocity data. The only unknown in Equation 6.8 is the damping coefficient which can be determined by the nonlinear least squares method. Using the MATLAB '*lsqnonlin* function', the damping coefficient was calculated and was equal to 89.6 N.s/m and 81.4 N.s/m for the natural grass and synthetic rubber, respectively. However, it should be noted that the damping coefficient depends on different variables such as temperature, impact velocity, acceleration, shape, and type of stress (compression, tensile, or shear). Thus, the obtained values may alter depending on the loading conditions. All the required inputs for the 3-DOF model are tabulated in the Table 6.2.

Table 6.2 : Model inputs for the 3-DOF SLIP model of greyhounds hind-leg.

Parameters	Determination	Value
m_b	Jayes et al. study [115]	32 kg
m_l	Jayes et al. study [115]	3.4 kg
k_l	Farley et al. study [116]	4.24 kN/m to 4.92 kN/m
k_s	Clegg hammer experiment	Table. 6.1
l_0	HFR videos (measured)	700 mm to 900 mm
$\dot{l_0}$	HFR videos (estimated)	11.3 m/s to 12.5 m/s
θ	HFR videos (estimated)	2.28 rad to 2.39 rad
$\dot{\theta_0}$	HFR videos (estimated)	11 rad/s to 13 rad/s
y	-	0 mm
$\dot{y_0}$	Approximated	11.3 m/s to 12.5 m/s

6.3 Results and discussion

In this section, firstly simulation results are verified with the experimental data (Section 6.3.1). Secondly, the results, namely hind-leg compression vs time, hind-leg rotation vs time, surface compression vs time, CoM trajectories, force applied on the CoM vs time (hereinafter GRF) and force applied on the hind-leg vs time (hereinafter Impact Force) for all the surface types, during RH single-support in all the aforementioned cases are plotted and analysed in Section 6.3.2, Section 6.3.3, and Section 6.3.4.

6.3.1 Simulation verification

To verify the 3-DOF SLIP model, we compared the hind-leg compression (Figure 6.5.A) and rotation (Figure 6.5.B) of four galloping greyhounds during RH single-support on the natural grass surface with the simulation results. We changed the initial conditions in the model as per the experimental data to get the best fit.

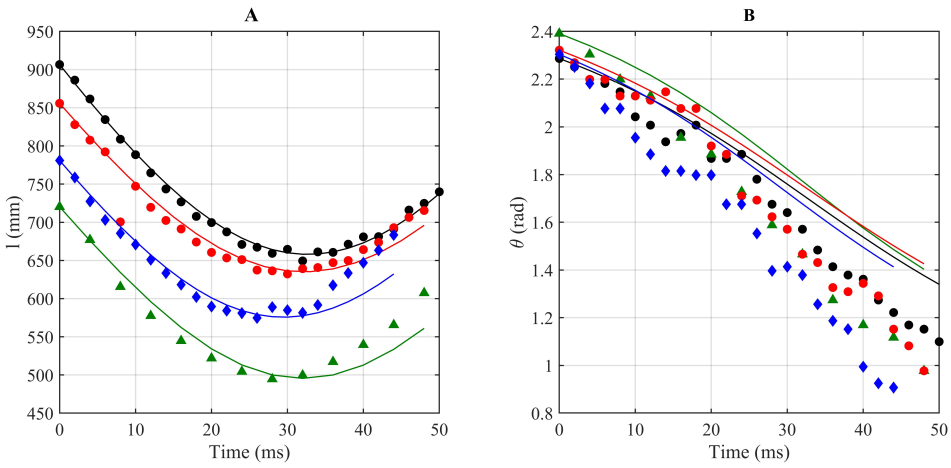

Figure 6.5 : Hind-leg compression vs time (A) and Hind-leg rotation vs time (B) of four greyhounds galloping on the natural grass surface compared with the simulation results. The experimental data and the model results are shown with scattered dots and rigid lines, respectively. The same colours in the scattered plots correspond to the model with similar initial conditions. The root mean square method for the hind-leg compression and leg rotation was equal to 1.59 mm and 0.23 rad, respectively.

The simulation results are shown as rigid lines, and the experimental data are shown as scattered dots. We changed model inputs (l, θ, $\dot{l}$, $\dot{\theta}$) in the 3-DOF model based on the experimental data. Thus, the same colours in the scattered dots correspond to the model with similar initial conditions, e.g. red scattered plot corresponds to red simulated results.

Root Mean Square Error (RMSE) between the model and data was 1.59 mm for hind-leg compression and 0.23 rad for hind-leg rotation vs time. The reported RMSE values here are the average of four conditions. The results show consistency between simulated results and experimental data as the model was able to qualitatively and quantitatively predict greyhound RH single-support dynamics.

6.3.2 RH single-support dynamics over natural grass vs artificial rubber

Dynamics of greyhound RH single-support for natural grass and synthetic rubber surfaces are analysed and compared. The rigid black lines and blue dashed lines illustrate the natural grass and artificial rubber surfaces, respectively. To achieve the highest possible accuracy, we used the initial conditions shown to have the highest corroboration with experimental data.

Hind-leg compression over time during RH single-support is depicted in Figure 6.6A. The motion started from when the extended length of the hind-leg (781 mm), reached its minimum length in the middle of the stance phase (mid-stance from now on) and started extending afterwards. The model predicted the duration of RH single-support with less than 20% error (53.5 ms vs 52.5 ms). It should be noted that the limb does not reach its initial length in this cycle. The consecutive dynamic after RH single-support is the RH double-support, which allows enough time for the leg to extend and finally lift off from the ground. This dynamic was not considered in this study. It can be seen that, the results of natural grass and artificial rubber were similar (the plots are almost superimposed on each other). The results suggested that the current surface compliance did not affect the overall hind-leg compression during RH single-support.

Hind-leg rotation vs time is illustrated in Figure 6.6B. The initial angle of the leg with respect to the ground was 2.269 rad. During mid-stance, the leg was perpendicular with the ground and at the end of the cycle, the hind-leg angle was 1.014 rad. The hind-leg rotations for both surface types were similar.

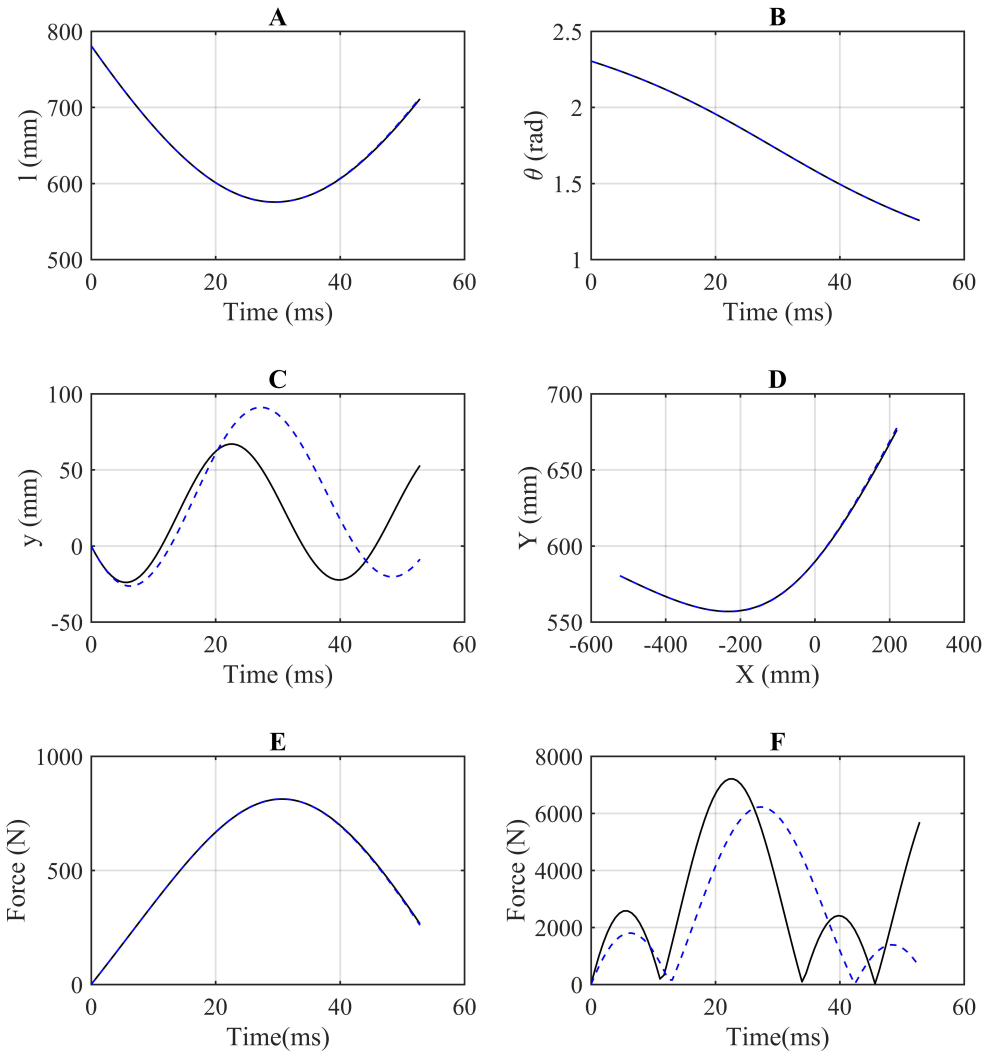

Figure 6.6 : Dynamics of greyhound RH single-support. Hind-leg compression (A), hind-leg rotation (B), surface compression (C), CoM trajectories (D), Force acting on the CoM (E) and Force acting on the hind-leg (F) on two different surface compliances. The rigid black line represents the natural grass surface and the blue dashed line represents the synthetic rubber surface, respectively.

Surface compression over time for natural grass and synthetic rubber surfaces are shown in Figure 6.6.C. The grass surface had lower frequency, but higher amplitude whereas the rubber surface had higher frequency but lower amplitude. At first, both surfaces were compressed to roughly to 25.3 mm. However, they diverged eventually due to their different natural frequency.

CoM trajectories are depicted in Figure 6.6.D. In the model, these data were extracted from the combination of both hind-leg compression and rotation results generated by the model. No difference was seen between trajectories of the CoM on grass and rubber as the results were superimposed.

To calculate the GRF during RH single-support, we used the absolute value of hind-leg compression (l) generated by the model and multiplied that by the spring coefficient of the leg (k_l). The leg spring coefficient was obtained from the Farley et al. study [116]. They measured the leg spring coefficient for animals of different sizes to study the impacts of body size and speed on dimensionless leg stiffness (k_{LEG}). The methods to obtain k_{LEG} were previously determined by McMahon et al. [117]. Farley et al. found that k_{LEG} did not significantly increase with animals forward speed or, in other words, it was independent of the speed. They found the k_{LEG} value of a dog (m=23 kg, l=0.5 m) was between 4.24 to 4.92 kN/m [116]. It should be noted that the reported value k_l is not specific to greyhounds; nevertheless, it was the closest value for this study.

GRF values of galloping over natural grass and synthetic rubber surfaces are illustrated in Figure 6.6E. We compared the results of our model with the Williams et al. study [30]. Their objective was to study the biomechanical strategies enabling greyhounds to achieve an effective acceleration during rotary gallop. To do so, they collected simultaneous kinematic and kinetic data using speed cameras (ProReflex, Qualisys, Gothenburg, Sweden) and force platforms (AMTI, Watertown, MA, USA), respectively. They analysed eleven greyhounds having low acceleration (acceleration ranging from 0.5 m/s^2 to 1.2 m/s^2) and eight greyhounds having high acceleration (acceleration ranging from 2.8 m/s^2 to 4.4 m/s^2). It was found that the greatest increase in joint work and power with acceleration appeared to be at the hip and hock joints. Moreover, the largest increase in absolute positive joint work appeared at the hip joint, supporting the fact that quadrupeds power locomotion by torque about their hip joint [30].

The GRF of the leading hind-leg with low and high acceleration was roughly 1.2 and 1.6 times the average body weight of a greyhound in the Williams et al study

[30]. The GRF predicted by our model is 2.5 times the greyhound's body weight (810 (N)), which seems consistent considering the current limitations. For instance, the sophisticated structure of the hind-leg was modelled with a linear spring and a concentrated mass on the toes, and the rest of the body was designed as a lumped mass on the hip joint. However, considering the aforementioned limitations, our model predicted the GRF within an acceptable range.

The impact force during RH single-support was calculated by multiplying the surface compression (y) by the surface stiffness coefficient (k_s) which is depicted in Figure 6.6.F. According to 'Newton's third law', the same amount of the load but in the opposite direction, acts on the hind-leg from the surface.

6.3.3 Effect of sand density of the track surface on the dynamics of greyhound RH single-support

In Chapter 4 we studied the functional behaviour of a sand sample collected from a typical greyhound race track and analysed the effect of moisture content and rates of compaction on the sand sample impact properties. In this section, the effect of these treatments on the dynamics of greyhound CoM and hind-leg during RH single-support is analysed using the developed model.

The results for the sand sample with 12% moisture content and all three rates of compaction are given in Figure 6.7. The blue, black and red lines denote the low, medium and high-density condition, respectively.

Altering the density of the sand sample with 12% content did not have a significant effect on the dynamics of CoM as the hind-leg compression vs time, the leg rotation vs time, the CoM trajectories and the GRF vs time, were similar between three different rates of compaction as illustrated in Figure 6.7.A, B, D and E.

However, the hock dynamics or in other words the Impact Force acting on the hock increased with increasing density of the sand with 12% moisture content.

The results for the sand sample with 17% moisture content and all three rates of compaction are given in Figure 6.8. The blue, black and red lines denote the low,

medium and high-density condition, respectively.

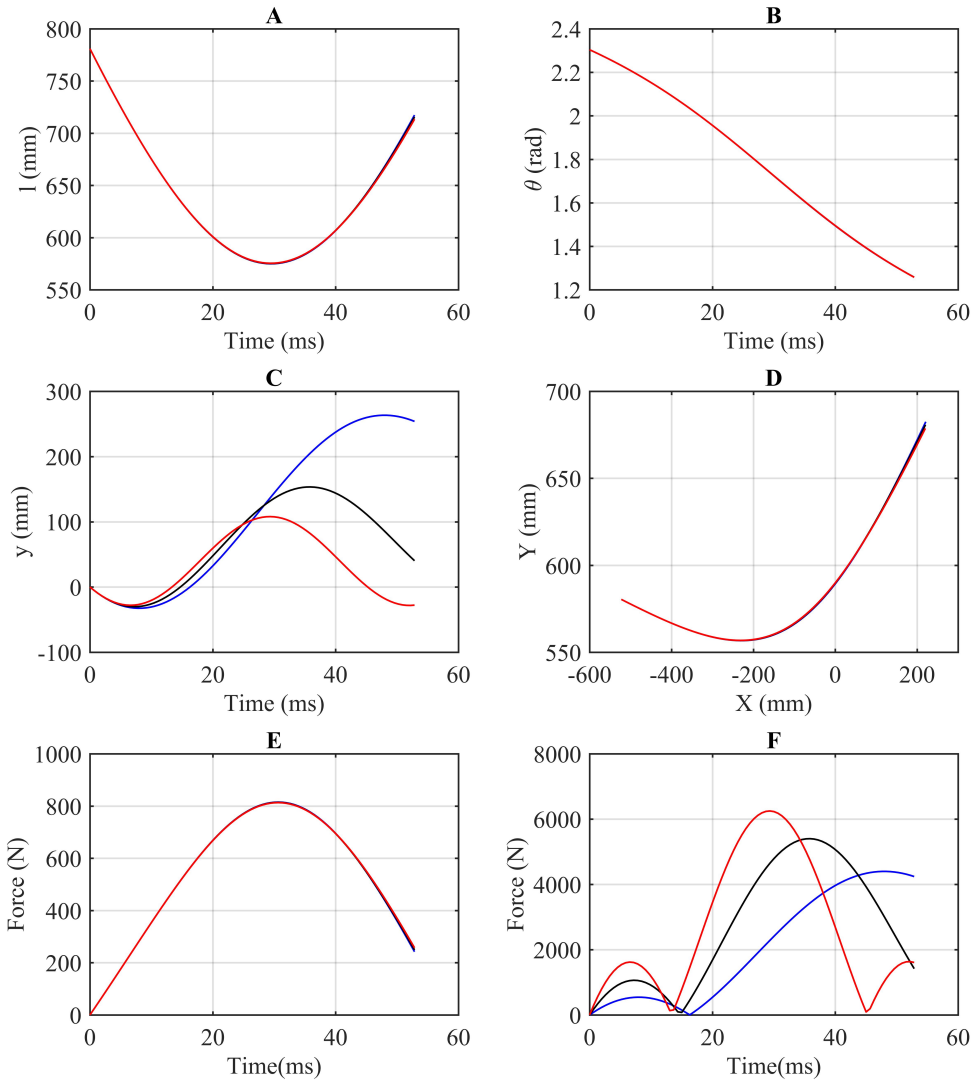

Figure 6.7 : Dynamics of greyhound's RH single-support. Hind-leg compression (A), hind-leg rotation (B), surface compression (C), CoM trajectories (D), Force acting on the CoM (E) and Force acting on the hind-leg (F) on two different surface compliances. The blue, black and red lines denote the low, medium and high-density condition, respectively.

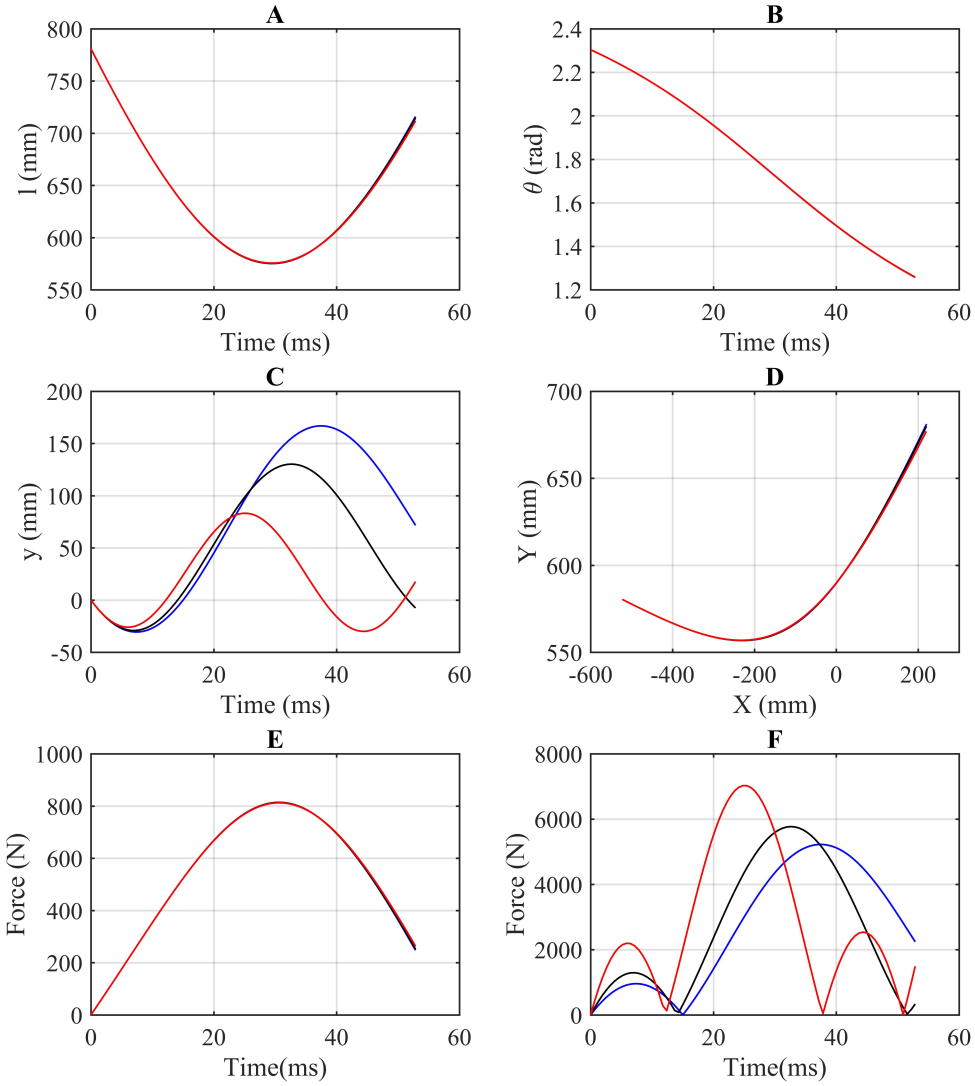

Figure 6.8 : Dynamics of greyhound's RH single-support. Hind-leg compression (A), hind-leg rotation (B), surface compression (C), CoM trajectories (D), Force acting on the CoM (E) and Force acting on the hind-leg (F) on two different surface compliances. The blue, black and red lines denote the low, medium and high-density condition, respectively.

On the one hand, similar to the 12% moisture content sand, the density of the sand sample with 17% moisture content did not have a significant effect on the dynamics of CoM. On the other hand, as the values of the Impact Force increased with the increasing density of the sand sample, it was concluded that the sand rate of compaction had affected the greyhound hock dynamics during RH single-support.

The results for the sand sample with 20% moisture content and all three rates of compaction are given in Figure 6.9. The blue, black and red lines denote the low, medium and high-density condition, respectively.

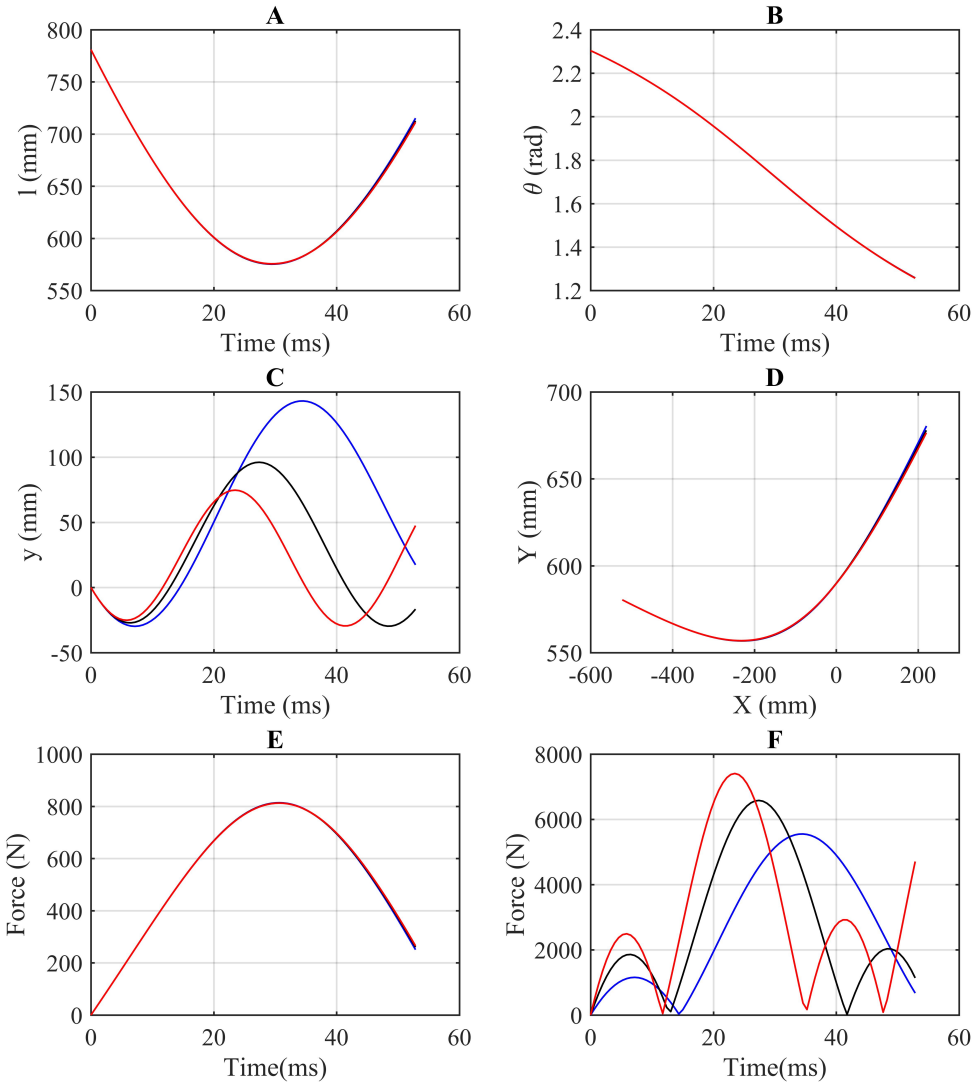

Figure 6.9 : Dynamics of greyhound's RH single-support. Hind-leg compression (A), hind-leg rotation (B), surface compression (C), CoM trajectories (D), Force acting on the CoM (E) and Force acting on the hind-leg (F) on two different surface compliances. The blue, black and red lines denote the low, medium and high-density condition, respectively.

Similar to 12% and 17% moisture content sand, the density of the sand sample with 20% content did not have a significant effect on the dynamics of CoM as the plots for the hind-leg compression vs time, the leg rotation vs time, the CoM

trajectories and the GRF vs time, were almost superimposed in all three rates of compaction. However, the hock dynamics or in other words, the Impact Force acting on the hock increased with increasing density of the sand sample with 20% moisture content.

Accordingly, regardless of the sand moisture content, the density of the sand seemed to affect the dynamics of greyhound hind-leg during RH single-support. Increasing sand density made the sand stiffer, and as discussed earlier, the harder surface had a higher Impact Force than the softer one.

6.3.4 Effect of sand moisture content of the track surface on the dynamics of greyhound RH single-support

The results for the sand sample with medium density in all three levels of moisture content are given in Figure 6.10. The rigid, dashed and dotted black lines show the sample with 20%, 17% and 12% moisture content, respectively. It should be noted that, as the effect of the moisture content on the dynamics of the greyhound's hind-leg was in question, similar sand density was considered for all moisture levels.

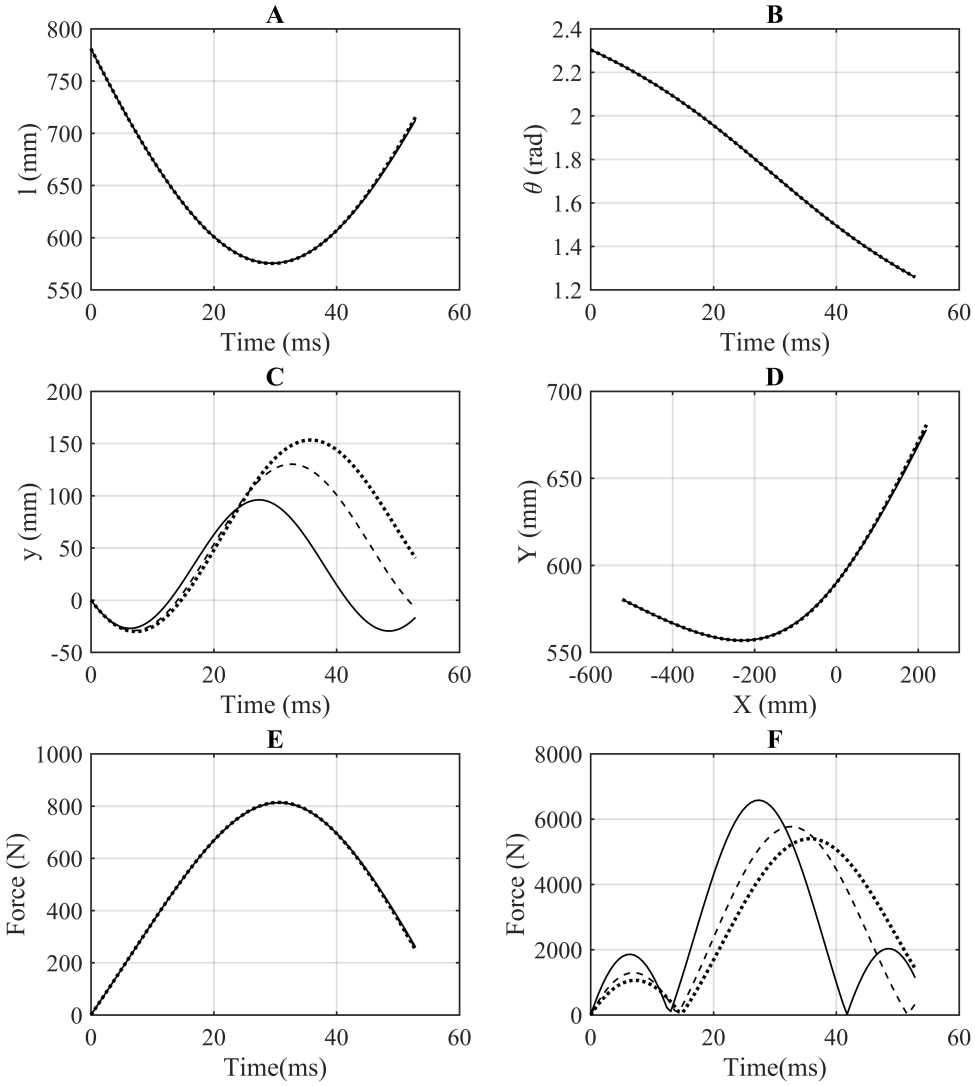

Figure 6.10 : Dynamics of greyhound's RH single-support. Hind-leg compression (A), hind-leg rotation (B), surface compression (C), CoM trajectories (D), Force acting on the CoM (E) and Force acting on the hind-leg (F) on three different surface compliances. The rigid, dashed and dotted lines denote the 12%, 17% and 20% moisutre content, respectively.

It can be seen from Figure 6.10 that increasing the moisture content has increased the Impact Force. However, the GRF values were similar in all moisture levels.

We saw in Chapter 3 that the hock (mainly the right side one) is the leading cause of catastrophic and major injuries in greyhounds. In all the surfaces studied, the second peak of the Impact Force had the highest value. For instance, with the

natural grass surface, the values for the first to the third peaks were 2.6 kN, 7.2 kN, and 2.4 kN, respectively. In the synthetic rubber surface, the values for the first to the third peaks were 1.8 kN, 6.2 kN, and 1.3 kN respectively.

Accordingly, comparing the impact force and GRF in all surface conditions, it can be seen that the Impact Force is almost eight times higher than the GRF, which in other words suggests that the greyhound hock dynamics were significantly affected by the surface compliance. Moreover, the results were qualitatively in agreement with the measured dynamics of galloping greyhounds in Chapter 5 where accelerations upon hind-legs strikes were shown to be fifteen times the greyhound's body weight.

We also discussed in detail in Chapter 2 that inappropriate types and conditions of the track surface could exacerbate the injury rate. It was also evidenced in the literature that hard surfaces increase the chance of hock fracture [26]. These result were in agreement with the current model that harder surfaces increased the Impact Force during RH single-support.

6.4 Summary

The purpose of this work was to study the effect of surface compliance on the locomotion dynamics of racing greyhounds, during the most critical phase of the galloping gait, the RH single-support. To do so, a 3-DOF model of a greyhound body and an underneath surface were designed using the SLIP method. The results showed that surface compliance did not have any significant impacts on the GRF acting on CoM. However, increasing the surface spring coefficient by 36%, resulted in an almost 13% increase in impact force acting on the hind-leg. Added to this, the Impact Force on a relatively hard surface was almost eight times higher than the GRF acting on the CoM. The model also was in agreement with literature injury data, reporting the leading hock injuries as one of the commonest life-threatening injuries in racing greyhounds. To summarise, the simple model was successful in predicting the dynamics of galloping greyhounds as our results were verified by both experimental data and the literature. For future research, the effect of surface compliance

on RH double-support can be conducted to explain the considerable difference in injury data between the leading and trailing hind-leg in racing greyhounds. Finally, this study clearly showed the importance of optimum surface design in reducing catastrophic injuries in greyhounds.

Chapter 7

Conclusion and future works

7.1 Conclusion

In this dissertation, we studied the foot-surface interaction of galloping greyhounds. We firstly analysed the race-related injury data of greyhounds in NSW to determine common types of life-threatening injuries. We then investigated the functional behaviour of the sand, since sand is the typical type of surface material used in greyhound racing. We measured the dynamics of galloping greyhounds on two different types of track surfaces, natural grass and sand, using a single IMU. We finally simulated a greyhound's hind-leg and its interaction with the track surface, using a well-known SLIP model. In this section, we briefly review our achievements, current limitations and future work.

7.2 Contributions

7.2.1 Identifying common types of life-threatening injuries in greyhounds

We analysed injury data collected over a two year period from NSW tracks from January 2016 to December 2017 reported in Chapter 3. It was found that the right hind-leg and mainly the hock has the highest rate of major and catastrophic injuries in racing greyhounds.

7.2.2 Identifying ideal moisture content and rates of compaction of sand surfaces

The functional behaviour of sand, as a typical surface material in greyhound racing, was analysed and presented in Chapter 4. We replicated twelve different conditions of a track surface by altering the moisture content (12%, 17% and 20%) and rates of compaction (1.35 g/cm^3, 1.45 g/cm^3, and 1.55 g/cm^3). We conducted a standard

impact test to assess the safety of replicated surfaces. It was found that a sand sample with 20% moisture content and 1.35 g/cm^3 density was ideal in terms of both injury prevention and galloping performance.

7.2.3 Measuring greyhounds galloping dynamics

We used an in-house and a commercial IMU to measure the galloping dynamics of greyhounds in a simulated race condition on two tracks with different surface types, which is reported in Chapter 5. This research is the first, as far as can be ascertained from the literature, to match greyhounds paw strikes with the acceleration signals of galloping greyhounds, recorded by a single IMU. Thus, we were able to identify the difference between turning dynamics and straight running using the acceleration signals.

7.2.4 Estimating greyhounds hind-leg dynamics via a mathematical model

We developed a 3-DOF SLIP model of a greyhound's hind-leg and an underneath surface presented in Chapter 6. The model could accurately predict greyhounds galloping dynamics during the hind-leg stance phase and could estimate the forces acting on the CoM and the hind-leg on different types of surfaces.

7.3 Future work and limitations

7.3.1 Additional injury types and injury contributing factors

In this dissertation, we analysed two years worth of injury data to find typical types of severe injuries in racing greyhounds. We considered Level 1 and 2[1] injuries of thirty-four greyhound racing tracks in NSW. Analysing the injury data on a track-by-track basis as well as more detailed analysis on injury types can assist in identifying more injury contributing factors. Moreover, we only considered two injury contributing factors in this dissertation. One of the most important risk factors is a smooth transition from straight sections to bends and bends to straights.

[1]Please refer to Section 3.2.1, Chapter 3 for more information on the injury levels.

This is an important topic for future research, which should be taken into account for safety and welfare practices.

7.3.2 Designing a test rig to measure the angular accelerations

To analyse the functional behaviour of greyhound race track surfaces, we collected sample from a typical race track in NSW. We analysed sand samples dynamic behaviour by changing their moisture content and rates of compaction. We did not study the shear strength of sand samples, which should be considered in future. Moreover, we used a standard impact test, which only reports the impact values in vertical direction. In future, a test rig should be designed to measure both the angular and linear impact data.

7.3.3 Higher resolution of kinematic and kinetic analysis

We measured greyhounds galloping dynamics via a single IMU attached above their CoM and could explain the 'fundamental' aspects of their gait. In order to have more accurate kinetic data, multiple sensors should be utilised. The sensors should be attached to greyhounds body segments and should be accurately synchronised with kinematic data of HFR videos.

7.3.4 Higher DOF SLIP models

In order to predict the dynamics of limb-surface interaction in greyhounds, a 3-DOF SLIP model was designed, and the results were verified with the experimental data. In future, a higher order model of greyhounds, which includes the double-support phase to study the significant difference between the leading and trailing hind-leg injury rates, could be useful.

Bibliography

[1] Maurice Cary Powers. A new roundness scale for sedimentary particles. *Journal of Sedimentary Research*, 23(2):117–119, 1953. ISSN 1938-3681.

[2] Markus Tuller, Dani Or, and D Hillel. Retention of water in soil and the soil water characteristic curve. *Encyclopedia of Soils in the Environment*, 4: 278–289, 2004.

[3] Hasti Hayati, David Eager, Robert Stephenson, Terry Brown, and Elizabeth Arnott. The impact of track related parameters on catastrophic injury rate of racing greyhounds. In *9th Australasian Congress on Applied Mechanics (ACAM9)*, page 311. Engineers Australia, 2017.

[4] David Eager and Hasti Hayati. Additional injury prevention criteria for impact attenuation surfacing within children's playgrounds. *ASCE-ASME Journal of Risk and Uncertainty in Engineering Systems, Part B Mechanical Engineering*, 5(1), 2019.

[5] David Eager, Hasti Hayati, and Chris Chapman. Impulse force as an additional safety criterion for improving the injury prevention performance of impact attenuation surfaces in children's playgrounds. In *ASME's International Mechanical Engineering Congress and Exposition (IMECE)*, 2016.

[6] Hasti Hayati, David Eager, Ardian Jusufi, and Terry Brown. A study of rapid tetrapod running and turning dynamics utilizing inertial measurement units in greyhound sprinting. In *ASME 2017 International Design Engineering Technical Conferences and Computers and Information in Engineering Conference*. American Society of Mechanical Engineers, 2017.

[7] Hasti Hayati, Paul Walker, Fatemeh Mahdavi, Robert Stephenson, Terry

Brown, and David Eager. A comparative study of rapid quadrupedal sprinting and turning dynamics on different terrains and conditions: racing greyhounds galloping dynamics. In *ASME 2018 International Mechanical Engineering Congress and Exposition*, pages V04AT06A047–V04AT06A047. American Society of Mechanical Engineers, 2018.

[8] Hasti Hayati, Fatemeh Mahdavi, and David Eager. Analysis of agile canine gait characteristics using accelerometry. *Sensors*, 19(20):4379, 2019.

[9] Hasti Hayati, Paul Walker, Fatemeh Mahdavi, Robert Stephenson, Terry Brown, and David Eager. A simple spring-loaded inverted pendulum (slip) model of a bio-inspired quadrupedal robot over compliant terrains. In *ASME 2018 International Mechanical Engineering Congress and Exposition*, pages V04BT06A052–V04BT06A052. American Society of Mechanical Engineers, 2018.

[10] Hasti Hayati, David Eager, and Paul Walker. The effects of surface compliance on greyhound galloping dynamics. *Proceedings of the Institution of Mechanical Engineers, Part K: Journal of Multi-body Dynamics*, 223(4):1033–1043, 2019. ISSN 1464-4193.

[11] Juliette Cunliffe. *Sight Hounds: Their History, Management and Care*. Swan Hill Press, 2006. ISBN 1904057780.

[12] P.E. Davis. Toe and muscle injuries of the racing greyhound. *New Zealand Veterinary Journal*, 21(7):133–146, 1973. ISSN 0048-0169. doi: 10.1080/00480169.1973.34094. URL `http://dx.doi.org/10.1080/00480169.1973.34094`.

[13] Milton Hildebrand. The adaptive significance of tetrapod gait selection. *American Zoologist*, 20(1):255–267, 1980. ISSN 0003-1569.

[14] Andrew A Biewener. *Animal locomotion*. Oxford University Press, 2003. ISBN 019850022X.

[15] Linda Margaret Beer. *A study of injuries in Victorian racing greyhounds 2006-2011*. Master thesis, The University of Melbourne, 2014.

[16] J Hickman. Greyhound injuries. *Journal of Small Animal Practice*, 16(12): 455–460, 1975. ISSN 1748-5827.

[17] P.E. Davis. Track injuries in racing greyhounds. *Australian veterinary journal*, 43(5):180–191, 1967. ISSN 1751-0813.

[18] J.R. Gannon. Stress fractures in the greyhound. *Australian veterinary journal*, 48(5):244–250, 1972.

[19] JHB Prole. A survey of racing injuries in the greyhound. *Journal of Small Animal Practice*, 17(4):207–218, 1976. ISSN 1748-5827.

[20] Milton Hildebrand. Motions of the running cheetah and horse. *Journal of Mammalogy*, 40(4):481–495, 1959. ISSN 0022-2372.

[21] A Cook. Literature survey of racing greyhound injuries, performance and track conditions. *Journal of Turfgrass Science*, 74:108–113, 1998. ISSN 1367-8361.

[22] Mark S Bloomberg, Jon F Dee, and Robert Augustus Taylor. *Canine sports medicine and surgery*. Saunders, 1998. ISBN 0721650228.

[23] L.R Gillette. Track surface influences on the racing greyhound. *Greyhound review*, 20:41–44, 1992.

[24] MS Bloomberg and WW Dugger. Racing injuries of greyhounds: racetrack injury survey. In *Proceedings of the 12th Annual International Sports Medicine Symposium*, pages 28–35, 1996.

[25] Bede W Ireland. *Race track biomechanics and design*, chapter 47, pages 393–396. Saunders, 1998.

[26] MS Bloomberg. Racing greyhound track injuries. In *Annual International Racing Greyhound Symposium Florida*, pages 3–12, 1989.

[27] GK Sicard, K Short, and PA Manley. A survey of injuries at five greyhound racing tracks. *Journal of small animal practice*, 40(9):428–432, 1999. ISSN 1748-5827.

[28] JM Jones. *Repair of hock fractures in racing greyhounds*. British Medical Journal Publishing Group, 2009. ISBN 0042-4900.

[29] D Eager, A Pendrill, and N Reistad. Beyond velocity and acceleration: jerk, snap and higher derivatives. *European Journal of Physics*, 37(6):65–68, 2016. ISSN 0143-0807.

[30] S. B. Williams, J. R. Usherwood, K. Jespers, A. J. Channon, and A. M Wilson. Exploring the mechanical basis for acceleration: pelvic limb locomotor function during accelerations in racing greyhounds (canis familiaris). *The Journal of Experimental Biology*, 212(4):550–565, 2009.

[31] Peter R Greene. Running on flat turns: experiments, theory, and applications. *Journal of biomechanical engineering*, 107(2):96–103, 1985. ISSN 0148-0731.

[32] Peter R Greene. Sprinting with banked turns. *Journal of biomechanics*, 20 (7):667–680, 1987. ISSN 0021-9290.

[33] J. Iddon. The effect of season and track condition on injury rate in racing greyhounds. *Journal of Small Animal Practice*, 55(8):399–404, 2014.

[34] T.C Angle, R. L Gillette, and W. H Weimar. Caudal paw displacement during movement initiation and its implications for possible injury mechanisms. *Veterinary and Comparative Orthopaedics and Traumatology*, 25(5):397–401, 2012.

[35] L.R Gillette. Optimizing performance and prevent injuries of the canine sprint athlete. In *North American Veterinary Conference 2007*, pages 1–6, 2007.

[36] Robert OW Walpole. Some preliminary observations and remarks on limb lameness in the racing track greyhound. *The Veterinary Journal (1900)*, 100 (1):11–16, 1944.

[37] Fatemeh Mahdavi, Md Imam Hossain, Hasti Hayati, David Eager, and Paul Kennedy. Track shape, resulting dynamics and injury rates of greyhounds. In *ASME 2018 International Mechanical Engineering Congress and Exposition*, pages V013T05A018–V013T05A018. American Society of Mechanical Engineers, 2018.

[38] Adam M Neville. *Properties of concrete*. Pitman, 1973. ISBN 0273361538.

[39] Adam M Neville and Jeffrey John Brooks. *Concrete technology*. Longman Scientific & Technical England, 1987. ISBN 0582988594.

[40] Australian Standard. As 1289 method 2.1.1: Methods of testing soils for engineering purposes, 2014.

[41] JJ Setterbo, PB Fyhrie, M Hubbard, SK Upadhyaya, and Susan M Stover. Dynamic properties of a dirt and a synthetic equine racetrack surface measured by a track-testing device. *Equine Veterinary Journal*, 45:25–30, 2013.

[42] B Clegg. An impact testing device for in situ base course evaluation. In *Australian Road Research Board Conference Proc*, volume 8, 1976.

[43] Abbas Mohajerani, Halenur Kurmus, Linda Tran, Chethana Maha Arachchillegedar, Mehdi Mirzababaei, and Arul Arulrajah. Clegg impact hammer: an equipment for evaluation of the strength characteristics of pavement materials, turf, and natural and artificial playing surfaces: a review. *Journal of Road Materials Pavement Design*, pages 1–19, 2018. ISSN 1468-0629.

[44] ML Peterson, C Wayne McIlwraith, and Raoul F Reiser II. Development of a system for the in-situ characterisation of thoroughbred horse racing track surfaces. *Biosystems Engineering*, 101(2):260–269, 2008. ISSN 1537-5110.

[45] Danielle Holt, Alison Northrop, Andy Owen, Jaime Martin, and Sarah Jane Hobbs. Use of surface testing devices to identify potential risk factors for synthetic equestrian surfaces. *Procedia Engineering*, 72:949–954, 2014. ISSN 1877-7058.

[46] ASTM. Standard test method for determination of the impact value (iv) of a soil, 2007.

[47] Marc H Ratzlaff, Martha L Hyde, David V Hutton, Rhonda A Rathgeber, and Olin K Balch. Interrelationships between moisture content of the track, dynamic properties of the track and the locomotor forces exerted by galloping horses. *Journal of Equine Veterinary Science*, 17(1):35–42, 1997. ISSN 0737-0806.

[48] Eric L Radin, Micheal G Ehrlich, Robert Chernack, Peter Abernethy, IGOR L Paul, and Robert M Rose. Effect of repetitive impulsive loading on the knee joints of rabbits. *Clinical Orthopaedics and Related Research*, (131):288–293, 1978.

[49] M Kai, T Takahashi, O Aoki, and H Oki. Influence of rough track surfaces on components of vertical forces in cantering thoroughbred horses. *Equine Veterinary Journal*, 31(S30):214–217, 1999.

[50] H Chateau, L Holden, D Robin, S Falala, P Pourcelot, P Estoup, J-M Denoix, and N Crevier-Denoix. Biomechanical analysis of hoof landing and stride parameters in harness trotter horses running on different tracks of a sand beach (from wet to dry) and on an asphalt road. *Equine Veterinary Journal*, 42:488–495, 2010. ISSN 0425-1644.

[51] Rachel C Murray, Walters Juli M., Snart Hannah, Dyson Sue J., and Parkin Tim DH. Identification of risk factors for lameness in dressage horses. *The Veterinary Journal*, 184(1):27–36, 2010.

[52] Thomas A McMahon and Peter R Greene. The influence of track compliance on running. *Journal of biomechanics*, 12(12):893–904, 1979. ISSN 0021-9290.

[53] Amy E Kerdok, Andrew A Biewener, Thomas A McMahon, Peter G Weyand, and Hugh M Herr. Energetics and mechanics of human running on surfaces of different stiffnesses. *Journal of Applied Physiology*, 92(2):469–478, 2002. ISSN 8750-7587.

[54] Alan M Wilson, JC Lowe, K Roskilly, Penny E Hudson, KA Golabek, and JW McNutt. Locomotion dynamics of hunting in wild cheetahs. *Nature*, 498 (7453):185–189, 2013. ISSN 0028-0836.

[55] Greg Byrnes, Norman T-L Lim, and Andrew J Spence. Take-off and landing kinetics of a free-ranging gliding mammal, the malayan colugo (galeopterus variegatus). *Proceedings of the Royal Society of London B: Biological Sciences*, 275(1638):1007–1013, 2008. ISSN 0962-8452.

[56] Andrew J Spence, Shai Revzen, Justin Seipel, Chris Mullens, and Robert J Full. Insects running on elastic surfaces. *Journal of Experimental Biology*, 213 (11):1907–1920, 2010. ISSN 0022-0949.

[57] E Barrey, M Hermelin, JL Vaudelin, D Poirel, and JP Valette. Utilisation of an accelerometric device in equine gait analysis. *Equine Veterinary Journal*, 26(S17):7–12, 1994. ISSN 0425-1644.

[58] E Barrey and P Galloux. Analysis of the equine jumping technique by accelerometry. *Equine Veterinary Journal*, 29(S23):45–49, 1997. ISSN 0425-1644.

[59] TH Witte, K Knill, and AM Wilson. Determination of peak vertical ground reaction force from duty factor in the horse (equus caballus). *Journal of Experimental Biology*, 207(21):3639–3648, 2004. ISSN 0022-0949.

[60] T. Pfau, T. H. Witte, and A. M. Wilson. Centre of mass movement and mechanical energy fluctuation during gallop locomotion in the thoroughbred racehorse. *Journal of Experimental Biology*, 209(Pt 19):3742–57, 2006. ISSN 0022-0949 (Print) 0022-0949 (Linking). doi: 10.1242/jeb.02439. URL `https://www.ncbi.nlm.nih.gov/pubmed/16985191`. Pfau, Thilo Witte, Thomas H Wilson, Alan M eng Comparative Study Research Support, Non-U.S. Gov't England J Exp Biol. 2006 Oct;209(Pt 19):3742-57. doi: 10.1242/jeb.02439.

[61] Gregory J. Jenkins, Chady H. Hakim, N. Nora Yang, Gang Yao, and Dongsheng Duan. Automatic characterization of stride parameters in canines with

a single wearable inertial sensor. *PLOS ONE*, 13(6):e0198893, 2018. doi: 10.1371/journal.pone.0198893. URL https://doi.org/10.1371/journal.pone.0198893.

[62] M. Rhodin, A. Bergh, P. Gustås, and C. B. Gómez Álvarez. Inertial sensor-based system for lameness detection in trotting dogs with induced lameness. *The Veterinary Journal*, 222:54–59, 2017. ISSN 1090-0233. doi: https://doi.org/10.1016/j.tvjl.2017.02.004. URL http://www.sciencedirect.com/science/article/pii/S109002331730045X.

[63] CB Gómez Alvarez, P Gustås, A Bergh, and M Rhodin. Vertical head and pelvic movement symmetry at the trot in dogs with induced supporting limb lameness. *The Veterinary Journal*, 229:13–18, 2017.

[64] Cassim Ladha, Jack O'Sullivan, Zoe Belshaw, and Lucy Asher. Gaitkeeper: A system for measuring canine gait. *Sensors*, 17(2):309, 2017. ISSN 1424-8220. URL https://www.mdpi.com/1424-8220/17/2/309.

[65] Linda Gerencsér, Gábor Vásárhelyi, Máté Nagy, Tamas Vicsek, and Adam Miklósi. Identification of behaviour in freely moving dogs (canis familiaris) using inertial sensors. *PLOS ONE*, 8(10):e77814, 2013. doi: 10.1371/journal.pone.0077814. URL https://doi.org/10.1371/journal.pone.0077814.

[66] Winard R. Britt, Jeffrey Miller, Paul Waggoner, David M. Bevly, and John A. Hamilton. An embedded system for real-time navigation and remote command of a trained canine. *Personal and Ubiquitous Computing*, 15(1):61–74, 2011. ISSN 1617-4917. doi: 10.1007/s00779-010-0298-4. URL https://doi.org/10.1007/s00779-010-0298-4.

[67] Alvaro Muro-De-La-Herran, Begonya Garcia-Zapirain, and Amaia Mendez-Zorrilla. Gait analysis methods: An overview of wearable and non-wearable systems, highlighting clinical applications. *Sensors*, 14(2):3362–3394, 2014.

[68] Nuno Ferrete Ribeiro and Cristina P Santos. Inertial measurement units: A

brief state of the art on gait analysis. In *IEEE 5th Portuguese Meeting on Bioengineering (ENBENG)*, pages 1–4, 2017.

[69] Shigeru Tadano, Ryo Takeda, and Hiroaki Miyagawa. Three dimensional gait analysis using wearable acceleration and gyro sensors based on quaternion calculations. *Sensors*, 13(7):9321–9343, 2013.

[70] Hartmut Geyer, Andre Seyfarth, and Reinhard Blickhan. Compliant leg behaviour explains basic dynamics of walking and running. *Proceedings of the Royal Society of London B: Biological Sciences*, 273(1603):2861–2867, 2006. ISSN 0962-8452.

[71] William John Schwind. *Spring loaded inverted pendulum running: A plant model.* Phd thesis, The University of Michigan, 1998.

[72] Reinhard Blickhan. The spring-mass model for running and hopping. *Journal of biomechanics*, 22(11-12):1217–1227, 1989. ISSN 0021-9290.

[73] GA Cavagna and M Kaneko. Mechanical work and efficiency in level walking and running. *The Journal of physiology*, 268(2):467, 1977.

[74] Daniel E Koditschek, Robert J Full, and Martin Buehler. Mechanical aspects of legged locomotion control. *Arthropod structure & development*, 33(3):251–272, 2004. ISSN 1467-8039.

[75] Reinhard Blickhan and RJ Full. Similarity in multilegged locomotion: bouncing like a monopode. *Journal of Comparative Physiology A: Neuroethology, Sensory, Neural, and Behavioral Physiology*, 173(5):509–517, 1993. ISSN 0340-7594.

[76] Hyunggwi Song, Heewon Park, and Sukyung Park. A springy pendulum could describe the swing leg kinetics of human walking. *Journal of Biomechanics*, 49(9):1504–1509, 2016. ISSN 0021-9290. doi: https://doi.org/10.1016/j.jbiomech.2016.03.018. URL `http://www.sciencedirect.com/science/article/pii/S0021929016303098`.

[77] Marc H Raibert. *Legged robots that balance*. MIT press, 1986. ISBN 0262181177.

[78] William Bosworth, Sangbae Kim, and Neville Hogan. The effect of leg impedance on stability and efficiency in quadrupedal trotting. In *Intelligent robots and systems (IROS 2014), 2014 IEEE/RSJ international conference on*, pages 4895–4900. IEEE, 2014. ISBN 1479969346.

[79] Qu Cao and Ioannis Poulakakis. Quadrupedal running with a flexible torso: control and speed transitions with sums-of-squares verification. *Artificial Life and Robotics*, 21(4):384–392, 2016. ISSN 1614-7456. doi: 10.1007/s10015-016-0330-5. URL `https://doi.org/10.1007/s10015-016-0330-5`.

[80] Qu Cao and Ioannis Poulakakis. Self-stable bounding with a flexible torso. In *proceedings of International Symposium on Adaptive Motion of Animals and Machines (AMAM), Darmstadt, Germany*, 2013.

[81] Qu Cao and Ioannis Poulakakis. Passive stability and control of quadrupedal bounding with a flexible torso. In *Intelligent Robots and Systems (IROS), 2013 IEEE/RSJ International Conference on*, pages 6037–6043. IEEE, 2013. ISBN 1467363588.

[82] Qu Cao and Ioannis Poulakakis. Control of quadrupedal bounding with flexible torso and speed transitions with sums of squares verification. In *The 1st International Symposium on Swarm Behaviour and Bio-inspired Robotics*, 2015.

[83] Qu Cao. *A modeling and control hierarchy of quadrupedal running with torso compliance*. Thesis, University of Delaware, 2016.

[84] Qi Deng, Shigang Wang, Wei Xu, Jinqiu Mo, and Qinghua Liang. Quasi passive bounding of a quadruped model with articulated spine. *Mechanism and Machine Theory*, 52:232–242, 2012. ISSN 0094114X. doi: 10.1016/j.mechmachtheory.2012.02.003.

[85] Yasuhiro Fukuoka, Hiroshi Kimura, and Avis H Cohen. Adaptive dynamic walking of a quadruped robot on irregular terrain based on biological concepts. *The International Journal of Robotics Research*, 22(3-4):187–202, 2003. ISSN 0278-3649.

[86] Zhenyu Gan and C David Remy. A passive dynamic quadruped that moves in a large variety of gaits. In *Intelligent Robots and Systems (IROS 2014), 2014 IEEE/RSJ International Conference on*, pages 4876–4881. IEEE, 2014. ISBN 1479969346.

[87] Zhenyu Gan, Thomas Wiestner, Michael A Weishaupt, Nina M Waldern, and C David Remy. Passive dynamics explain quadrupedal walking, trotting, and tölting. *Journal of computational and nonlinear dynamics*, 11(2):021008, 2016. ISSN 1555-1415.

[88] Elena Garcia, Juan C Arevalo, Manuel Cestari, and Daniel Sanz-Merodio. On the technological instantiation of a biomimetic leg concept for agile quadrupedal locomotion. *Journal of Mechanisms and Robotics*, 7(3):031005–031005–12, 2015. ISSN 1942-4302.

[89] Christian Gehring, C Dario Bellicoso, Stelian Coros, Michael Bloesch, Péter Fankhauser, Marco Hutter, and Roland Siegwart. Dynamic trotting on slopes for quadrupedal robots. In *Intelligent Robots and Systems (IROS), 2015 IEEE/RSJ International Conference on*, pages 5129–5135. IEEE, 2015. ISBN 1479999946.

[90] Tomoya Kamimura, Yuichi Ambe, Shinya Aoi, Kazuo Tsuchiya, and Fumitoshi Matsuno. Dynamical analysis of simple models with flexible body for bounding in quadrupeds. In *Systems, Man, and Cybernetics (SMC), 2016 IEEE International Conference on*, pages 1449–1454. IEEE, 2016. ISBN 1509018972.

[91] Hae-Won Park, Patrick M Wensing, and Sangbae Kim. High-speed bounding with the mit cheetah 2: Control design and experiments. *The International Journal of Robotics Research*, 36(2):167–192, 2017. ISSN 0278-3649.

[92] Ioannis Poulakakis, James Andrew Smith, and Martin Buehler. *On the dynamics of bounding and extensions: Towards the half-bound and gallop gaits*, pages 79–88. Springer, 2006.

[93] Ioannis Poulakakis, James Andrew Smith, and Martin Buehler. Modeling and experiments of untethered quadrupedal running with a bounding gait: The scout ii robot. *The International Journal of Robotics Research*, 24(4):239–256, 2005. ISSN 0278-3649.

[94] Marc Raibert, Kevin Blankespoor, Gabriel Nelson, and Rob Playter. Bigdog, the rough-terrain quadruped robot. *IFAC Proceedings Volumes*, 41(2):10822–10825, 2008. ISSN 1474-6670.

[95] Servet Soyguder and Hasan Alli. Computer simulation and dynamic modeling of a quadrupedal pronking gait robot with slip model. *Computers & Electrical Engineering*, 38(1):161–174, 2012. ISSN 00457906. doi: 10.1016/j.compeleceng.2011.11.007.

[96] C. Wang, T. Zhang, X. Wei, Y. Long, and S. Wang. Dynamic imbalance analysis and stability control of galloping gait for a passive quadruped robot. *Appl Bionics Biomech*, 2015:479615, 2015. ISSN 1176-2322 (Print) 1176-2322 (Linking). doi: 10.1155/2015/479615. URL `https://www.ncbi.nlm.nih.gov/pubmed/27110095`. Wang, Chunlei Zhang, Ting Wei, Xiaohui Long, Yongjun Wang, Shigang eng Egypt Appl Bionics Biomech. 2015;2015:479615. doi: 10.1155/2015/479615. Epub 2015 Jun 21.

[97] Ryuta Yamasaki, Yuichi Ambe, Shinya Aoi, and Fumitoshi Matsuno. Quadrupedal bounding with spring-damper body joint. In *Intelligent Robots and Systems (IROS), 2013 IEEE/RSJ International Conference on*, pages 2345–2350. IEEE, 2013. ISBN 1467363588.

[98] Singiresu S Rao and Fook Fah Yap. *Mechanical vibrations*, volume 4. Prentice hall Upper Saddle River, 2011.

[99] Valerie Illingworth. *Dictionary of computing*. Oxford University Press, Inc., 1997.

[100] Christopher Clapham and James Nicholson. *The concise Oxford dictionary of mathematics*. OUP Oxford, 2009.

[101] Peter Aerts and D De Clercq. Deformation characteristics of the heel region of the shod foot during a simulated heel strike: the effect of varying midsole hardness. *Journal of sports sciences*, 11(5):449–461, 1993. ISSN 0264-0414.

[102] John EA Bertram. *Understanding mammalian locomotion: concepts and applications*. John Wiley & Sons, 2016. ISBN 0470454644.

[103] Peter G Weyand, Deborah B Sternlight, Matthew J Bellizzi, and Seth Wright. Faster top running speeds are achieved with greater ground forces not more rapid leg movements. *Journal of applied physiology*, 89(5):1991–1999, 2000. ISSN 8750-7587.

[104] James W Cooley, Peter AW Lewis, and Peter D Welch. The fast fourier transform and its applications. *IEEE Transactions on Education*, 12(1):27–34, 1969.

[105] Monson H Hayes. *Statistical digital signal processing and modeling*. John Wiley & Sons, 2009.

[106] Christopher Torrence and Gilbert P Compo. A practical guide to wavelet analysis. *Bulletin of the American Meteorological society*, 79(1):61–78, 1998.

[107] Sophie Biau, Sophie Lemaire, and Eric Barrey. Analysis of gait transitions in dressage horses using wavelet analysis of dorsoventral acceleration. *Pferdeheilkunde*, 18(4):343–353, 2002. ISSN 0177-7726.

[108] Australian Standard. Playground surfacing-specifications, requirements and test method, 2016.

[109] S.B Williams. Functional anatomy and muscle moment arms of the pelvic limb of an elite sprinting athlete: the racing greyhound (canis familiaris). *Journal of Anatomy*, 213:361–372, 2008.

[110] James R Usherwood and Alan M Wilson. Biomechanics: no force limit on greyhound sprint speed. *Nature*, 438(7069):753, 2005.

[111] Penny E Hudson, Sandra A Corr, and Alan M Wilson. High speed galloping in the cheetah (acinonyx jubatus) and the racing greyhound (canis familiaris): spatio-temporal and kinetic characteristics. *Journal of Experimental Biology*, 215(14):2425–2434, 2012. ISSN 0022-0949.

[112] Fatemeh Mahdavi, Paul Kennedy, David Eager, and Hasti Hayati. Ageing and resulting injuries: effects on racing greyhounds. In *European Society of Biomechanics (ESB), Vienna, Austria, July 5 to 7*, 2019.

[113] Marjolaine Baude, Emilie Hutin, and Jean-Michel Gracies. A bidimensional system of facial movement analysis conception and reliability in adults. *BioMed research international*, 2015:1–8, 2015. ISSN 2314-6133.

[114] Camma Damsted, Rasmus Oestergaard Nielsen, and Lars Henrik Larsen. Reliability of video-based quantification of the knee-and hip angle at foot strike during running. *International journal of sports physical therapy*, 10(2):147–154, 2015.

[115] A.S Jayes. Estimates of mechanical stresses in leg muscles of galloping greyhounds (canis familiaris). *Journal of Zoology*, 1982.

[116] Claire T Farley, James Glasheen, and Thomas A McMahon. Running springs: speed and animal size. *Journal of experimental Biology*, 185(1):71–86, 1993.

[117] Thomas A McMahon and George C Cheng. The mechanics of running: how does stiffness couple with speed? *Journal of biomechanics*, 23:65–78, 1990.

Appendices

Appendix A

The MATLAB code used in Chapter 5 to pick acceleration peaks

```
close all;
% Script file: peak_structure.m
%
%Purpose:
%       detect the peaks in data (structures)
%       Record of revisions:
%       Date        Programmer          Description of Change
%       ====        ==========          =====================
%    08/08/2019    HASTI HAYATI         modified MATLAB code
%% read xlsx files
[~,sheets] = xlsfinfo('imu_time_grafton.xlsx');
for i = 1:length(sheets)
    data{i} = xlsread('imu_time_grafton.xlsx',sheets{i})
end
%% findpeaks
PeaksCell=cell(size(data));
for i=1:length(data);
figure(i)
    for j=1:3
    [pks,locs] = findpeaks(data{i}(:,j+1),data{i}(:,1),'
        MinPeakDistance',0.2);
    PeaksCell{i}.pkslocs{j}(:,2)=pks;
    PeaksCell{i}.pkslocs{j}(:,1)=locs;
    figure()
    plot(data{i}(:,1),data{i}(:,j+1));
    hold on
    scatter(PeaksCell{i}.pkslocs{j}(:,1),PeaksCell{i}.
        pkslocs{j}(:,2))
```

```
27      xlabel('Time (s)')
28      ylabel('Acceleration (g)')
29      end
30  end
```

The MATLAB code used in Chapter 5 to apply FFT on acceleration signals

```
close all;
% Script file: fft_transformation_Hasti_v2
%
%Purpose:
%       This is the code to convert time-domain data to freq
    domain data using FFT function.
%       Record of revisions:
%       Date        Programmer          Description of Change
%       ====        ==========          =====================
%     08/08/2019    HASTI HAYATI         modified MATLAB code
%%       Call the data
[~,sheets] = xlsfinfo('imu_data_cessnock.xlsx');
for m = 1:length(sheets)
    data{m} = xlsread('imu_data_cessnock.xlsx',sheets{m})
end
%%       FFT
F={};
X_mag = cell(size(data));
P2 = cell(size(data));
P1 = cell(size(data));
f = cell(size(data));
% Fs = 100;           %for GPSport unit
Fs = 185;             %for iKMS unit
for s = 1:length (data)
    F{s} = fft(data{(s)})
    for h = 1:length (F)
        X_mag{h} = abs(F{h})
        P2{h} = X_mag{h}/length(F{h})
```

```
28          P1{h} = P2{h}(h:(length(F{h})/2) + h,:)
29          P1{h}(2:end - h) = 2*P1{h}(2:end - h)
30          f{h} = Fs*((0:length(F{h})/2)/length(F{h}))
31      end
32  end
33  %%      Localmaxima to find the peaks in the signals
34  time = f;
35  PeaksCell=cell(size(P1));
36  acc=cell(size(P1))
37  for m=1:length(P1);
38  figure(m)
39  acc{m}=P1{m}
40      for j=1:3
41      [pks,locs] = findpeaks(acc{m}(:,j),time{m},'
            MinPeakDistance',2);
42      PeaksCell{m}.pkslocs{j}(:,2)=pks;
43      PeaksCell{m}.pkslocs{j}(:,1)=locs;
44      figure()
45      plot(time{m},acc{m}(:,j));
46      hold on
47      scatter(PeaksCell{m}.pkslocs{j}(:,1),PeaksCell{m}.
            pkslocs{j}(:,2))
48      xlabel('Frequency (Hz)')
49      ylabel('Amplitude (g)')
50      grid on
51      end
52  end
```

The MATLAB code used in Chapter 5 to apply wavelet transform on acceleration signals

```
1  close all;
```

```
% Script file: Wavelet_changepoint_detection.m
%
%Purpose:
%       wavelet transform on signals
%       Record of revisions:
%       Date        Programmer          Description of Change
%       ====        ==========          =====================
%     15/08/2019    HASTI HAYATI         modified MATLAB code
%% plot your signal in time-domain
[~,sheets] = xlsfinfo('Copy of imu_time_richmond.xlsx');
for i = 1:length(sheets)
    data{i} = xlsread('Copy of imu_time_richmond.xlsx',
       sheets{i})
end
%%
figure;
plot(data{1, 3}(:,1),data{1, 3}(:,3))
xlabel('Time (mins)');ylabel('Dorso-ventral Acceleration (g)
    ');
title('Acceleration Signal');axis tight
grid on
Fs = 100;           %for GPSport unit
%Fs = 185;             %for iKMS unit
%% Time Frequency using Spectrogram.
figure;
spectrogram(data{1, 3}(:,3) ,[],[],[],Fs,'yaxis');
%% Spectrogram using shorter window
figure;
spectrogram(data{1, 3}(:,3) ,128,[],[],Fs,'yaxis'); title('
   Spectrogram using shorter window');
%% cwt
```

```
figure;
cwt(data{1, 3}(:,4),Fs);
%% Fine Scale Analysis
No = 8; %8
Nv = 32;%32
figure;
cwt(data{1, 3}(:,3),Fs, 'NumOctaves' ,No,'VoicesPerOctave',
    Nv);
title('CWT with Number of Octaves: 10 and Voices per Octave:
     32');
%% Reconstruct the seismic signal
[WT, F] = cwt(data{1, 3}(:,3),Fs);
xrec = icwt(WT, F, [1 2],'SignalMean',mean(data{1, 3}(:,3)))
    ;
figure;
plot(data{1, 3}(:,1),xrec,'b');title('Reconstructed Seismic
    Signal'); axis tight;grid on;
% END
```

The MATLAB code used in Chapter 6 to simulated RH single-support dynamics

The function

```
% Script file: GR_dof3F.m
%
%Purpose:
%       A 3DOF model of a greyhound hind-leg over different
    types of surfaces
%       The EOM is solved using ODE45 solver in MATLAB R18
%       This code can be developed to a higher DOF to mimic
    multilegged
%       locomtion
```

```
%       Record of revisions:
%       Date        Programmer          Description of Change
%       ====        ==========          =====================
%       22/12/17    HASTI HAYATI          Orogincal code


%% THE CODE IS MODIFIED ON 19/12/2018
close all;
function s=GR_dof3F(ts,ys);
m1=32;
m2=3.4;       % This value is obtained from the literature
k1=4*10^3     % This value is obtained from the literature
%% WET SAND
k2=287 *10^3  %SAND
c2=251
%% 7CM RUBBER
%k2=6.8287e+04
%c2=8.6e+01;
%% GRASS
% k2=1.0765e+05;
% c2=89
%% Initial Conditions
l01=0;        %Initial hip to toe length
l02=0;        %inital surface penetration
g=9.8;        %gravitational acceleration
%% Statespace method
s=zeros(6,1);
s(1)=ys(2);
s(2)=2*ys(1)*(ys(4)^2) - (k1/m1)* ((ys(1)-l01)-(ys(5)-l02))
    -(c2/m1)*(ys(6))-g*sin(ys(3))
s(3)=ys(4);
```

```
38 s(4)=-g*cos(ys(3))/2*ys(1) - 2*ys(2)*ys(4)/ys(1)
39 s(5)=ys(6);
40 s(6)=(k1/m2)*((ys(1)-l01)+(ys(5)-l02))-(k2/m2)*(ys(5)-l02)-(
       c2/m2)*(ys(6))
```

The solver

```
1  % Script file: GR_dof3S.m
2  %
3  %Purpose:
4  %       A 3DOF model of a greyhound hind-leg over different
       types of surfaces
5  %       The EOM is solved using ODE45 solver in MATLAB R18
6  %       This code can be developed to a higher DOF to mimic
       multilegged
7  %       locomtion
8  %       Record of revisions:
9  %       Date        Programmer          Description of Change
10 %       ====        ==========          =====================
11 %       22/12/17    HASTI HAYATI          Orogincal code
12 close all;
13 tspan=[0:6.5244e-04:0.0535];
14 y0=[0.6389;-18;2.295108;-12;0;0]; %Initial
15 %% ODE solver
16 [ts,ys]=ode45(@GR_dof3F,tspan,y0);
17 k1=4*10^3
18 %% Plot the results
19 subplot(321) %leg compression
20 plot(t*1000,Y(:,1)*1000)
21 grid on
22 xlabel('Time (ms)');
23 ylabel('l (mm)');
```

```
24 hold on
25 title ('A')
26 subplot(322) %leg rotation
27 plot(t*1000,Y(:,3))
28 grid on
29 xlabel('Time (ms)');
30 ylabel('\theta (rad)');
31 hold on
32 title ('B')
33 subplot(323) %surface penetration
34 plot(t*1000,Y(:,5)*1000)
35 grid on
36 ylabel('y (mm)');
37 xlabel('Time (ms)');
38 hold on
39 title ('C')
40 subplot(324) %surface velocity
41 xi=Y(:,1).*cos(Y(:,3));
42 yi=Y(:,1).*sin(Y(:,3));
43 plot(xi*1000,yi*1000);
44 xlabel('X (mm)');
45 ylabel('Y (mm)');
46 grid on
47 title ('D')
48 hold on
49 subplot(325) %GRF
50 grf_com=abs(Y(:,1)-0.781).*k1.*sin(Y(:,3));
51 plot(t*1000,grf_com);
52 ylabel('Force (N)');
53 xlabel('Time(ms)');
54 hold on
```

```
55 grid on
56 title ('E')
57 subplot(326) %Impact Force
58 grf_y=abs(Y(:,5)*k2);
59 plot(t*1000,grf_y);
60 ylabel('Force (N)');
61 xlabel('Time(ms)');
62 hold on
63 grid on
64 title ('F')
```

Appendix B

Runge Kutta 4^{th} order method to solve differential equations

The Runge Kutta methods are a family of implicit and explicit interative methods. The most well-known type of Runge-Kutta family is the 4^{th} order method, usually reffered to as 'RK4' [99, 100].

Let the initial value be given as follows:

$\dot{y} = f(t, y), \quad y(t_0) = y_0$

where y is a function of a time t. The $\dot{y}$ is the rate of change of y over time.

Firstly, the step size should be defined given as:

$y_{n+1} = y_n + \frac{1}{6}(k_1 + 2k_2 + 2k_3 + k_4); \quad t_{n+1} = t_n + h$

where h is the step height. For $n = 1, 2, 3, ...$ and by using:

- $k_1 = hf(t_n, y_n)$;
- $k_2 = hf(t_n + \frac{h}{2}, y_n + \frac{k_1}{2})$;
- $k_3 = hf(t_n + \frac{h}{2}, y_n + \frac{k_2}{2})$;
- $k_4 = hf(t_n + h, y_n + k_3)$;

Accordingly, y_{n+1} is the RK4 approximation of $y(t_{n+1})$. As mentioned, this method is called the 4^{th} order method, which means that the local truncation error is on the order of $O(h^5)$, while the total accumulated error is order $O(h^4)$.

The state-space method

MATLAB Ordinary Differential Equations (ODE) solvers, are based on the Runge-Kutta methods. However, as RK4 can only solves the first-order ODEs, the 'state-space' method should be used to reduce the order of the ODE.

The state-space model can be used for linear, nonlinear, time-variant and time-invariant systems. Using this method, the n^{th} differential equation can be reduced to n first-order differential equation which is expressed as follows:

$$\dot{x(t)} = A(t)x(t) + B(t)u(t)$$

$$y(t) = C(t)x(t) + D(t)u(t)$$

where:

- x is called the 'state vector';
- y is called the 'output vector';
- u is called the 'input vector';
- A is a $n \times n$ called 'state matrix';
- B is a $n \times p$ called 'input matrix';
- C is a $q \times n$ called 'output matrix';
- D is a $q \times p$ the 'feedthrough matrix'.

Accordingly, based on the type of ODE, the state-space method can be used to reduce the order of the equation.